Delft University of Technology

MSc. Thesis

Comparative Study of Steady and Unsteady method Optimization applied to Turbomachinery

by :

A. Reever Stooss

to obtain the degree of Master of Science in Aerospace Engineering at the Delft University of Technology, to be defended on Friday March 12, 2021 at 9:30.

Student Number :	4741145
Principal Supervisor:	Dr. Ir. M. Pini, TU Delft
Thesis Committee :	Prof. Dr. Ir. P. Colonna, TU Delft
	Dr. Ir. M. Pini, TU Delft
	Dr. Ir. A.H. van Zuijlen, TU Delft
	Ir. N. Anand, TU Delft

TU Delft Delft University of Technology

Abstract

Turbomachines are prevalent within the aerospace industry and vital for both power production and flight systems. To achieve better performance and higher efficiency, a numerical optimization technique is used to optimize designs. Previous work has primarily focused on performing steady-state optimization of turbomachinery using Reynolds Averaged Navier Stokes simulations. In efforts for further performance increases, the next step of turbomachinery optimization is to incorporate time-accurate solvers. These time-accurate solvers are computationally more expensive than steady solvers, which hinders usage in optimization. The harmonic balance method was developed to reduce computational requirements compared to a time-accurate solver while maintaining unsteady flow characteristics in the simulation results. Optimization using the harmonic balance method has shown better performance in 2D cases, but there has not been work reporting on a 3D case. Further analysis of how optimization changes flow irreversibility in a design has not been shown between harmonic balance and mixing plane based optimization. This work's novel contribution is to perform a comparative study of harmonic balance and mixing plane based optimization of a 3D multistage turbine and perform a loss quantification comparison of the optimized designs. In this work, the flow around a 3D 1.5 stage axial turbine in the subsonic to transonic flow regime was simulated and optimized using the mixing plane and harmonic balance methods. The turbine blade shapes are parameterized using a CAD-based NURBS parameterization and optimized using a gradient-based adjoint algorithm. Flow features, entropy trends, and computational costs between harmonic balance and mixing plane simulation and optimization were compared. This study shows that most entropy creation differences between harmonic balance and mixing plane methods occur in the rotating domain. A turbine design optimized using the harmonic balance method has better fluid-dynamic performance than a design optimized using the mixing plane method. Turbine designs combining blades from both harmonic balance and mixing plane based optimization show better performance than a design using a single flow simulation method for optimization. Results also indicate that a grid converged mesh may not be necessary for entropy generation minimization of turbomachinery designs for transonic flow.

Contents

List of Figures

List of Tables

Nomenclature

Acronyms

2D	2 Dimensional
3D	3 Dimensional
CFD	Computational Fluid Dynamics
CFL	Courant-Friedrichs-Lewy number
DFT	Discrete Fourier Transform
FFD	Free form deformation.
FGMRES	Flexible Generalized Minimal Residual method
GC	Grid Converged
HB	Harmonic Balance
HPC	High Performance Cluster
JST	Jameson-Schmidt-Turkel
LES	Large Eddy Simulation
LUSGS	Lower-Upper Symmetric Gauss-Seidel
MP	Mixing Plane
NURBS	Non-Uniform Rational Basis Spline
Opt	Optimized
R1	Rotor 1
RANS	Reynolds Averaged Navier-Stokes
S1	Stator 1
S2	Stator 2
SLSQP	Sequential Least Squares Programming
SST	Menter's Shear Stress Transport turbulence model
TE	Trailing Edge
URANS	Unsteady Reynolds Averaged Navier-Stokes

Greek Symbols

ϵ	Perturbation value
γ	Specific heat ratio
α	Design parameter vector
τ	Reynolds Stress Tensor
τ^r	Residual Stress Tensor
ν	Kinematic Viscosity
ω	Rotation Speed
θ_{in}	Blade section inlet angle
θ_{out}	Blade section outlet angle
ζ	Stagger

Operator

$\langle\phi\rangle$	Spatially Filtered Average
$\overline{\phi}$	Temporal Average or Spatial Average
ϕ'	Value fluctuation

Symbols

P	Power
$\langle s\rangle$	Mass-flow Averaged Entropy
$\mathbf{E}_{k,n}$	DFT matrix
$\mathcal{O}$	Order of Accuracy
Ω_{HB}	Frequency
ρ	Density

$\mathbf{R}$	Residual Vector
$\mathbf{X}$	Mesh Grid points
C_p	Specific heat at constant pressure
C_v	Specific Heat at constant volume
C_d	Dissipation Coefficient
G	Inequality Constraint
H	Equality Constraint
J	Objective Function
M	Mach Number
M_{rel}	Relative Mach Number
R	Gas Constant/ Boltzmann Constant
s	Specific Entropy
s_{gen}	Entropy Generation rate
V	Velocity
$y+$	Dimensionless Wall Distance
$\mathbf{U}$	Conservative Flow Quantity Vector
K	Number of Frequency's
N	Number of
P	Pressure

Subscripts

tot	Total
i, j	Spatial index
ref	Reference Point
x, y, z	Spatial Direction
surf	blade surface

Chapter 1

Introduction

Turbomachinery play a significant role in everyday life and are of particular importance to aerospace applications. These machines are responsible for fluid transport, power generation and extraction, and other applications. An accurate understanding and modeling of the underlying fluid physics are paramount to designing high-performance and efficient machines. Since the 1960s, with the advent of Computational fluid dynamics (CFD), there have been significant advances in numerical modeling techniques to simulate flow physics [1] accurately.

CFD has been under development for many years and offers many methods (or flow solvers) to simulate flow physics. Turbomachinery problems are of particular interest to aerospace applications due to their widespread use in turbofans, rocket engines, and power generation. A flow solver typically used for turbomachines is a steady Reynolds Averaged Navier Stokes (RANS) solver, which simulates a temporally and statistically averaged flow solution. RANS solvers work in both 2D and 3D problems but come with a drawback inherent to turbomachines. All turbomachines exhibit flow unsteadiness, with the prime example seen in a blade wake. The wake is a non-uniform flow region that changes in both time and space that can significantly affect downstream components' performance. Other flow solvers have been developed to incorporate unsteadiness into the flow simulation.

A well-known unsteady solver is the Large Eddy Simulation (LES) method, typically used in 3D problems for accurate flow physics computations. The drawback of LES is the substantial computational costs associated with simulations using this method compared to a steady solver, sometimes up to an order of magnitude larger [2]. Unsteady RANS (URANS) offers a middle ground to RANS and LES solvers to capture some large-scale wakes as commonly seen in turbomachinery problems [3] at a lower cost to LES methods. Previous work [2, 4] has shown that even the URANS method is too computationally expensive and borderline unfeasible for optimization. The harmonic balance method was developed to resolve periodic unsteady flow at a reduced computational cost and was applied to an internal flow problem in [5].

The problem of increasing computational cost is further exacerbated when simulating multizone turbomachines. Multizone machines refer to machines with multiple blade rows. Further resources are required to store greater amounts of information for the simulation. In turbomachinery, the rotor is a rotating blade row that either transfers work into or out of the flow. Because there is a rotating and stationary domain, an interface is needed to transport flow quantities between domains. In typical RANS solvers, a mixing plane [6, 7] has been used, which averages quantities as they pass through the interface while in time accurate solvers an interpolation procedure is done. These interfaces require additional computational resources for use in flow simulation [8].

Once the turbomachine has been simulated, the performance can be assessed and is typically optimized. Optimization involves simulating many different designs to find the best performing one but comes at the cost of higher requirements in either time and or resources than a simple flow simulation [4, 9]. A turbomachinery design is composed of blades that can have individual and unique geometries. Due to the high cost of optimization, algorithms have been developed to traverse the design space more efficiently and belong to one of two categories: gradient-free and gradient-based. These two categories refer to whether the optimization algorithm uses the sensitivity information. Sensitivity refers to how design variable changes will affect the results. In [9] gradient-based algorithms perform much better and lead to substantially lower optimization times and provide a basis for requiring efficient sensitivity calculation methods. One of the most efficient methods of calculating sensitivities is the discrete adjoint method seen in [10] and applied to a multistage turbine in [4, 8, 11] with

success. The discrete adjoint method allows for multiple design sensitivities to be calculated with only two solutions, a direct flow solution, and an adjoint solution.

Previous work has been done on understanding how optimization impacts performance when using a steady method in 2D [8, 12] and 3D [13]. The unsteady optimization result using harmonic balance has been compared in 2D design problems [4, 11] but has not been extended to 3D problems.

Typically a loss accounting is done to quantify performance outcomes in turbomachines. Loss accounting quantifies energy or work converted from a useful form in the flow to an unusable format as an unintended side effect of regular machine operation. In work done by J. Denton [14], the primary sources of losses are shown to stem from viscous friction, heat transfer, and nonequilibrius processes. Previous results have quantified single machine losses [15] or between specific flow solver methods [16] but have not compared how losses are changed by optimization.

Stemming from these considerations, two related research areas can be combined to produce a novel result. By combining loss accounting with optimization of a 3D turbomachine using both steady RANS and unsteady harmonic balance methods, a designer can understand which flow solver is worth the computational resources required for the optimization.

1.1 Knowledge Gap

Previous work demonstrates that using the harmonic balance method in optimization has shown increased turbomachinery performance in 2D design problems. In contrast, 3D optimizations have primarily been done with a steady mixing plane method. Furthermore, analysis of loss and entropy in a 3D multizone blade shape optimized design using both harmonic balance and mixing plane methods has not been reported. This research fills the knowledge gap by investigating how the choice of flow solver method used for optimization affects entropy and how the resulting blade geometries differ between optimization using the harmonic balance method rather than mixing plane. As a result of this work, The performance benefits of using harmonic balance instead of mixing plane method for optimization of a 3D test case and where optimization affects performance are quantified.

1.2 Research Goal

To address the knowledge gap, the research goal of this thesis can be formulated as:

> *The research aim of this work is to quantify the performance difference of using an unsteady method instead of a steady method for optimizing a 3D multistage turbine.*

An emphasis is placed on understanding how the mass-flow averaged entropy is distributed and changed by the optimization process.

1.3 Research Questions

To achieve the research aim of this thesis, four research questions must be answered.

* What performance increase is realized when using a 3D harmonic balance optimization over a steady mixing plane optimization in a 3D multistage turbine test case?
* What are the entropy differences through machine zones for 3D multizone steady mixing plane and harmonic balance simulations?
* What changes does optimization make to the entropy in each flow region?
* What are the entropy differences distributed through the machine zones for mixing plane and harmonic balance optimized designs?

1.4 Research Objectives

To provide proof to the research questions, the following objectives are made for data collection.

* Quantify entropy differences through machine regions for 3D multizone mixing plane and harmonic balance simulations.
* Quantify performance increase seen when using a harmonic balance based optimization over a mixing plane based optimization in a 3D multistage turbine test case.
* Quantify entropy changes in multizone optimization and its distribution through machine regions for mixing plane, and harmonic balance optimized designs.

1.5 Original Contribution

The work presented in this thesis brings a novel analysis of the differences in entropy generation in 3D CAD-based parameterized multistage turbine optimized using harmonic balance and mixing plane methods. A new investigation of how optimization changes the mass-flow averaged entropy along the mean flow direction in a multistage turbine is also shown. The following points are unique contributions:

* Analysis of a 3D multistage axial turbine entropy trend difference between harmonic balance and mixing plane method simulation.
* Computational requirement comparison of harmonic balance and mixing plane simulation and optimization of a 3D multistage turbine.
* Harmonic balance and mixing plane based optimized design entropy trend comparison of a 3D multistage turbine test case.

Thesis Layout

Each chapter will detail a specific portion of the thesis work and are briefly summarized below.

chapter 2 reports on previous work in turbomachinery optimization and loss parameters. The mathematical basis for flow solvers and algorithms used are briefly explained with documentation for further resources. Loss parameters are explained with an overview of how losses are generated and their impact on turbomachinery performance.

chapter 3 describes the setup and analysis used in this study. Specific implementation and reasoning are given for why various tools are used and their impact on data extraction and analysis.

chapter 4 gives an overview of the test case. A grid convergence study shows the extent to which the objection function value depends on mesh size and subsequent computational cost scaling.

chapter 5 reports the resulting flow fields and entropy distributions. Mach contours and entropy trends as a function of axial distance are examined to determine where the two flow solver methods differ and how large the difference is. The optimization outcomes using both flow solver methods are compared, and further hypothesis testing and conclusions are shown in this chapter.

chapter 6 summarizes the study and gives conclusions along with recommendations for future work.

Chapter 2

Background

The background information necessary to answer this work's research goal can be broken up into three areas.

Turbomachinery Optimization: This section will give an overview of the steps and scientific basis in optimization. Specific emphasis in each method is given towards applications in turbomachines.

Current Optimization works: The current results of turbomachinery optimizations are shown in this section. Open areas of interest are shown here and form the foundation from which this thesis extends.

Loss accounting in Turbomachinery: How losses are accounted for in typical turbomachinery applications are explained in this section. Any differences in loss between simulation methods and machine geometry are the basis for concluding and understanding why certain methods should be preferred.

Each of these areas will be examined and explained with the context of previous scientific literature.

2.1 Aerodynamic Design Chain

This section will go into detail about how optimization is done in the context of turbomachinery. The optimization process in turbomachinery, otherwise known as the aerodynamic design chain, is a relatively simple series of steps, which can be seen in Figure 2.1.

The steps denoted in blue boxes are algorithmic steps that an optimization software implements to perform the optimization. A brief description of each step is given below, with an in-depth treatment in subsequent sections.

0. **Blade Parameterization**: The blade(s) geometry is parameterized into a finite vector α of N length and used as the design vector. This parameterization describes the underlying blade shape and changes to the values in α reflect a change of the blade shape.
1. **Surface Deformation**: The blade surface mesh points ($\mathbf{X}_{\text{surf}}$) are changed according the values in α. All mesh elements that correspond to the surface are translated to reflect the design vector change.
2. **Mesh Deformation**: Using the deformed surface mesh points the entire volumetric mesh ($\mathbf{X}$) is translated. The volumetric mesh must still maintain certain characteristics, such as the absence of negative mesh cell volumes and retain the original point connectivity, i.e., mesh points can not be added or deleted, and connections between mesh points are immutable.
3. **Flow Solver**: The flow is simulated in the mesh, and the resulting flow vector ($\mathbf{U}$) is calculated. The objective function (J) and inequality constraint (G) are extracted from the flow domain. There are various flow solving methods with RANS as a steady-state averaging approach to LES, which resolves many time-varying flow structures and turbulent interaction.
4. **Gradient Solver**: In this step, the gradient is calculated for the objective and inequality constraints of the problem. The gradient contains information about how sensitive the quantity of interest is to a design vector perturbation. The objective gradient, or in another term, sensitivity ($\frac{dJ}{d\alpha}$) indicates if the perturbation will increase or decrease the objective function value. The inequality constraint sensitivity ($\frac{dG}{d\alpha}$) contains information on whether the design vector perturbation is moving towards or away from a

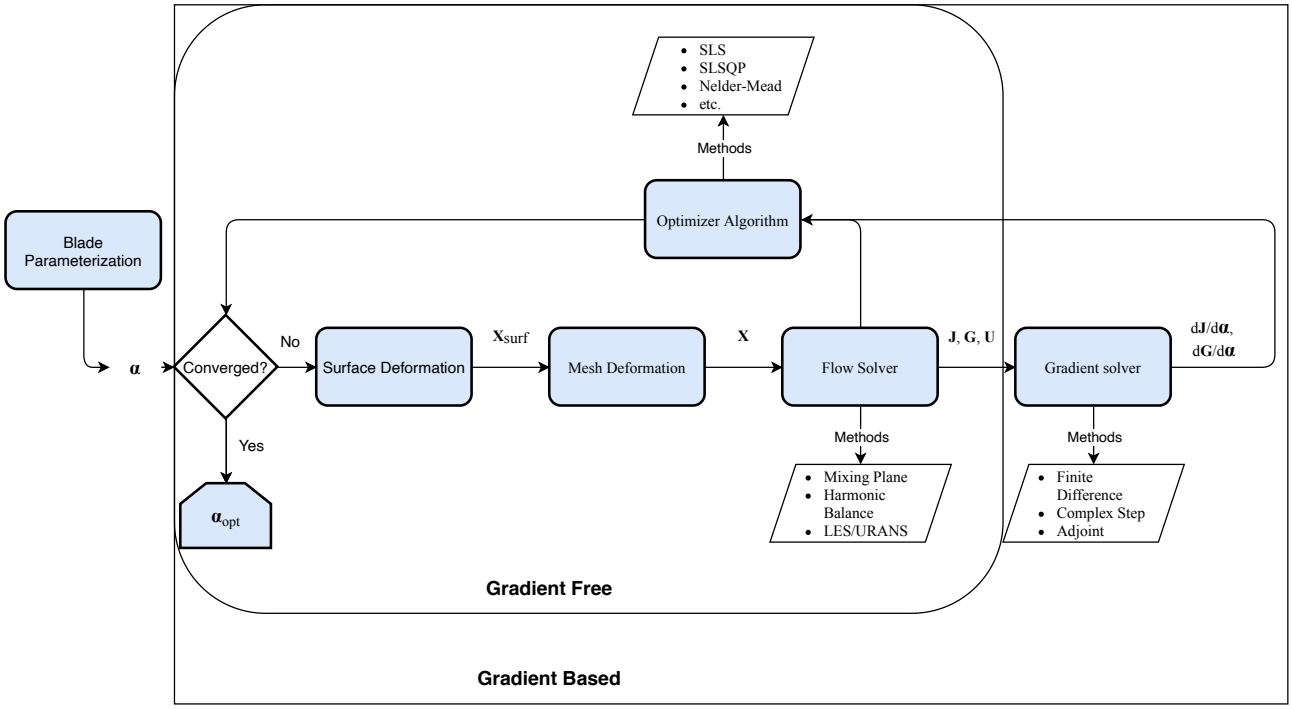

Fig. 2.1: General aerodynamic design chain.

valid design space. There are various methods of calculating the gradient, but the output of each approach is the same.

5. **Optimizer Algorithm**: The optimization algorithm uses the information of the objective function, inequality constraint, and optionally gradient information to determine what change to make in the parameterization to minimize the objective and stay in the valid design space.

The purpose of optimization is to maximize or minimize some value subject to the constraints of the problem. This can formally be written as:

$$\begin{aligned} \min_{\alpha} \quad & J(\mathbf{U}(\alpha), \mathbf{X}(\alpha)), \\ s.t. \quad & G(\alpha) \leq 0, \\ & H(\alpha) = 0. \end{aligned} \tag{2.1}$$

This treatment of optimization covers optimization in the context of a turbomachinery design problem. J refers to the objective function, which will be minimized. The objective function value is dependent on the flow field vector ($\mathbf{U}$) and the volumetric mesh ($\mathbf{X}$). The volumetric mesh and flow field vector depend on the design vector (α). In turbo-machinery, α can be some pre-allocated blade parameterization or coordinates to determine shape deformation. Further detail can be found in subsection 2.1.1.

The equation(s) found in $G(\alpha)$ consists of inequality constraints and can be seen as

$$G(\alpha) \leq 0. \tag{2.2}$$

In cases involving turbomachinery, some inequality constraints are minimum blade outlet angle, power output, or overall pressure ratio. The exact value of inequality constraints is irrelevant within the optimizer algorithm, so long as it is below some threshold.

The constraint equation(s) found in $H(\alpha)$ are all equality constraints. Moreover, it can be written as

$$H(\alpha) = 0. \tag{2.3}$$

The purpose of these constraints is to ensure that some parameter within the optimization problem is always the same. For the optimization process to fully converge and give a valid optimum, this constraint **must** be

met. In a typical case, the machine's power output can be used as an equality constraint as producing too much power can lead to over-designing the appliance, and too little power is not enough for the machine's design point.

The objective function (J) is a significant parameter in the optimization process and substantially impacts the optimization solution. Within turbomachinery, importance is placed upon some measurement of thermodynamic efficiency. Further detail of what parameters can/are used as an objective for optimization are shown in section 2.3.

2.1.1 Parameterization

An essential element for optimization is the design vector that the optimizer can use for changing the underlying blade shape. A useful method of achieving this goal is to parameterize the blade shape. By parameterizing the blade shape, a unique combination of numbers can describe the blade in question. The optimizer can then use the base parameterization and change various values to produce the next design step's blade shape.

2.1.1.1 CAD-Based Parameterization

One method for parameterization is using Non-Uniform Rational Basis Spline (NURBS) curves [17] with control points to describe an initial blade shape and is a type of CAD-based parameterization. Any changes in parameterization value can easily be reflected as a surface point translation. A CAD-based NURBS curve approach lends itself to a more physically intuitive blade parameterization method in which different control points control certain aspects of a blade shape. Another benefit of this approach is that physical constraints such as blade thickness, angles, or radii can be directly controlled and maintained during the optimization process.

Three main areas need to be described by the parameterization method for 3D blade shapes. These areas are the blade meridional channel, blade section, and the span. Each of the areas addresses a specific blade geometry. The blade meridional channel describes the shape of the blade moving in the flow direction. The blade section describes the blade profile at a particular span position, while the blade span parameterization describes where a blade profile occurs with respect to the blade's length.

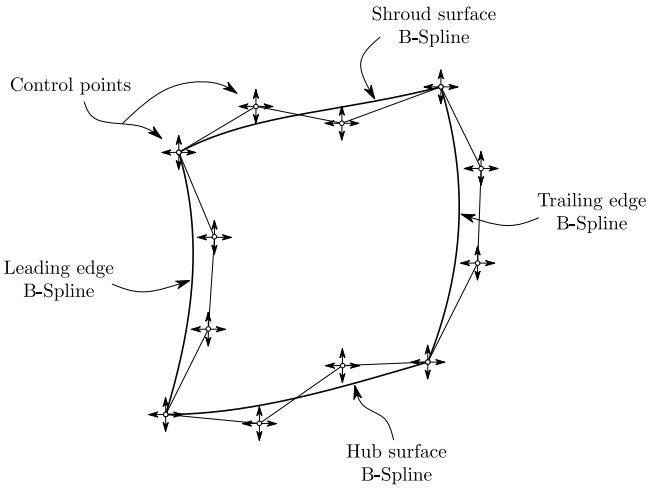

Fig. 2.2: NURBS Blade Meriodional Channel Parameterization from Ref. [18].

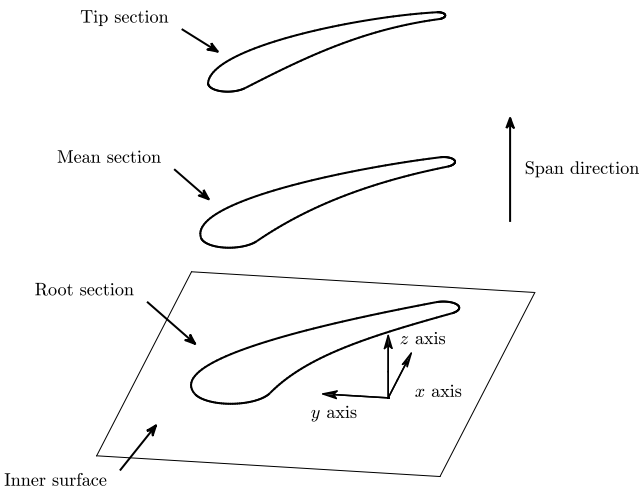

Fig. 2.3: Blade Span Parameterization from Ref. [18].

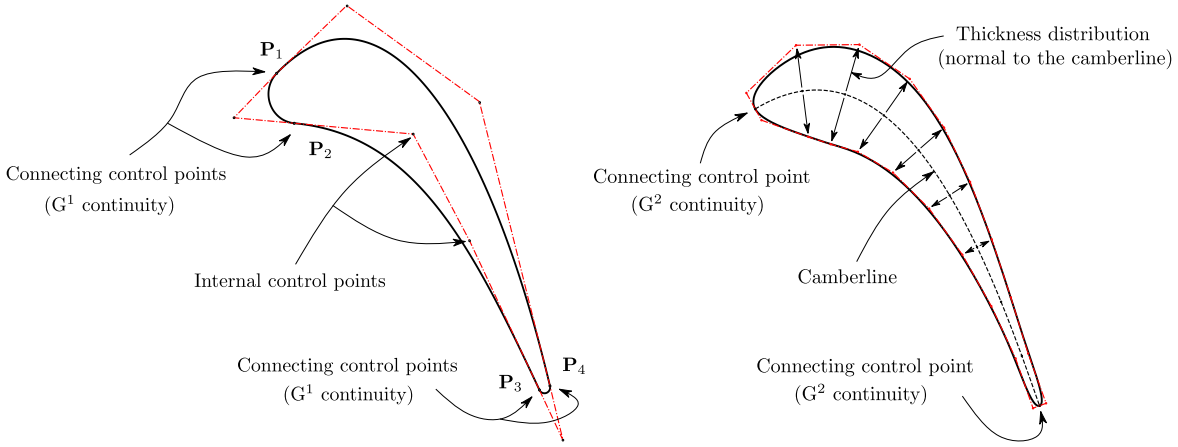

(**a**)NURBS Connecting arcs blade section parameterization.

(**b**)NURBS Camber thickness distribution blade section parameterization.

Fig. 2.4: Blade section parameterization examples from Ref. [18].

2.1.1.2 Free Form Deformation box

Another way to parameterize the blade for the optimizer is the FFD box, or Free Form Deformation box [19]. The FFD box approach overlays a box on the region to be changed similar to Figure 2.5. Each intersection of a line is a control point that the optimizer can translate. When a control point has moved, the parallelogram which is comprised of that point is deformed. All points of the underlying object, in this case, blade shape, are then distorted following the deformation of the original parallelogram. A drawback of this approach is that there is no fundamental connection between the FFD box and underlying shapes, resulting in many different control point changes possibly producing the same blade shape. An FFD box approach also poses problems for geometric constraints that might need to be placed on the underlying geometry. Ensuring specific blade shape characteristics becomes difficult. The benefit of this approach is that parameterization is straightforward and easy to implement.

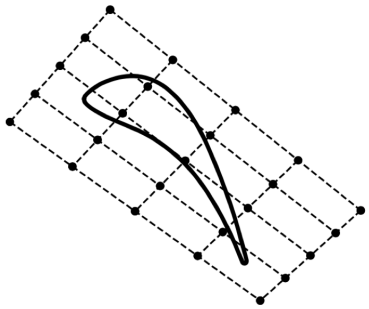

Fig. 2.5: FFD box demonstration from Ref. [12].

The actual surface distortion for a specific point can be calculated using Bernstein polynomials as:

$$\Delta X^k_{\text{surf,n}} = \sum_{j=0}^{q} \sum_{i=0}^{o} B^o_i(d_n) B^q_j(g_n) \left(P^k_{i,j} - P^{k-1}_{i,j}\right), \tag{2.4}$$

k is the design step, P the control point, B the Bernstein polynomial, and d_n and g_n the parametric coordinate that the surface point is mapped to [12].

2.1.1.3 Volume Mesh Deformation

Once the surface mesh points ($\mathbf{X}_{\text{surf}}$) have been translated the rest of the mesh points ($\mathbf{X}$) in the simulation domain must be moved to ensure mesh quality remains satisfactory. The CFD simulation software *SU*2 utilizes

a spring analogy based mesh deformation algorithm [20]. From the linear elasticity equations the mesh is deformed. Using the surface deformation from the blade surfaces as a Dirichlet boundary condition the whole volume deformation can be calculated as:

$$\mathbf{K}\Delta\mathbf{X}^d = \mathbf{T}\mathbf{X}_{\text{surf}}, \tag{2.5}$$

where a stiffness matrix ($\mathbf{K}$) is used while $\mathbf{T}$ is the projection matrix which re-orders $\Delta\mathbf{X}$ to $\mathbf{X}$. The coordinates of the mesh points for a given optimization step as:

$$\mathbf{X}^d = \mathbf{X}^{d-1} + \Delta\mathbf{X}^d, \tag{2.6}$$

This step's result is that new surface geometries can be realized in the simulation domain without a comprehensive re-meshing step, which is often time-intensive.

2.1.2 Flow Solver

Once a suitable mesh for the simulation domain has been made, a flow solver must be chosen. The flow solver is responsible for simulating the flow physics of interest/importance from which a performance metric is extracted for use in the optimization process. In Figure 2.6, the difference between flow solvers is compared between the RANS, URANS, LES flow solver methods, and an experimental result is shown using an identical blade shape.

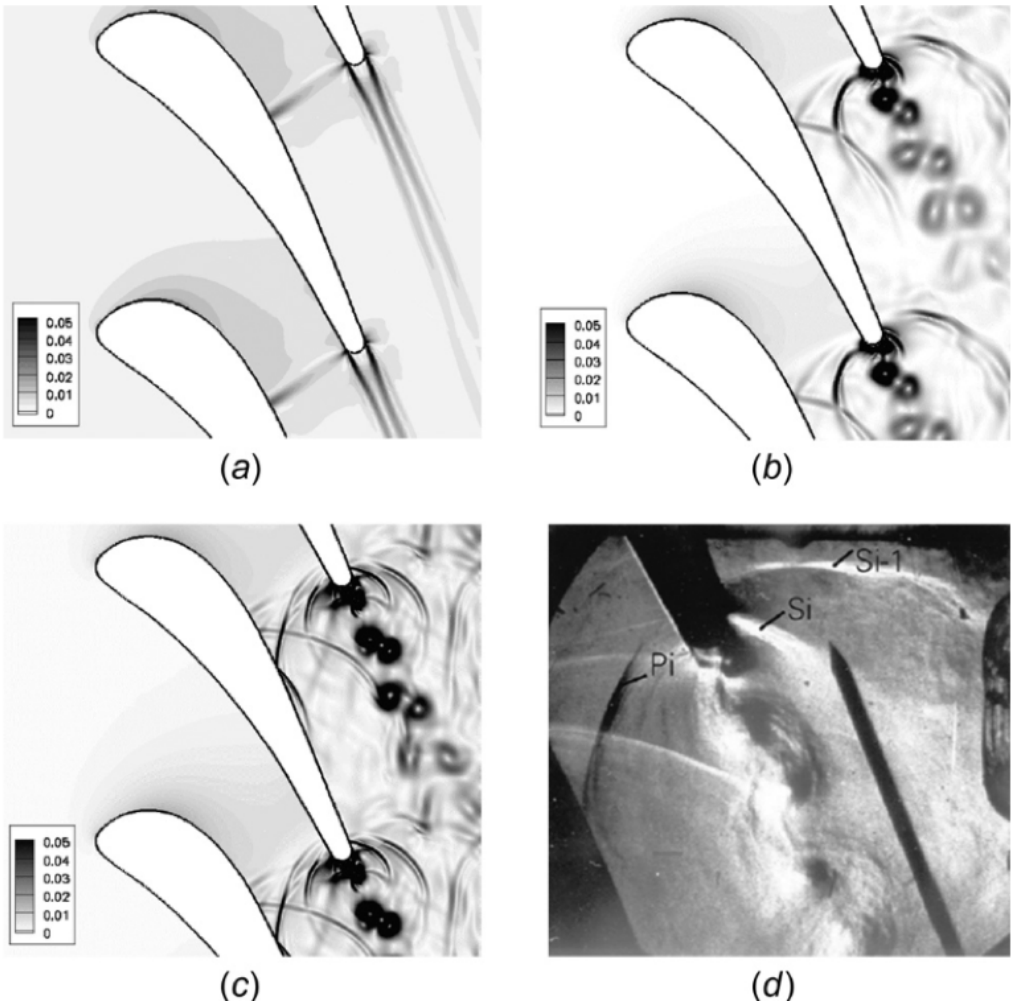

Fig. 2.6: Norm of the density gradient as obtained by use of (**a**) RANS, (**b**) URANS, (**c**) LES at single time instant, and (**d**) a direct view at the trailing edge flow dynamics as seen in experiment from Ref. [2].

The RANS simulation in (**a**) displays the least computationally expensive method of the three CFD methods. RANS has the most simplistic approach to turbulence produced and is easily seen by the low wake resolution. The image shown in (**b**) displays the URANS flow solution and displays a much higher fidelity of the trailing edge

wake. A more significant amount of flow physics is seen in the Kármán vortex street, an inherently unsteady fluid phenomenon related to uneven and time-dependent flow separation. Flow interactions are further resolved in the blade-blade plane. The final CFD solution is seen in (**c**) and is simulated using LES. In this solution, the vortex street is again seen, although with greater clarity and detail. Blade to blade plane fluctuations are also seen with enhanced resolution, but this comes at an increased computational cost. The actual experimental flow can be seen in (**d**).

	Points	Cells	Mean y^+	Geometry
Structured Meshes				
H1	97,000	62,000	12	3D
H2	636,000	500,000	5	3D
Unstructured Meshes				
T1	17,000	32,000	250	2D
T2	79,000	154,000	15	2D
T3	400,000	1,900,000	60	3D

Table 2.1: Grid Parameters from Ref. [2].

Table 2.1 shows five different meshes split between structured/unstructured and 2D/3D. The total cells in the volume range from $\mathcal{O}(10^4\text{-}10^6)$ and have varying y^+ values. As can be seen in Table 2.2, the computational cost for fidelity in the time domain increases drastically with cell volume. The processor number can reduce the elapsed time, but the total CPU time always increases when using a higher fidelity CFD model or increasing cell count.

	Mesh	CPU (h)	Elapsed time (h)	Processor number
RANS	H2	30	2.5	12
URANS	H2	336	28	12
LES	H1	20.5	1.3	16
	H2	267	16.7	16
	T1	2	0.1	32
	T2	73.2	2.3	32
	T3	950	23.8	40

Table 2.2: Computational Cost of CFD Methods from Ref. [2].

The CPU hours for the H2 mesh in Ref. [2] demonstrate that incorporating the unsteady effects in the computational method (URANS, LES) comes with an almost 10-fold increase in required CPU time. For optimizations that require many simulations of a blade, the time requirements should be lowered to the greatest extent while still incorporating the relevant unsteady flow physics. The least intensive method, RANS, is given a brief overview in the section below with more information found in Ref. [8].

2.1.2.1 RANS

In Reynolds Averaged Navier Stokes (RANS) simulations, the underlying flow physics are considered to be temporally and statistically averaged. The mean flow characteristics are resolved while the turbulence generated in the domain is modeled with a turbulence closure model such as k-ϵ or k-omega.

The terms Reynolds averaged refer to how the flow quantities are separated. As an example, if flow quantity (ϕ) is the actual flow quantity, it will be broken up into two aspects, a temporal mean value ($\overline{\phi}$) and a fluctuation (ϕ')[21]:

$$\phi = \overline{\phi} + \phi'. \tag{2.7}$$

With these aspects substituted into the Navier Stokes equation another temporal average is done while assuming that the average of a fluctuation is zero [21].

$$\overline{\overline{\phi}_1 \phi'_2} = \overline{\phi'} = 0, \tag{2.8}$$

For the in-compressible case this results in the following Equations.

$$\frac{\partial \overline{u_i}}{\partial t} + \frac{\partial \overline{u_i u_j}}{\partial x_j} = -\frac{1}{\rho}\frac{\partial \overline{p}}{\partial x_i} + \nu \frac{\partial^2 \overline{u}_i}{\partial x_j \partial x_j} - \frac{\partial \tau_{ij}}{\partial x_j}, \tag{2.9}$$

$$\frac{\partial \overline{u}_i}{\partial x_i} = 0, \tag{2.10}$$

$$\tau_{ij} = \overline{u_i' u_j'}. \tag{2.11}$$

A point should be made here that Equation 2.11 represents the Reynolds stress tensor, which models flow turbulence. There are various closure models for the Reynolds stress tensor, which have better or worse predictive performance in different turbulence conditions. Further information on the RANS method in SU2 can be found in Ref. [8].

The harmonic balance method can be used to incorporate unsteadiness into the simulation without too much additional cost.

2.1.2.2 Harmonic Balance

Harmonic balance is a method that can approximate periodic unsteady flow fields. The largest flow unsteadiness in turbomachinery stems from the wake, which harmonic balance can approximate. As the blade passing motion is a periodic condition, only the frequency is needed to recreate it. Using the Discrete Fourier Transform (DFT), the conservative flow values ($\tilde{\mathbf{U}}$) are reconstructed, further explanation of the mathematical basis can be seen in [4, 5].

$$\widehat{u}_k = \frac{1}{N}\sum_{n=0}^{N-1} \tilde{U}_n e^{-i w_k t_n}, \tag{2.12}$$

$$E_{k,n} = \frac{1}{N} e^{-i\omega_k t_n}, \tag{2.13}$$

$$\tilde{U} = E^{-1}\widehat{u}. \tag{2.14}$$

The blade wake can be perfectly recreated but would require many input frequencies to be resolved at an increased computational cost. A specific and finite number of frequencies (K) can be resolved for a chosen number of time instances (N) to lessen computational requirements while retaining reasonable wake fidelity[22]. The relation between resolved frequencies ($K_{\text{Frequency's}}$) and required time instances ($N_{\text{Time Instances}}$) for stability is shown as:

$$N_{\text{Time Instances}} = 2K_{\text{Frequency's}} + 1. \tag{2.15}$$

The impact of resolved frequencies resolved on the resulting wake for a 3D blade was investigated in [23] with the corresponding wake features shown in Figure 2.7,

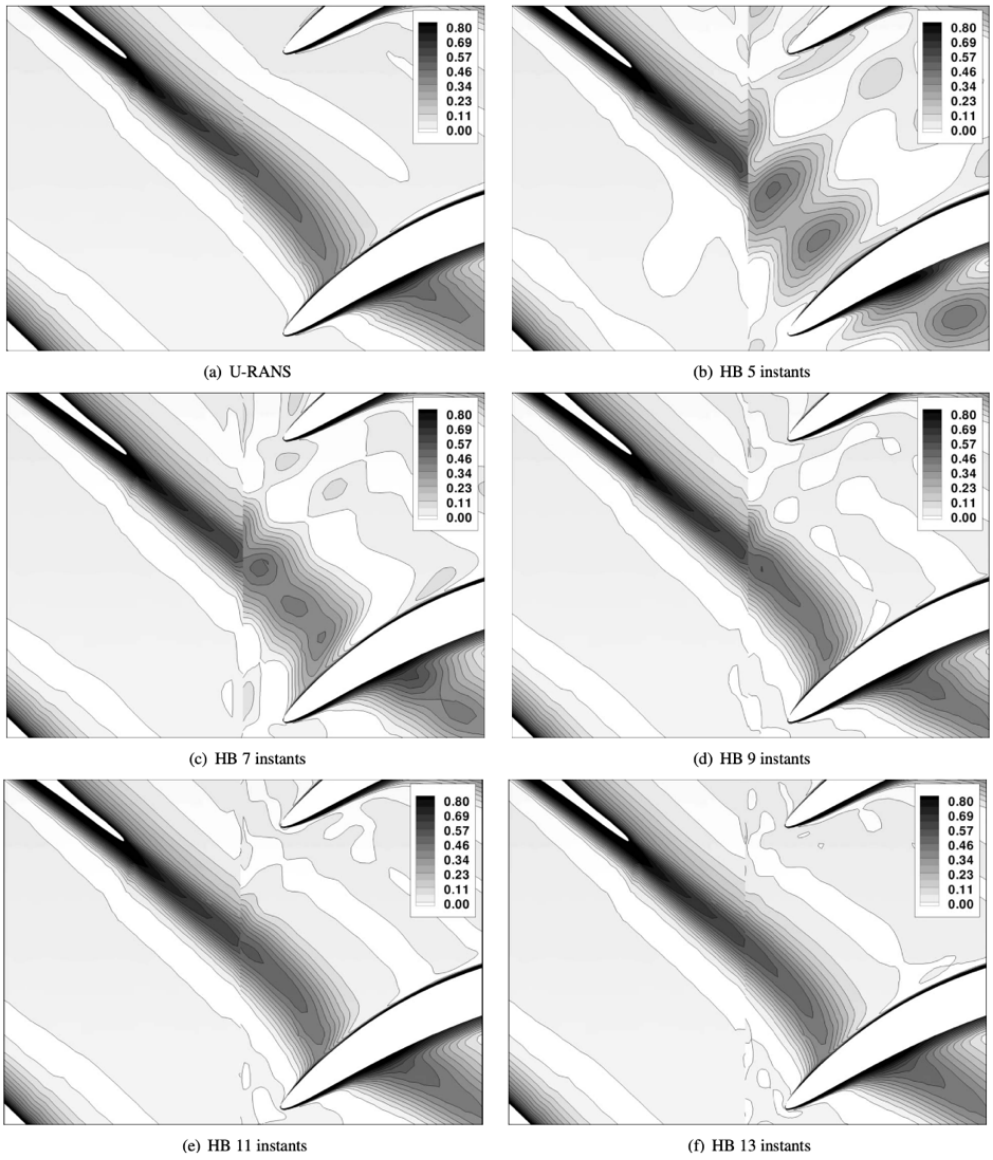

Fig. 2.7: Effect of Harmonic balance Frequency resolution on wake structure at interface from Ref. [23].

As the number of frequencies (and by extension time instances) increases, the resolved wake in the subsequent domain approaches agreement between the U-RANS and harmonic balance solutions. This agreement is beneficial from the perspective of accurately resolving the flow structures. The additional time instances require increasing memory requirements to calculate flow conditions. Time requirement scaling can be seen in Figure 2.8. While the time needed for harmonic balance is more expensive than a steady-state simulation, it is not as expensive as a fully time-accurate simulation. While many time instances are required to resolve flow structures accurately, there is a lessor requirement for a dimensionless parameter. The pressure loss coefficient in Figure 2.9 shows that of the time instances required for an accurate model is only half of what is needed to model the flow structure in Figure 2.7. This low requirement for time instances indicates a reduction in the computational cost required to optimize a dimensionless parameter.

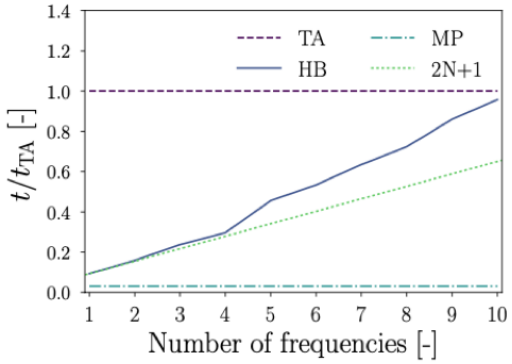

Fig. 2.8: Computational Cost for Harmonic Balance compared to time-accurate method for increasing number of resolved frequencies from Ref.[4].

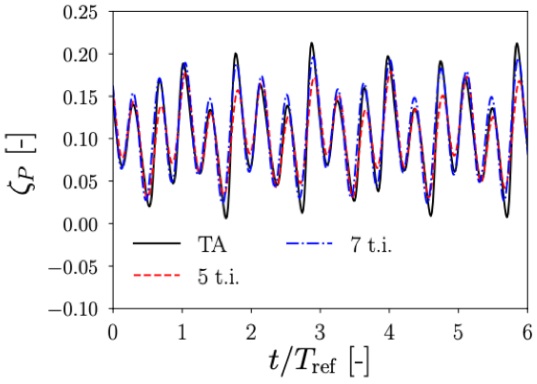

Fig. 2.9: Harmonic Balance Accuracy between time instances (t.i.) and time-accurate flow parameter variation from Ref.[4].

2.1.2.3 Interface Methods

A moving domain is used within a multizone turbomachinery simulation to represent a rotating blade and must be interfaced with the stationary domain. This interface introduces a source of error depending on the context and is discussed in the next sections. There are two interface methods of interest for the current work: the sliding mesh interpolation method and the mixing plane method.

Sliding Mesh In the sliding mesh approach, the fluid domain interfaces use the mesh cells at the outlet and inlet of the two domains and directly interpolates the flow quantities. This method's limitation is that the number of cells on the interface is equal in both domains. A drawback of this approach is that the stator and rotor domains must be of equal pitch or some whole integer factor. As shown in Figure 2.10, the pitch of two stator blades is exactly 7-pitch lengths of the rotor.

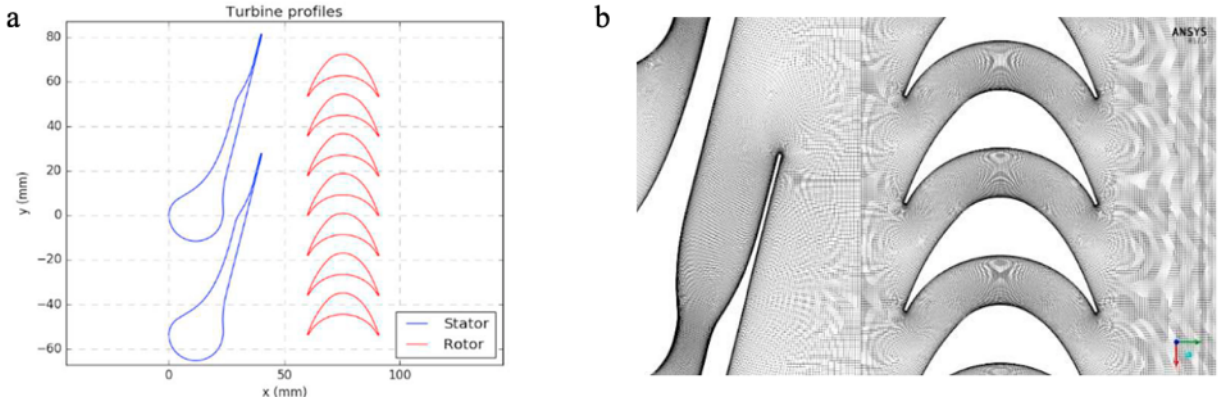

Fig. 2.10: Example of Sliding mesh from Ref. [24].

The sliding mesh interface is useful as the flow quantities can be directly interpolated and passed onto the next cell. The impact of this interface method has been studied with both steady and unsteady methods.

The differences between steady and unsteady quantities were compared and seen in Table 2.3. It should be noted that in these simulations, the stator-rotor gap was 50% of the rotor chord. The differences between some parameters, such as isentropic efficiency and rotor torque, are relatively small, while others, such as domain level (Stator/Rotor) entropy creation, are much different.

Quantities	Steady Simulation	Unsteady Simulation	Quantities	Steady Simulation	Unsteady Simulation
Stator Pressure Coefficient	0.1000	0.1022	Stator Entropy Creation (J/(kg.K))	3.528	3.174
Rotor Blade Torque (N.m/m)	2.6299	2.6255	Rotor Entropy Creation (J/(kg.K))	3.215	3.492
Total to total Isentropic efficiency	0.9193	0.9179			

Table 2.3: Steady/unsteady simulations performance metric comparison from Ref. [24].

Mixing plane A mixing plane is a fluid interface method that determines how fluid properties are transported from one interface to the next. The main idea behind a mixing plane interface is to employ some averaging procedure at the interface, which smooths the flow non-uniformity. The averaged quantities are then distributed to the interface output. The mixing plane can impart a steep flow entropy jump in the case of fully mixed-out flow. The entropy jump stems from the averaging procedure [7], which can take the form as below:

$$FLUX_{jmix} = FLUX_{avg,jmix} + F_{ext}(FLUX_{jmix-1} - FLUX_{avg,jmix-1}). \tag{2.16}$$

A physical understanding of the Equation 2.16 operation can be seen in Figure 2.11. Various drawbacks occur with this method, which has been briefly stated in Ref. [7]:

> "This model works very well for subsonic flow, but for super- sonic relative flow at the mixing plane extrapolation of the flow angle on the downstream side can give erroneous results. "

as well as in Ref. [25]:

> "The present results show that the steady mixing-plane method considerably underpredicts the stage efficiency at a small stator–rotor gap, compared with unsteady calculations."

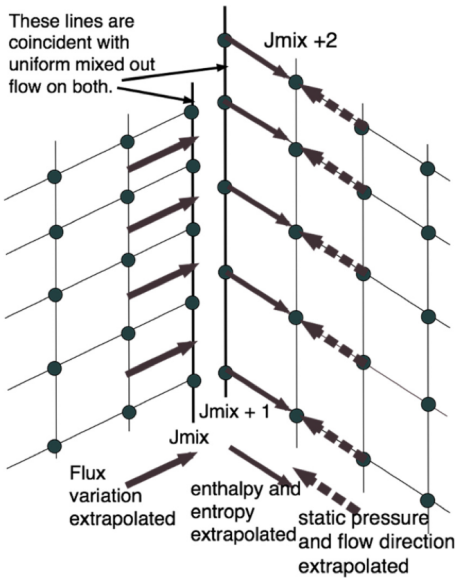

Fig. 2.11: Mixing Plane Treatment from Ref. [7].

The mixing plane interface can implement different averaging methods such as area or mass-flow averaging, which give preference to spatial or high momentum flow areas, respectively. Another useful averaging technique is the mixed-out average, which averages the flow quantities in such a way as to reproduce the flow conditions if all the entropy of mixing the flow over a long distance is captured. For typical turbomachinery applications, the mass-flow averaging technique is beneficial as it preserves entropy fluxes through the interface. In contrast, the mixed-out averaging tends to over-estimate entropy creation [6].

2.1.3 Gradient Solver

Gradient-based algorithms are quicker options for converging to an optimal point but require extra information for the algorithm to work. The additional information is that the algorithm has the gradient of the design vector, which shows how a design variable change will affect the objective value before the design step is taken. The gradient's actual calculation is a more complicated point, and two standard methods are explained in the following sections.

2.1.3.1 Finite Difference

The finite difference method of obtaining objective sensitivities is the straightforward solution of multiple simulations of small perturbations (ϵ) on the design variables. The difference can be seen with a first-order forward difference Equation 2.17 or central difference Equation 2.18.

$$\frac{dJ}{d\alpha_i} = \frac{J(\alpha_i + \epsilon) - J(\alpha_i)}{\epsilon}, \tag{2.17}$$

$$\frac{dJ}{d\alpha_i} = \frac{J(\alpha_i + \epsilon) - J(\alpha_i - \epsilon)}{2\epsilon}. \tag{2.18}$$

The finite difference approach has a couple of detracting properties with a high computational cost for problems with many design variables and perturbation size affecting resulting sensitivity accuracy. The high computational cost stems from each sensitivity value requiring one or two extra direct simulations of the flow. In typical optimization settings for 3D blades, the number of design variables can be large to have a larger design space and for an optimum design. Optimization problems require iterative gradient evaluations, with each direct simulation requiring a non-trivial amount of wall clock time. Extra direct simulations lead to optimizations that quickly become in-feasible in typical design workflows by requiring many concurrent simulations or long serial computation times.

2.1.3.2 Adjoint Approach

In the adjoint approach, the objective function (J) and simulation residuals ($\mathbf{R}$) are a function of 2 variables, the volumetric mesh of the design vector $\mathbf{X}(\alpha)$, and the flow field conservative values $\mathbf{U}(\alpha)$ [10].

$$J[\mathbf{U}(\alpha), \mathbf{X}(\alpha)], \tag{2.19}$$

$$\mathbf{R}[\mathbf{U}(\alpha), \mathbf{X}(\alpha)] = 0. \tag{2.20}$$

With this breakdown, the objective function is made of multiple parts. One part is responsible for how the flow field is affected by the design vector, and another responsible for how the objective function changes with respect to changes in the flow field.

$$\frac{dJ}{d\alpha} = \frac{\partial J}{\partial \mathbf{U}}\frac{\partial \mathbf{U}}{\partial \alpha} + \frac{\partial J}{\partial \mathbf{X}}\frac{\partial \mathbf{X}}{\partial \alpha}, \tag{2.21}$$

$$\frac{dR}{d\alpha} = \frac{\partial \mathbf{R}}{\partial \mathbf{U}}\frac{\partial \mathbf{U}}{\partial \alpha} + \frac{\partial \mathbf{R}}{\partial \mathbf{X}}\frac{\partial \mathbf{X}}{\partial \alpha} = 0. \tag{2.22}$$

Using the knowledge that physical flow fields are conservative Equation 2.20, the objective function total derivative and total residual derivative are combined into the adjoint vector Equation 2.24[10].

$$\frac{dU}{d\alpha} = -\frac{\partial \mathbf{R}}{\partial \mathbf{U}}^{-1}\left[\frac{\partial \mathbf{R}}{\partial \mathbf{X}}\frac{\partial \mathbf{X}}{\partial \alpha}\right], \tag{2.23}$$

$$\frac{dJ}{d\alpha} = -\frac{\partial J}{\partial \mathbf{U}}\left[\frac{\partial \mathbf{R}}{\partial \mathbf{U}}\right]^{-1}\frac{\partial \mathbf{R}}{\partial \mathbf{X}}\frac{\partial \mathbf{X}}{\partial \alpha} + \frac{\partial J}{\partial \mathbf{X}}\frac{\partial \mathbf{X}}{\partial \alpha}. \tag{2.24}$$

The objective function gradients for all design variables can be calculated from a single adjoint solution to the problem using the adjoint vector.

2.1.4 Optimization Algorithm

The optimization algorithm is used to determine how the design variables should be perturbed to reach the maximum or minimum; for convenience shall be referred to as a minimum. The optimization process begins with an initial design vector, perturbs the design variables, and then evaluates the objective function at this new design point. The algorithm then uses the new objective function value to determine the next perturbation.

This process continues until the optimization converges to a solution that satisfies its constraints.

A survey of different optimization algorithms was done to examine performance and costs in Ref.[9]. Using an aircraft wing as the object to be optimized for the lowest drag and free form deformation box as the design vector, the resulting drag, total iterations, and processing time can be seen in Table 2.4. A mesh cell count of around 450,000 was used.

Optimizer	Drag (counts)	Iterations	Proc-hours	
SLSQP	221.16	23	2.56	Gradient Based
IPOPT	221.15	40	2.69	Gradient Based
PSQP	221.15	29	3.70	Gradient Based
GCCMA	221.16	81	4.57	Gradient Based
SNOPT	221.16	40	5.81	Gradient Based
CONMIN	221.16	98	33.61	Gradient Based
NOMAD	221.91	375	40.23	Gradient Free
ALPSO	221.15	8128	1695.72	Gradient Free
NSGA2	221.98	12757	2744.16	Gradient Free

Table 2.4: Optimization Algorithm Comparison from Ref. [9].

In Table 2.4, the optimal objective value that all algorithms exited at was around the same value, with all gradient-based algorithms converging almost precisely to the same value. The terms gradient-based and gradient-free refer to whether the optimizer uses the gradient. The gradient contains information on how much a variable's perturbation will change the function or quantity of interest. The Gradient-based algorithms in Table 2.4 share a much lower iteration count than gradient-free algorithms. Of the gradient-based algorithms, the quickest on both iteration number and processing time is SLSQP, which is based on sequential least squares programming algorithm [9]. The difference in iteration number and processing time is not proportional across algorithms, and thus a single parameter can not be used as a basis for algorithm selection.

2.2 Current Optimization Works

2.2.1 2D Optimization with Harmonic Balance and Mixing Plane Methods

In work done in Ref.[4] an FFD box was used for optimization on a 2D turbine design with a stator and rotor. In this work, an optimization was done with both mixing plane and harmonic balance methods. The optimization trends can be seen in Figure 2.12 with two different configurations with different boundary conditions. In both conditions, the harmonic balance optimized design results in better performance after optimization than the mixing plane optimized design.

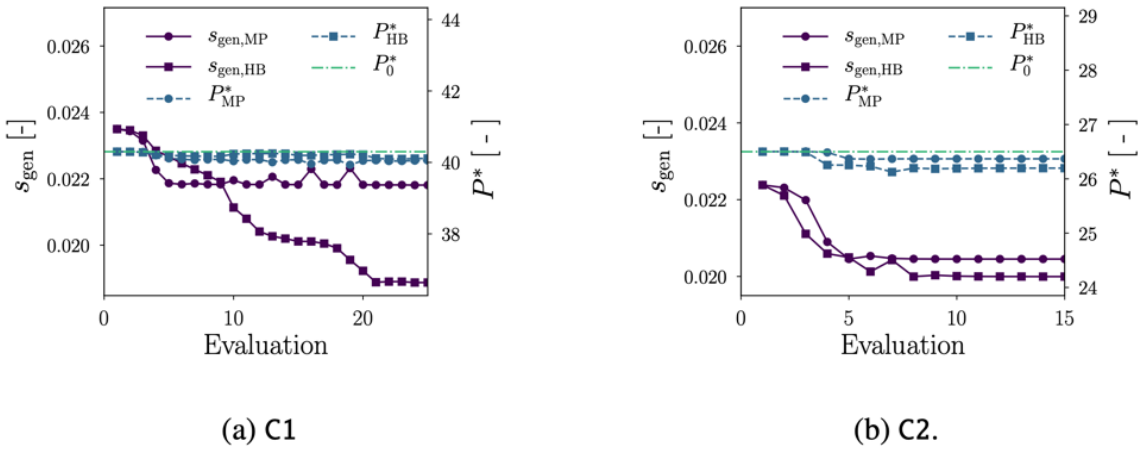

Fig. 2.12: 2D harmonic balance and mixing plane optimization trends from Ref. [4].

2.2.2 3D FFD Mixing Plane Optimization

An extension into 3D design problems was done in Ref. [8] by performing an optimization using FFD boxes and the mixing plane method. The optimization shows a tremendous reduction in entropy generation from the baseline design as seen in Figure 2.13 (**b**). Because the blades were 3D, an interesting result that the blades deformed into non-prismatic blades was obtained. The optimal blade profiles vary along the span with a different shape at the hub than the shroud, as seen in (**a**).

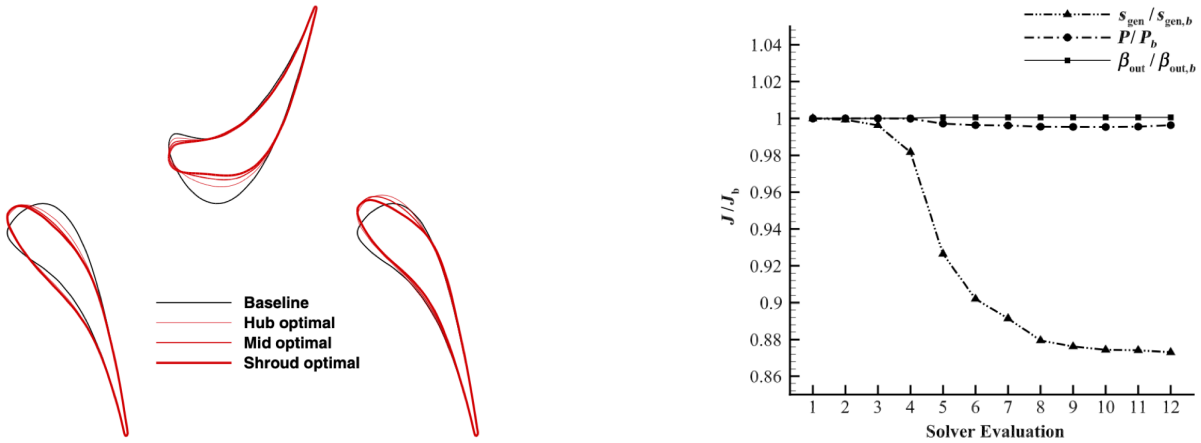

(a) 3D FFD mixing plane optimization blade shapes. **(b)** 3D FFD mixing plane optimization trend.

Fig. 2.13: (**a**) 3D mixing plane optimized blade shapes using FFD box and (**b**) Objective value trend from Ref. [8].

2.3 Losses in Turbomachinery

There are many ways to quantify total performance within turbomachinery or estimate some type of lost work within a stage. The two main parameters are often pressure loss coefficients or entropy generation created in the turbomachinery stage. The subsequent chapters will go over different parameters that can be used to estimate some aspect of turbomachinery performance.

A design objective typically used is the enthalpy loss coefficient ($\zeta_{turbine}$) [14, 26] or the entropy generation (s_{gen}) [4] that uses the spouting velocity (V) and the inlet temperature ($T_{0,\text{in}}$) which can be seen as:

$$\zeta_{turbine} = \frac{h_2 - h_{2s}}{h_{02} - h_2}, \tag{2.25}$$

$$s_{\text{gen}} = \frac{\Delta s}{V^2/T_{0,\text{ inlet}}}. \tag{2.26}$$

The parameter ζ encompasses all loss sources within a turbine stage and provides a comprehensive value for the amount of work which is lost due to irreversible effects. The stage enthalpys (h) are the only variables which are needed for calculation. Alternatively under an ideal gas assumption the irreversible work from an arbitrary reference point can be calculated from just the temperature and pressure as:

$$s - s_{\text{ref}} = C_p \cdot ln(T/T_{\text{ref}}) - R \cdot ln(P/P_{\text{ref}}). \tag{2.27}$$

Tracking the entropy through a fluid domain is useful as it is a state variable. Another added benefit of monitoring entropy is that it is not based on empirical relations, which can change depending on the fluid context, i.e., turbines and compressors.

There are known mechanisms for how entropy is created in a fluid domain and under what circumstances. These mechanisms are explained in subsequent sections with typical estimation techniques.

2.3.1 Loss Mechanisms

There are three primary sources of entropy creation, of which points 1 and 3 will be discussed in subsequent sections.

> "1 Viscous friction in either boundary layers or free shear layers. The latter include the mixing process in, for example, a leakage jet.
> 2 Heat transfer across finite temperature differences, e.g., from the mainstream flow to a flow of coolant gas.
> 3 Nonequilibrius processes such as occur in very rapid expansions or in shock waves "
> Quoted from Ref. [14].

2.3.1.1 Shock Loss

Shock losses are only seen in turbomachines that operate above Mach $\geq$ 0.8. Shocks are significant sources of entropy generation as a nonequilibrius process and can be seen in both compressor and turbine stages. Entropy generated from shocks can be approximated [14] with :

$$\Delta s \approx R\frac{\gamma+1}{12\gamma^2}\left(\frac{\Delta P}{P_1}\right)^3 + O\left(\frac{\Delta P}{P_1}\right)^4, \tag{2.28}$$

Using oblique shock theory and the flow normal to the created shock. Bow shocks and oblique shocks can be treated similarly using this approximation, with the major difference being the upstream velocity normal to the shock.

Within turbines, small shocks for low transonic machines are not too detrimental to overall efficiency [14] but can have tremendous effects on trailing edge losses due to mixing. Figure 2.14 shows the trailing edge losses within a transonic turbine stage while Figure 2.15 shows a marked increase in the loss from the shock wave system for exit Mach numbers above 0.8.

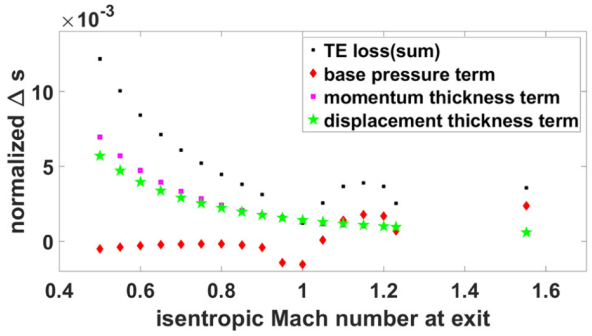

Fig. 2.14: Trailing edge losses within transonic turbine stage for increasing exit isentropic Mach number from Ref. [15].

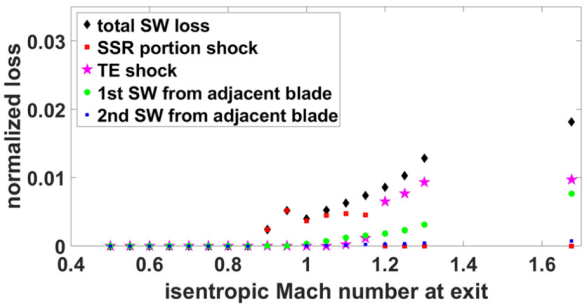

Fig. 2.15: Shock system losses within transonic turbine stage from Ref. [15].

The total shock wave loss was estimated using:

$$\Delta s_{SW} = C_v \frac{2\gamma(\gamma-1)}{3(\gamma+1)^2}(M^2_{\text{normal}} - 1)^3, \tag{2.29}$$

This loss mechanism estimation technique requires knowledge of the Mach number upstream and normal to the shock in question, fluid parameters of specific heat capacity at constant volume (C_v), and specific heat capacity ratio (γ). As can be seen from both Figure 2.14 and Equation 2.29 [15], the losses associated with shocks scale with increasing Mach number and are only relevant for flow Mach numbers greater than 0.8.

2.3.1.2 Boundary Layer Loss

Boundary layers are prevalent in any turbomachine due to the fluid's viscous effects interacting with a solid boundary. A no-slip condition is often placed on a wall or boundary, which enforces that the flow velocity at the boundary is 0. This boundary condition creates a velocity profile of 0 at the wall to the free stream velocity

(V_δ) at the boundary layer's edge. A general trend is that increases in flow velocity gradients in the boundary layer lead to a rise in entropy. A proposed expression for the entropy production rate per unit area [14] can be expressed as:

$$\dot{S}_{\text{a, bl}} = \int_0^\delta \frac{1}{T} \tau_{yx} dV_x. \tag{2.30}$$

The entropy production is dependent upon the shear stresses present within the boundary layer. Instead of referring to the entropy production rate, which is different in every machine/boundary layer, a non-dimensional dissipation coefficient (C_d)[14] can be used for comparison among different machines:

$$C_{\text{d}} = \frac{T\dot{S}_{\text{a, bl}}}{\rho \cdot V_\delta^3}. \tag{2.31}$$

2.3.1.3 Trailing Edge Loss

The trailing edge loss encompasses the mixing of the boundary layers present on both sides of the turbomachine blade surfaces as the flow exits the blade. Due to viscosity in the fluid when there is a mismatch between adjacent fluid properties energy will be lost as viscosity diffuses the non equal components such as velocity or temperature. A loss correlation for trailing edge losses [15] as:

$$\zeta_{TE} = \frac{-C_{pb}t}{w} + \frac{2\theta_1}{w} + \left(\frac{\delta_1^* + t}{w}\right)^2, \tag{2.32}$$

can be made which relies on a base pressure term (C_{pb}),

$$C_{pb} = \frac{P_b - P_{\text{ref}}}{\frac{1}{2}\rho u_{TE}^2}, \tag{2.33}$$

and can be calculated using the trailing edge thickness (t), momentum thickness (θ), displacement thickness ($\delta*$), and throat width (w).

2.3.2 Steady and Transient comparison

A study of the differences in 3D steady and unsteady simulations has been explored by tracking the aerodynamic loss in Ref. [16]. A direct demonstration of how loss is generated as a function of axial distance is shown in Figure 2.16 (**a**). The stator region is shown between the dashed red lines, while the rotor is between the dashed blue lines. A majority of loss is generated in and after the rotor, which is also the most complex fluid region. The region in Figure 2.16 (**b**) shows that wake-wake interactions, shocks, and boundary layer-shock interactions take place along the rotor and responsible for the majority of the loss.

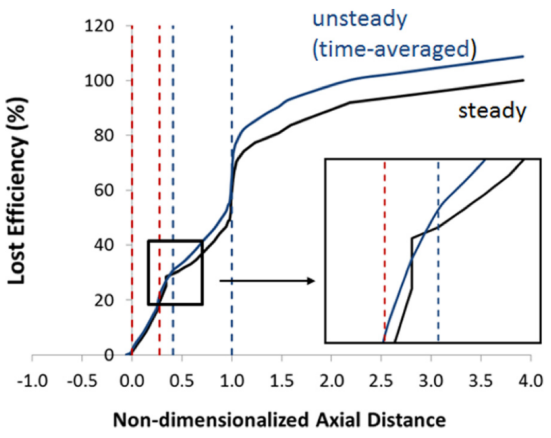

(**a**) Steady to Unsteady Loss Difference

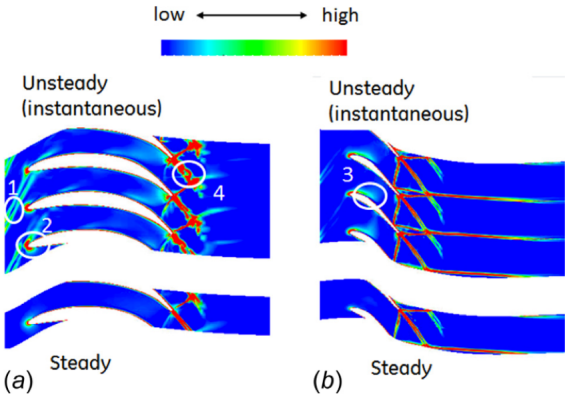

(**b**) Unsteady to Steady Entropy Generation of Rotor at (a) hub and (b) tip.

Fig. 2.16: Unsteady to Steady Entropy Generation from Ref. [16].

A further breakdown of loss is seen in Figure 2.17 (**b**) by sequentially changing boundary conditions (such as no-slip blade surfaces, leakage flows, etc.) to remove or lessen a loss source and calculating the difference from the baseline entropy trend seen in Figure 2.17 (**a**). The largest impact on loss stems from the rotor trailing edge, while the unsteady loss only accounts for around 10% of the total loss. The unsteady loss value was calculated by the difference in efficiency seen in Figure 2.16 (**a**).

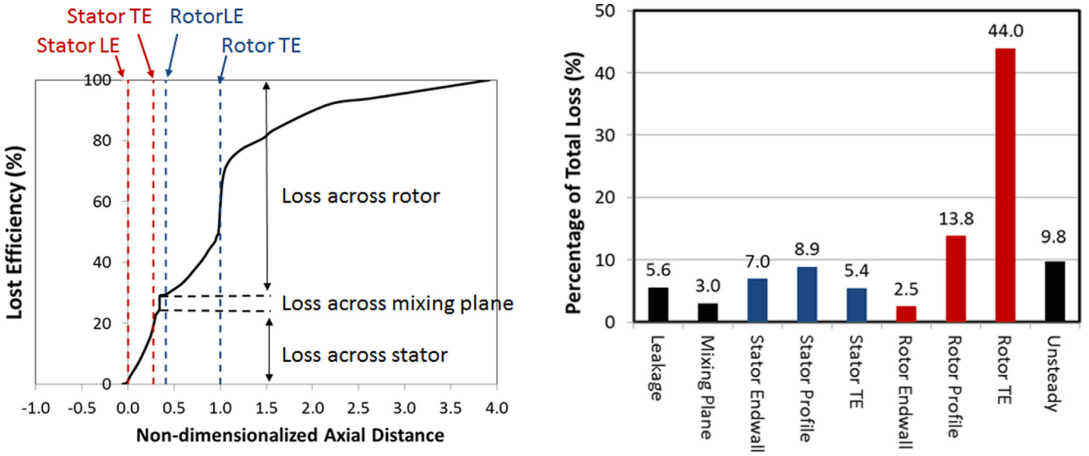

(**a**) Loss through axial distance

(**b**) Loss audit of turbine stage

Fig. 2.17: Loss Behavior through stage from Ref. [16]

.

Chapter 3

Methodology

3.1 Aerodynamic Design Chain

Parablade is a software tool written in python with a code branch, *feature_multizone_optimization*, dedicated to multizone turbomachinery optimization problems. The optimization code executes the following loop to produce an optimized design.

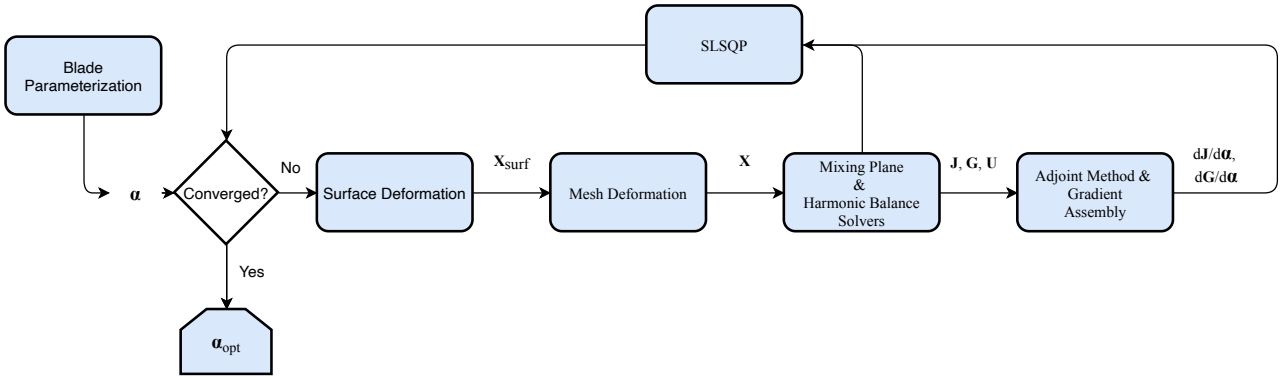

Fig. 3.1: Optimization Loop for mixing plane and harmonic balance optimizations.

For this work the objective function (J) to be minimized was the entropy generation rate (s_{gen}),

$$s_{gen} = \frac{s_{S1,out} - s_{S1,in}}{V_0^2/T_{0,in}} + \frac{s_{R1,out} - s_{R1,in}}{V_0^2/T_{0,in}} + \frac{s_{S2,out} - s_{S2,in}}{V_0^2/T_{0,in}}, \tag{3.1}$$

and only one inequality constraint (G) being the power (P) output:

$$P \geq \Delta h \cdot \dot{m}, \tag{3.2}$$

with h being the specific enthalpy and $\dot{m}$ the mass-flow rate.

The optimization algorithm used is the Sequential Least-Squares Programming (SLSQP) algorithm [27]. This algorithm is a first-order solver which is aided in using the gradients of the objective and constraint values. These gradients are calculated using the adjoint method in conjunction with the complex step method in the *Parablade* software. Further information on its implementation can be seen in Ref. [13]. The SLSQP algorithm was chosen as this is a gradient-based algorithm that speeds up time to optimization convergence and has been shown to work well in both external flow problems [9] and internal flow problems [8, 13].

3.2 Blade Parameterization

The software *Parablade* was used to perform the parameterization and optimization. This software package was selected as it has already been integrated and verified for use with both *SU*2 and Tecplot 360. It also supports a CAD-Based NURBS parameterization which was chosen for this work.

3.3 Flow and Adjoint Solution

For simulation, the opensource flow solver $SU2$ V.5 was used as it already incorporates the adjoint solver and deformation code. Further capability is gained using $SU2$ as the blade parameterization software *Parablade* has already been linked and tested for use with $SU2$ in Ref. [13]. The harmonic balance flow solver uses the SU2 branch $TMZHB\_Temp$ while the mixing plane simulation utilizes the $feature\_turbomachinery$ branch, and its accuracy was verified in [4].

A mass-averaged interface was selected for the mixing plane method to preserve entropy fluxes across the interface as recommended in Ref. [6]. For the harmonic balance method, a linear interpolation was done. The base design was simulated with both harmonic balance and mixing plane methods to understand where and why the two methods produce differences in flow features and entropy. Further detail is given in chapter 4. After the baseline design is simulated, an optimization was done with the mixing plane and harmonic balance methods. The optimized blade designs are compared to the simulation of the baseline design with both simulation methods afterward.

3.3.1 Gradient Computation

The gradient calculations for optimization were done using the adjoint method described in Equation 2.24 and implemented in conjunction with a complex step method in *Parablade*. Further information can be seen in Ref. [10] and Ref.[13].

3.3.2 Mesh Deformation

Blade surface deformation is extended to the volumetric mesh using the spring analogy method shown in subsubsection 2.1.1.3.

3.4 Post Processing

Data extraction for the flow fields was done using Tecplot 360 [28] and Python. Tecplot 360 has a Python-compatible API, which was used to extract the slices of interest in the fluid domain, while the Tecplot application was used to create other domain views. Other CFD post-processors such as Paraview were excluded from consideration as $SU2$ already incorporates data export to a Tecplot compatible file. Furthermore, the other tools used have already been tested and verified to work well with the Tecplot 360 software.

3.4.1 Performance Metrics

The entropy generation rate was used as the objective function for optimization, and the mass-flow averaged entropy was used for loss trend analysis. For loss trend comparisons, the mass-flow averaged entropy was extracted from a plane normal to the mean flow direction in the baseline and optimized designs. For optimization comparisons, the entropy difference is calculated as:

$$\Delta \langle s \rangle = \frac{\langle s \rangle_{Baseline} - \langle s \rangle_{OptimizedBlade}}{\langle s \rangle_{Baseline}}, \tag{3.3}$$

and is used to compare the optimized design to the baseline design. For the mixing plane and harmonic balance method comparison the difference is calculated as :

$$\Delta \langle s \rangle = \frac{\langle s \rangle_{MP} - \langle s \rangle_{HB}}{\langle s \rangle_{MP}}. \tag{3.4}$$

An important use of Equation 3.4 is that if $\Delta \langle s_{gen} \rangle = Constant$ the entropy generation rate as a function of axial distance between the compared trends are equal. The next important feature is that when the entropy difference is positive, the compared design performs better, i.e., generating less entropy, and conversely, when the difference is negative, the compared design is performing worse.

The mass-averaged entropy trends are captured for a quantitative view of lost work in the flow.

Chapter 4

Case Study

The Aachen test case [29] is a 1.5 stage turbine that operates in the transonic regime. All blades are prismatic. The design is originally an axial turbine with a 36:41:36 blade ratio, but for this research, it was simplified to 41 blades (N_{blades}) in each section, a blade ratio of 41:41:41. The blade ratio change was done to simplify the simulation domain. A deviation from the 1:1 interface cell ratio necessitates the use of phase-lag boundary conditions, which have not been implemented in *SU*2. The flow domain boundary conditions are reported in Table 4.1.

Boundary condition	Flow Quantity Imposed	Value
Inlet	Total Pressure	155,000 [Pa]
	Total Temperature	308 [K]
Outlet	Static Pressure	99,614 [Pa]
Blades	No-Slip	-
	Constant Heatflux	0 $\left[\frac{\text{w}}{\text{m}^2}\right]$
Hub	Symmetry	-
Shroud	Symmetry	-
Side Walls	Periodic	-
Interface$_{\text{Mixing Plane}}$	Massflow avg.	-
Interface$_{\text{Harmonic Balance}}$	Interpolation	-

Table 4.1: Aachen Machine boundary conditions.

The blade walls are assumed adiabatic. All hub and shroud surfaces can only be deformed tangentially to ensure a constant fluid domain area. In contrast, the walls have a periodic boundary condition which mirrors data to the opposite surface.

The same numerical schemes were used for both harmonic balance and mixing plane simulations and can be seen in Table 4.2.

Turbulence Model	SST
CFL	10
Convective Scheme	JST
Linear Solver	FGMRES
Preconditioner	LUSGS

Table 4.2: Numerical methods shared between harmonic balance and mixing plane simulations.

The SST turbulence model was used as this two-equation model has blended functionality for both free stream and near-wall regions[30]. As *SU*2 did not incorporate wall functions in the version used, a turbulence model with reasonable applicability for these flow conditions was selected. A CFL number of 10 was used to balance convergence time and stability. The FGMRES and LUSGS linear solver and preconditioner were selected to balance the computational cost and effectiveness [31].

The test case was meshed using the same starting blade shape and subsequently optimized using both harmonic balance and mixing plane simulation methods. After the optimizations were completed, the resulting flow fields

were post-processed by analyzing the quantitative flow features and extracting 50 linearly spaced surface slices normal to the mean axial-flow direction per blade domain.

The Mach number and relative Mach number contours are used to identify regions of potential interest for comparison. With the test case used in this investigation, there is minimal chance of shocks developing, and there is no heat transfer through the fluid domain boundaries. There are only two sources of entropy generation in the system.

1. Fluid Mixing
2. Profile losses/ Boundary layer losses

Regions of large fluid mixing losses would be expected to coincide with high Mach flow areas as mixing losses usually scale with flow velocity gradients [6]. Because the mass flow rate is similar in all test cases due to the same boundary conditions, if there is a higher flow velocity region, the flow velocity gradient would increase and is expected to show up in entropy contours.

4.1 Blade Parameterization

Using the thickness parameterization in *Parablade*, there are 19 total parameterization variables per blade section, of which only 13 are given to the optimizer and can be seen in Table 4.3.

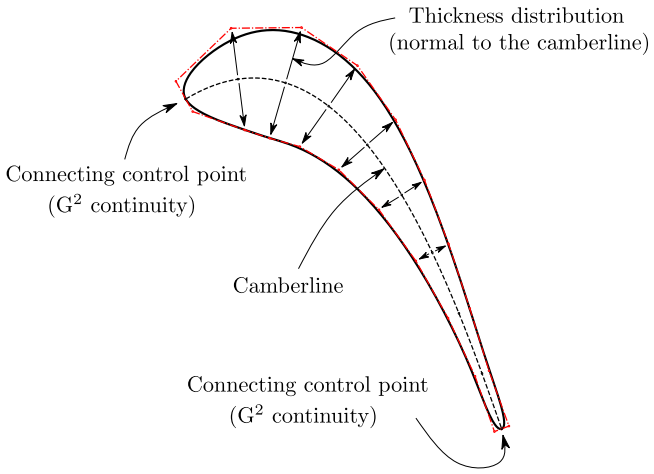

Fig. 4.1: Thickness blade section parameterization from Ref. [18].

Each 3D blade is split into five sections linearly spaced along the blade span, which are independently controlled by the optimizer for a total of 195 design variables given to the optimizer.

– Thickness Upper 1.	– Thickness Lower 1.	
– Thickness Upper 2.	– Thickness Lower 2.	– Stagger, ζ.
– Thickness Upper 3.	– Thickness Lower 3.	– Blade inlet angle, θ_{in}.
– Thickness Upper 4.	– Thickness Lower 4.	– Blade outlet angle, θ_{out}.
– Thickness Upper 5.	– Thickness Lower 5.	

Table 4.3: Optimization design variables for one section of a single blade.

Due to the number of design variables, finite difference gradient validation was omitted as previous works have shown acceptable agreement between adjoint and finite difference sensitivities in both harmonic balance [4] and mixing plane [13] methods.

4.2 Numerical Method

The flow solver is based on a finite volume method for spatial integration. The temporal integration is achieved through an implicit Euler method with a fixed Courant-Friedrichs-Lewy (CFL) number of 10. The convective fluxes are discretized using the second-order Jameson-Schmidt-Turkel (JST) [32] scheme. The choice of a second-order scheme over an upwind scheme such as ROE was due to the simulation remaining relatively stable in convergence while also producing a stage efficiency and flow velocity distribution similar to previous works such as Ref. [8]. The flow solver utilizes the Flexible Generalized Minimal Residual method (FGMRES) [33], which is a more stable iterative method with a Lower-Upper Symmetric Gauss-Seidel (LUSGS) preconditioner to reduce memory requirements. Six orders of reduction in the maximum zone residual were achieved in 12,000 and 13,500 iterations for mixing plane and harmonic balance methods.

Within the constraints of this research the harmonic balance method was restricted to a single resolved harmonic. The harmonic chosen was the fundamental blade passing frequency. The blade passing rotation speed (ω) is directly seen from the design rotation speed and blade number as:

$$\Omega_{\mathrm{HB}} = N_{blade} \cdot \omega. \tag{4.1}$$

The overall period and frequencies set for the solver can be seen in Table 4.4.

Setting (symbol) [unit]	value
Period (τ) [s]	$4.181{\cdot}10^{-4}$
frequency (Ω_{HB}) $\left[\frac{1}{s}\right]$	0.0, 15026.5, -15026.5

Table 4.4: Harmonic balance settings.

4.3 Grid Convergence Study

The appropriate mesh choice was made after analyzing the grid convergence study results and examining each grid's computational cost. In Figure 4.2 (**a**) the number of elements for a given mesh index are seen while Figure 4.2 (**b**) shows the resulting entropy generation rate. Meshes with element counts below 500k have a strong sensitivity to element number, but after around 600K elements, the values do not change substantially. Both harmonic balance and mixing plane simulations have a similar trend in entropy generation value, but the harmonic balance simulations consistently produce greater entropy generation rates.

Meshes with greater than 1.8M elements show a large fluctuation in entropy generation rate. This could be due to a multitude of factors such as boundary layer refinement, spanwise element count, or element skew but was not investigated further as other research constraints disqualified these meshes from further use.

Mesh Name	# of Elements
M0	129,450
M1	259,950
M2	491,250
M3	807,780
M4	1,297,080
M5	1,819,590
M6	2,406,570

(**a**)Number of elements in meshes used for grid convergence study.

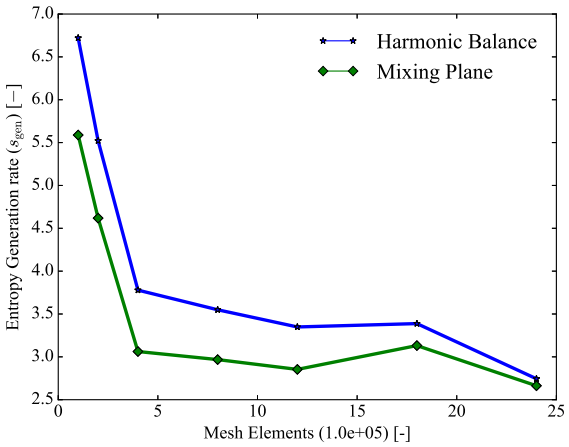

(**b**) Grid Convergence for Aachen case of Steady State and Harmonic balance method using one harmonic.

Fig. 4.2: Mesh grid convergence study results.

Further requirements were imposed on the mesh used in the form of available computational resources. Two hard limits were imposed upon the mesh computational resources used in the amount of memory (RAM) required and the wall-clock time needed. A high-performance cluster (HPC) was used with a constraint of a maximum of 20 processor cores and 128 Gb of memory. The time spent for a single job or analysis is also capped at 72 hrs of real-time/wall-clock time. The mesh used for optimization and comparison is seen in Figure 4.3

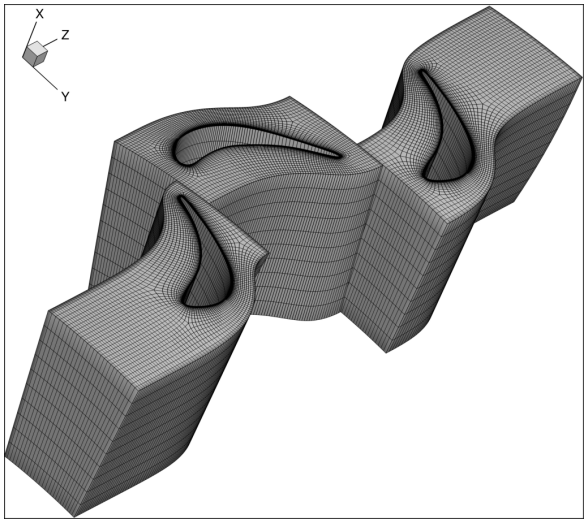

Fig. 4.3: Test case mesh used for optimization.

4.4 Computational Resources

Three-dimensional simulations require a large number of computational resources for both the direct and adjoint solvers. Typical design flows have limitations on either time or storage, which becomes the trade-off for design. The harmonic balance method has been shown to have a reduced cost compared to a time-accurate method [4] but is still more expensive than a steady solver. An initial run of the direct and adjoint solvers was done to understand the computational requirement scaling for the meshes seen in Figure 4.2.

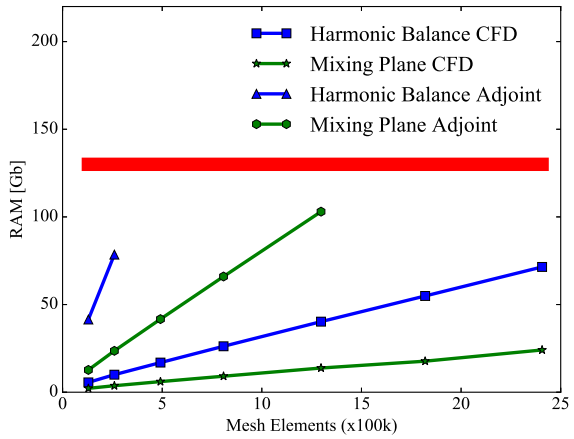

(a) Memory requirements requirements for meshes in grid convergence study^{+}.

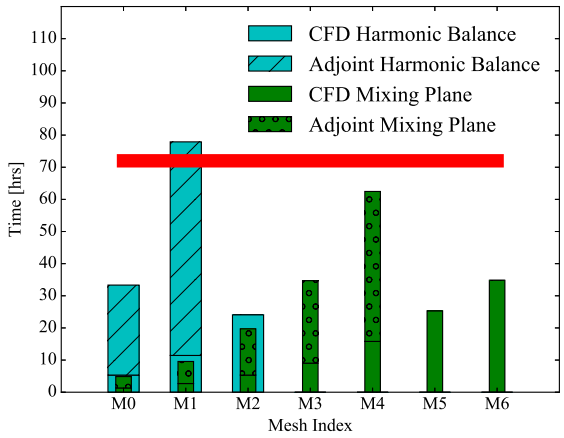

(b) Time requirements for all meshes indexes*.

Fig. 4.4: (**a**) Ram requirements for a mesh for a given element number. (**b**) design step time requirements for each mesh index . $^{+}$ - Missing trend values due to constraint value being exceeded during execution. * - Some bars missing due to either insufficient convergence or memory constraint violation.

The dominating constraint is seen in the RAM requirements for the adjoint solver in Figure 4.2 (**a**). The blue line with triangular markers denotes the harmonic balance adjoint solver memory used, which ends after two meshes and does not have a value for meshes with above 500k elements due to exceeding the memory constraint. The mixing plane adjoint solver also exceeds the memory constraint for meshes above 1.5M elements. As the final mesh must be optimized with the same mesh for an accurate comparison, the meshes above 500k elements were disqualified from further consideration.

In Figure 4.2 (**b**), the time requirements for one direct solution and two adjoint solutions for both harmonic balance and mixing plane solvers are shown. The cyan bars represent harmonic balance, while the green denotes the mixing plane solver. Not all mesh indexes have a corresponding value due to either the maximum mesh residual not converging to at least six orders of magnitude in change or the mesh violating the previous memory constraint. The direct (CFD) solvers for the harmonic balance method cease after the M3 mesh with 807k elements due to insufficient convergence, which can be seen in Figure A.1. The adjoint solvers for both harmonic balance and mixing plane methods are absent for meshes above M1 and M4 due to exceeding the memory constraint. From this data, the only mesh which is usable is the M0 mesh with 129k elements. The next largest mesh exceeds the time constraint by a couple of hours and would not be suitable. A mesh with an element count between M0 and M1 was not made as the new mesh would not substantially change the flow field resolved or provide any drastically different insights and would be at the cost of dramatically increasing optimization time.

From the data seen in Figure 4.4, the best choice of mesh is the M0 mesh with 129k elements. This atypical choice was made based on the computational resources available to compare the simulation method optimization results. As the solution is not grid independent for each of the optimized blade shapes, a grid converged mesh of 600k elements is used in a final comparison.

In Table 4.5, the computational scaling for memory and simulation time for six orders of convergence are displayed for the mixing plane and single harmonic balance method. From the time scaling of the harmonic balance adjoint solution, a strong motivation for reducing mesh size is seen as nearly 90 minutes of additional processing time is required for every ten-thousand elements added. Memory also balloons quickly in the harmonic balance adjoint and requires 2.837 Gb per ten-thousand elements added to a mesh. For a grid converged harmonic balance optimization, a minimum memory size of 183 Gb and 206.2 hours of wall clock time is needed per design step compared to a modest 52 Gb and 28.8 hours for the mixing plane optimization step.

	Memory $[\frac{Gb}{10kElements}]$		Time $[\frac{hrs}{10kElements}]$	
	HB	MP	HB	MP
Direct	0.296	0.099	.508	0.136
Adjoint	2.837	0.785	1.473	0.171

Table 4.5: Grid Computational time and memory scaling for mixing plane and single harmonic harmonic balance direct and adjoint solutions.

Chapter 5

Results and Discussion

In this chapter, the thesis results are shown and explained. First, the flow differences between the harmonic balance and mixing plane method are analyzed. Next, the blade surface sensitivities of the harmonic balance and mixing plane methods are examined. Afterward, the optimization convergence and results of the harmonic balance and mixing plane method optimization are shown. The hybrid design hypothesis results are shown last.

The flow features are examined on the secondary and blade to blade planes for both the initial differences between the harmonic balance and mixing plane simulations and designs resulting from optimization. All flow contours are averaged from the resolved time instants in the harmonic balance case. The mass averaged entropy trends are discussed in every case to quantify the location of performance differences. From the results of optimization, additional hypotheses were made and tested. Hypothesis analysis only includes mass-averaged entropy trends as the flow features found for the specific flow solver method are assumed to behave similarly.

5.1 Flow field computed by the MP and HB method

To quantify the impact of the flow method, i.e., steady or unsteady, on the entropy generation seen in Figure 4.2 (**b**) and explain why the harmonic balance simulations have a larger entropy generation rate in all cases, the Aachen design was simulated using the harmonic balance and mixing plane methods. Each interface and span contour plot displays the harmonic balance result on the left and mixing plane on the right. For interface plots, the top two plots show the previous domain's outlet (input of flow information) while the bottom plots display the inlet of the next domain (output of flow information). The interfaces are examined first to identify how well flow information is passed between zones and see how the bulk quantities are changed.

As there are only two sources of loss expected, profile and mixing, the Mach and entropy contours are shown. The Mach contours are used to identify regions with large velocity gradients in which mixing may be prevalent. Mixing losses are spread over an area and show diffuse regions of higher than average entropy in an entropy contour. The entropy contour will also show the blade wake and contains the profile loss. There is a steep velocity gradient in the boundary layer due to the no-slip boundary condition. The boundary layer results in very localized entropy generation. After the interfaces have been analyzed, the flow contours at the hub, mid-span, and shroud positions are shown to understand what flow structures may be responsible for the interfaces' changes.

5.1.1 Flow field on secondary planes

5.1.1.1 Stator 1 - Rotor 1

The first interface is the Stator 1 and Rotor 1 interface; The Mach number can be seen in Figure 5.1 and entropy in Figure 5.2. The harmonic balance and mixing plane methods have similar Stator 1 outlet contours as seen in the top two contours of Figure 5.1. The harmonic balance contour shows a larger relative Mach number flow area at the hub to the wake's right. The wake is identifiable as the rectangular region of slower flow. The

maximal Mach value is above 0.55 in harmonic balance, while the mixing plane contour shows a slightly lower value. The span-wise flow contour shapes between the two methods are relatively similar. Harmonic balance results show a higher average Mach value but lower variation than when using the mixing plane method. An increase in entropy creation is expected from the higher flow velocity seen in the harmonic balance result.

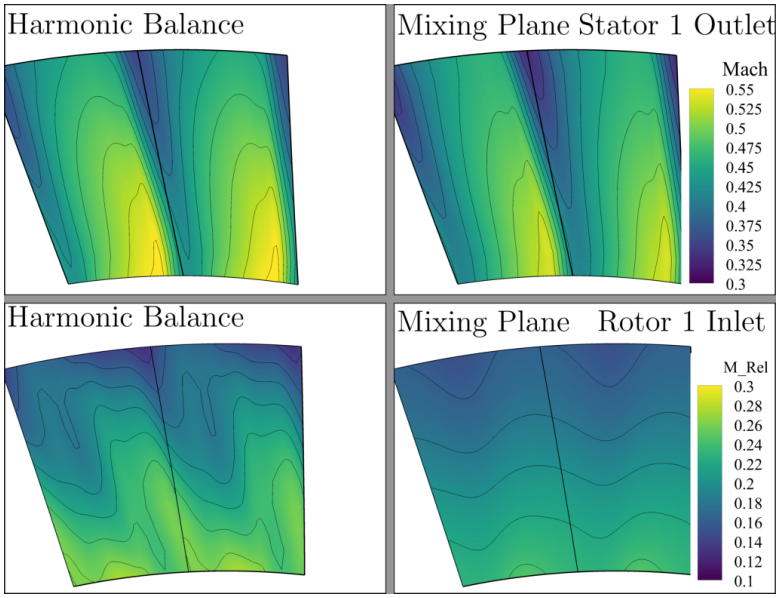

Fig. 5.1: Baseline Geometry Stator 1- Rotor 1 interface Mach and relative Mach number contours. The left column shows harmonic balance results while the right column shows the mixing plane results. The top row is the Stator 1 outlet while the bottom row is the Rotor 1 inlet.

The Rotor 1 mixing plane's inlet looks very different from the Stator 1 outlet. The mixing plane wholly erased the flow features associated with the wake or any span-wise flow structure from the outlet, as expected. The harmonic balance Rotor 1 inlet shows a poor representation of the Stator 1 outlet but tries to capture the overall features. There are some span-wise flow features with a faster flow at the hub than at the shroud, but a clear representation has not been achieved.

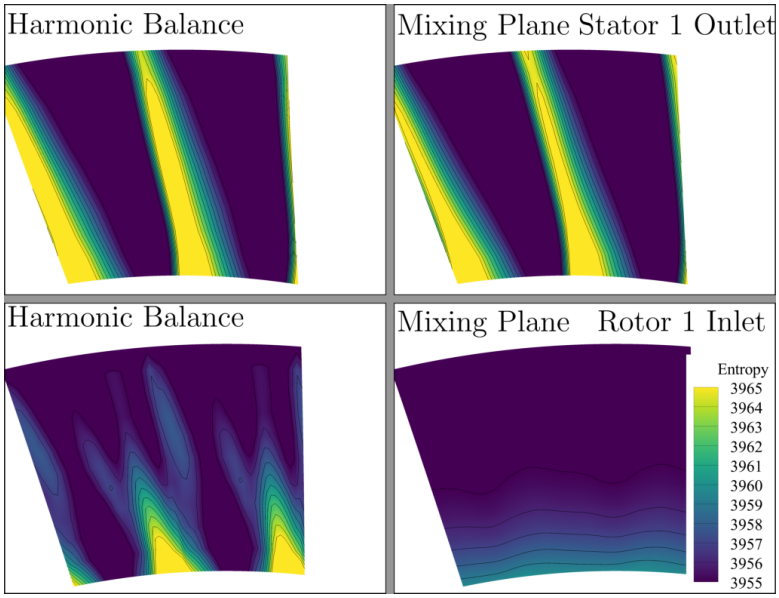

Fig. 5.2: Baseline Geometry Stator 1- Rotor 1 interface entropy contours. The left column shows harmonic balance results, while the right column shows the mixing plane results. The top row is the Stator 1 outlet, while the bottom row is the Rotor 1 inlet.

Figure 5.2 shows the entropy contours of the Stator 1-Rotor 1 interface. The entropy contours of the Stator 1 outlet are somewhat similar between harmonic balance and the mixing plane methods. Both show an equal entropy distribution at the hub, but the mixing plane method span-wise distribution shows a faster reduction in wake size towards the shroud and is thinner. The large entropy feature is solely due to the blade profile entropy generation and is part of the wake that would interact with features downstream. As seen previously, the mixing plane Rotor 1 inlet is almost entirely averaged out, with a slight indication of the previous wake in the slightly larger than average entropy at the hub. The harmonic balance result shows a trident-like entropy structure as the wake is transported to the new zone. In the ideal case, the same entropy contour would be seen at the Stator 1 outlet and the Rotor 1 inlet, but the trident-like wake structure results from only a single harmonic being resolved.

5.1.1.2 Rotor 1 - Stator 2

The Rotor 1 - Stator 2 relative Mach number contours in Figure 5.3 exhibits an opposite trend as the previous where the high relative Mach number flow now occurs at the shroud position instead of the hub. This reversal occurs due to the imposed grid velocity condition on the mesh. The grid velocity imposes the rotating blade condition. As seen previously, the harmonic balance and mixing plane contours are relatively similar for the Rotor 1 outlet, with a higher flow velocity being seen when using the harmonic balance method. In the harmonic balance result, the wake is transported to the Stator 2 inlet, and the regions of high and low relative Mach number are represented. The harmonic balance representation of the Rotor 1 outlet on the Stator 2 inlet is not accurate for the span-wise flow due to the low number of harmonics resolved.

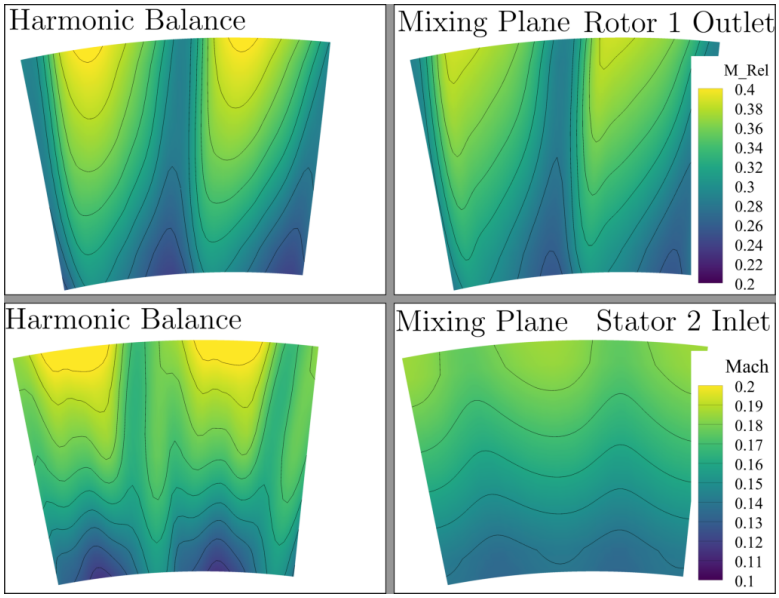

Fig. 5.3: Baseline Rotor 1-Stator 2 interface relative Mach number contour.The left column shows harmonic balance results while the right column shows the mixing plane results. The top row is the Rotor 1 outlet while the bottom row is the Stator 2 inlet.

Figure 5.4 shows the Rotor 1- Stator 2 interface's entropy contour and shows a massive difference between the harmonic balance and mixing plane methods. The harmonic balance result has a large area at the hub with high entropy, which is not present when using the mixing plane method. This area is assumed to be the wake from the previous interface, which has grown in size. As the wake has grown in size, the only source of this increase is the Stator 1 wake's interaction with the Rotor 1 blade's boundary layer. As seen previously, the wake is mimicked at the Stator 2 inlet with only the bulk entropy features of high and low regions. The wake is not very accurately represented across the interface.

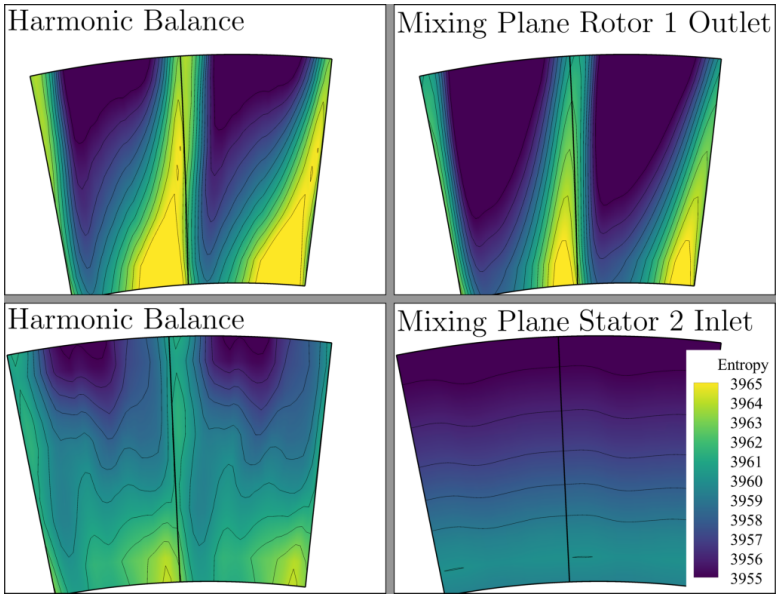

Fig. 5.4: Baseline Rotor 1-Stator 2 interface entropy contour. The left column shows harmonic balance results, while the right column shows the mixing plane results. The top row is the Rotor 1 outlet, while the bottom row is the Stator 2 inlet.

At the Rotor 1 outlet, the mixing plane wake contour for the mid-span to shroud is similar to the harmonic balance but does have a lower average value. The lower value can be explained by the absence of any wake features in the mixing plane. The mixing plane interface for the Stator 2 inlet shows a completely averaged contour but a broader region with a higher than average entropy closer to the hub.

5.1.1.3 Stator 2 outlet

The Stator 2 blade outlet Mach number contours seen in Figure 5.5 show near-identical span-wise flow distributions between the flow solvers. Mixing plane simulation shows a slightly larger flow region moving at and above $M \geq 0.65$ than the harmonic balance result at the hub.

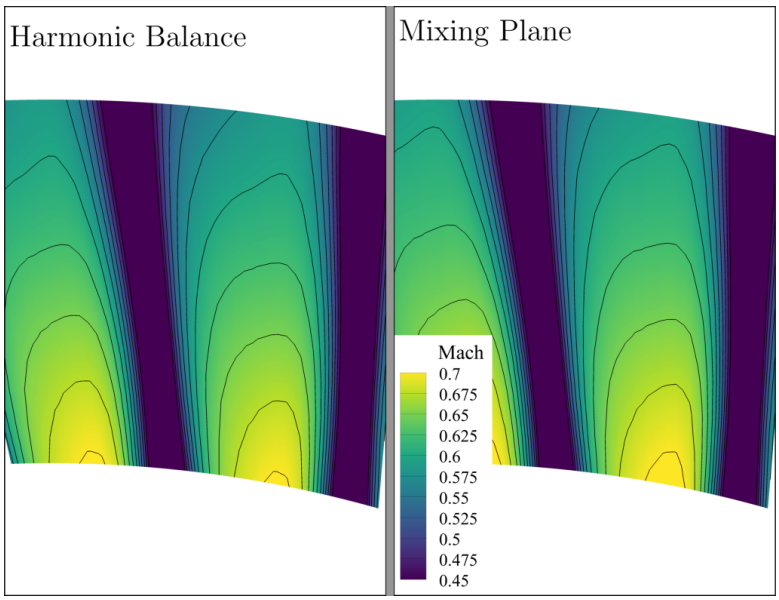

Fig. 5.5: Baseline design Stator 2 blade outlet Mach number contour. The left column shows harmonic balance results while the right column shows the mixing plane results.

A consequence of this faster moving flow is a slight increase in entropy generation both in the boundary layer and enhanced mixing in the throat area. The gradient of the contour lines becomes steeper towards the shroud in the harmonic balance case. The gradient increase leads to a rise in mixing loss, increasing average entropy in the same region than in the mixing plane result.

The entropy contours in Figure 5.6 also show similar entropy distributions, with the largest difference being the average entropy in the wake-free regions. The harmonic balance wake-free region's average entropy is higher than what is found using the mixing plane method. This entropy increase is due to the enhanced mixing seen in the Mach contour. The blade wake shows a very localized area of high entropy expected from the substantial velocity gradients found in the boundary layer.

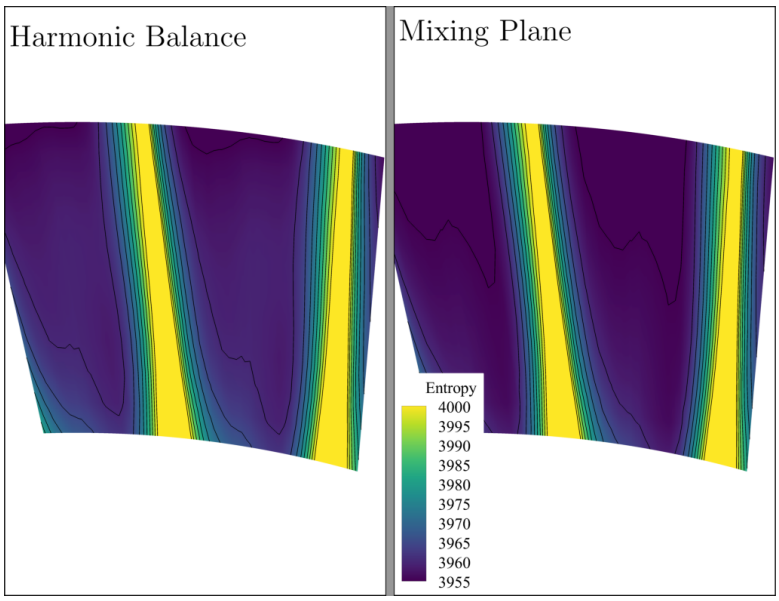

Fig. 5.6: Baseline design Stator 2 blade outlet entropy contour. The left column shows harmonic balance results while the right column shows the mixing plane results.

5.1.2 Flow field on blade to blade planes

In this section, the blade to blade flow Mach number contours are shown at the hub, mid-span, and shroud positions. Another iso-surface view indicates the region of flow above a threshold to show the flow interactions at the blade's throat.

5.1.2.1 Stator 1

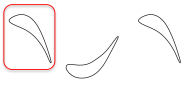

In Figure 5.7 (**a**) the Mach contours are shown for the hub, mid-span, and shroud position while in (**b**) a Mach number iso-surface for flow above 0.5 is shown for the Stator 1 blade in both harmonic balance on the left and mixing plane method on the right.

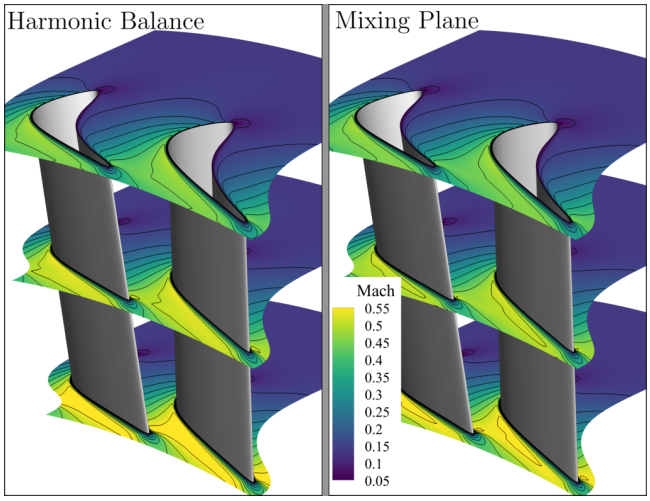

(**a**) Mach number contour at hub, mid-span, and shroud position.

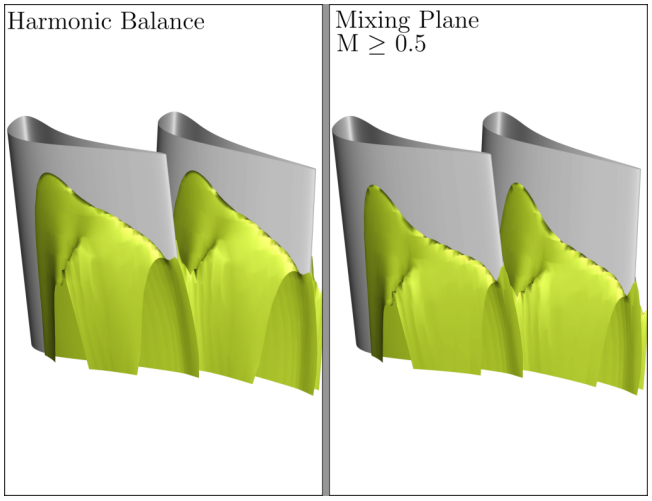

(**b**) $M \geq 0.5$ iso-surface.

Fig. 5.7: Harmonic balance and Mixing Plane (**a**) Mach contour and (**b**) $M \geq 0.5$ iso-surface for the baseline Stator 1 blade. In both (**a**) and (**b**) the left picture shows harmonic balance result while the right result shows the mixing plane. The top of the blade is the location of the shroud.

In (**a**) the shroud does not have much difference, but the mid-span and especially hub show a very large difference in the contours' highest flow velocity. The harmonic balance contours show the entire geometric throat to have a Mach number larger than 0.55, while the mixing plane contour only has a small area of the same flow velocity. The difference would suggest that the harmonic balance result generates more entropy in this area than the mixing plane due to increased mixing and boundary layer losses. Figure 5.7 (**b**) also shows that a greater percentage of the blade span accelerates above a Mach number of 0.5 in harmonic balance simulation than in mixing plane. The increase of fast flow suggests an increase in entropy generation.

5.1.2.2 Rotor 1

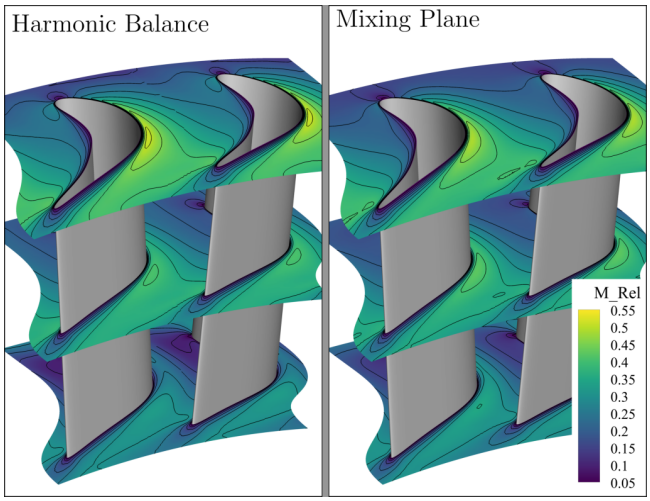

(**a**) Relative Mach number contour at hub, mid-span, and shroud position.

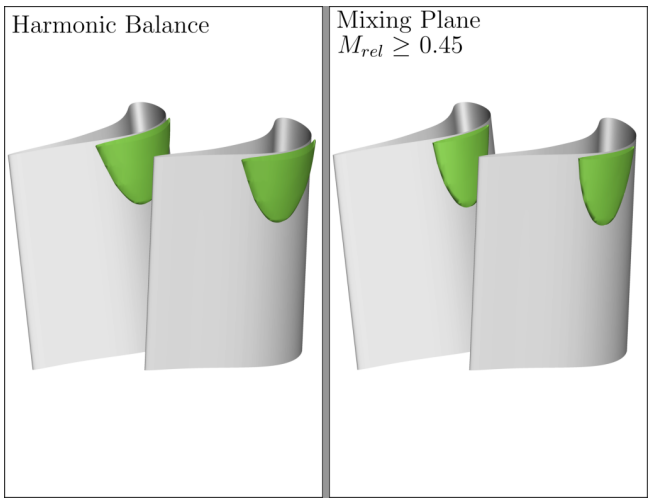

(**b**) $M_{\text{rel}} \geq 0.45$ iso-surface.

Fig. 5.8: Harmonic balance and Mixing Plane M_{rel} contour (**a**) and $M_{\text{rel}} \geq 0.45$ (**b**) for the baseline Rotor 1 Geometry. In both (**a**) and (**b**) the left picture shows harmonic balance result while the right result shows the mixing plane. The top of the blade is the location of the shroud.

In Figure 5.8 (**a**) the relative Mach contours are shown for the hub, mid-span, and shroud position while in (**b**) a Mach iso-surface for flow above 0.45 is shown for the Rotor 1 blade with harmonic balance on the left and mixing plane method on the right. In the Rotor 1 flow field, the relative Mach contours are very similar between harmonic balance and mixing plane. The shroud contour in Figure 5.8 (**a**) shows that there is a slightly higher Mach number which occurs further away from the geometric throat as compared to the mixing plane case. In Figure 5.8 (**b**) the contours for flow about $M_{\text{rel}} \geq 0.45$ is quite similar but the harmonic balance method iso-surface is slightly larger in the axial direction and thinner in the blade to blade plane. Due to the nearly equal size of the iso-surface, this region's entropy differences should not result from flow mixing.

5.1.2.3 Stator 2

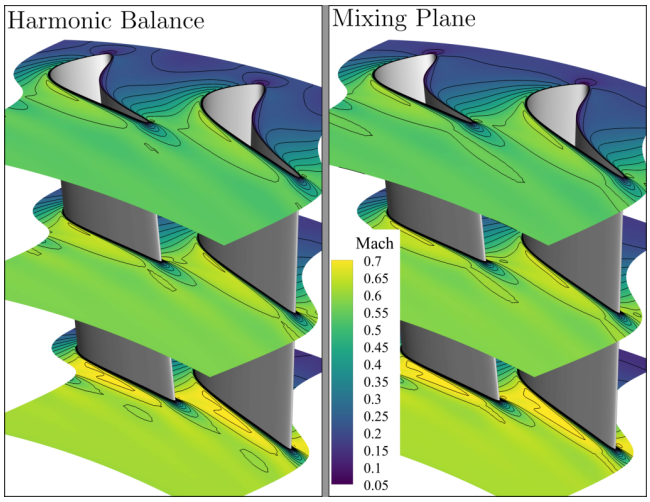

(**a**) Mach number contour at hub, mid-span, and shroud position.

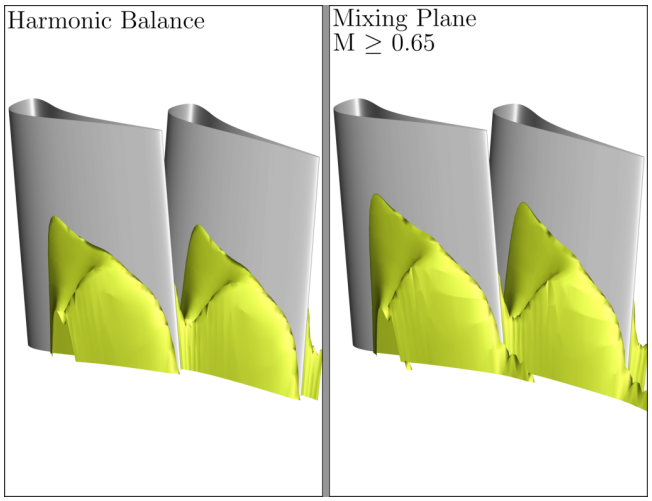

(**b**) $M \geq 0.65$ iso-surface.

Fig. 5.9: Harmonic balance and Mixing Plane Mach contour (**a**) and $M \geq 0.65$ (**b**) for the baseline Stator 2 Geometry. In both (**a**) and (**b**) the left picture shows harmonic balance result while the right result shows the mixing plane. The top of the blade is the location of the shroud.

In Figure 5.9 (**a**) the Mach contours are shown for the hub, mid-span, and shroud position while in (**b**) a Mach contour for flow above 0.65 is shown for the Stator 2 blade with the harmonic balance method used on the left and mixing plane method on the right. Figure 5.9 (**a**) shows that the shroud section has similar flow behavior up until the Stator 2 throat. The wake is more pronounced in the mixing plane method denoted by the extension of the iso-surface past the blade trailing edge in Figure 5.9 (**b**) . The hub section shows that the mixing plane method produces an overall larger area of high Mach number flow. In Figure 5.9 (**b**) a large distinction can be seen in how the throat area affects the flow velocity. The hub shows a near unbroken flow velocity with a Mach number greater than 0.7. The span-wise position where the throat accelerates to flow to Mach 0.7 is similar in both harmonic balance and mixing plane. However, the harmonic balance method iso-surface shows that the flow does not accelerate as much moving towards the shroud, which would suggest a reduced rate of entropy generation in this area.

5.1.3 Mass-Averaged Entropy trends in Axial direction

Mass-flow averaged entropy is plotted as a function of axial distance for both harmonic balance and mixing plane in Figure 5.10 (**a**) with the difference between mixing plane and the harmonic balance shown in Figure 5.10 (**b**). Figure 5.10 (**a**) best shows how large the differences are between harmonic balance and mixing plane methods. Entropy generation resulting from the boundary layer is very similar for Stator 1, and the entropy at the trailing edge is quite small. A large divergence in entropy occurs in the Rotor 1 zone, which is expected as this zone is where most time-varying interactions are assumed to occur. In Figure 5.10 (**b**), the Rotor 1 zone, including the interface differences, accounts for the supermajority of the total entropy difference between the two methods.

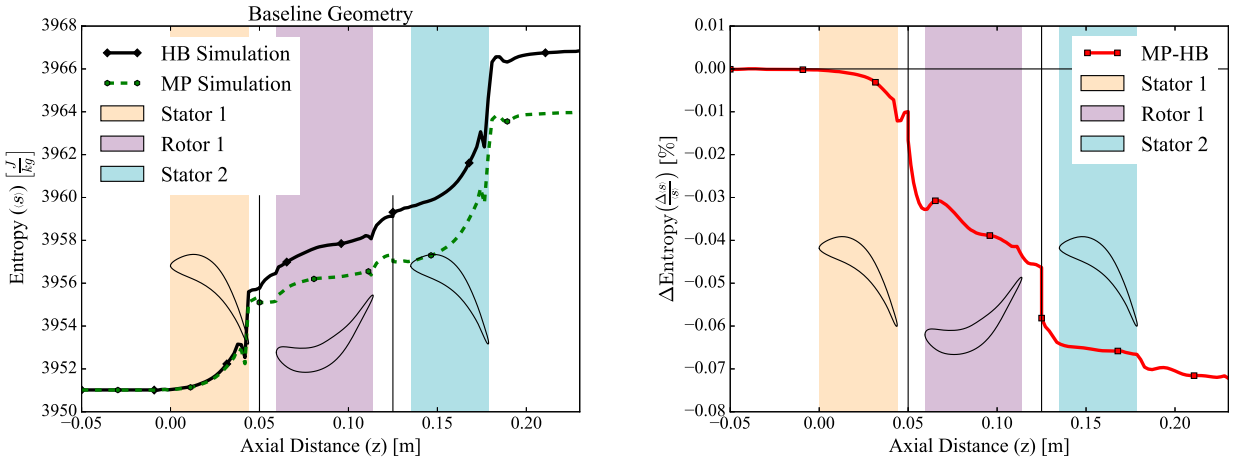

(**a**). (**b**).

Fig. 5.10: Harmonic balance to mixing plane baseline geometry (**a**) mass-flow averaged entropy trend and (**b**) mass-flow averaged entropy difference.

Stator 2 shows a slight increase in the difference between harmonic balance and mixing plane results but accounts for a small portion. While the entropy difference is large, the rate of the respective trends changing is almost identical and can be seen by the nearly flat line in Figure 5.10 (**b**).

Both Stator 1 and Stator 2 account for a small portion of the difference between mixing plane and harmonic balance results and are inherently stationary zones. The Rotor 1 zone shows the largest divergence differences in entropy and is inherently unsteady. The Stator 1 blade wake increasing entropy generation of subsequent components can not be definitively shown as the wake passed on at the Rotor 1-Stator 2 interface is more diffused and not as well defined as the Stator 1-Rotor 1 interface. The Stator 2 blade outlet shows a minimal difference for entropy in the wake between the two methods. However, harmonic balance results show larger entropy values in the wake-free region than mixing plane.

Further investigation is needed to answer if, in multizone harmonic balance simulation, the minimum number of time instances required is dependent on zone number to accurately maintain wake structure coherence as the entropy in the wake-free area rises. In Figure 5.2 the Stator 1-Rotor 1 interface shows is a clear entropy flow structure, which is assumed to represent the wake due to the high entropy. An equivalent structure can not be seen at the Rotor 1-Stator 2 interface in Figure 5.4. This interface only has two small regions of high or low entropy with a more or less uniformly averaged middle area. A clear and identifiable wake structure is not seen and suggests that the wake is no longer localized.

5.2 HB and MP Based design sensitivities

The design sensitivities calculated with the two flow solution methods at design step 0 were compared to gain insight on whether the optimization could converge to the same optimal solution. As the harmonic balance method is a series of steady simulations solved at different time steps, surface sensitivities are available every instant. These time instants are averaged together for the comparison against the mixing plane sensitivities using:

$$\frac{dJ}{d\mathbf{X}}_{surf,HB} = \frac{1}{3}\sum_{n=0}^{2}\sqrt{\left(\frac{dJ}{d\mathbf{X}_{\text{surf,x,n}}}\right)^2 + \left(\frac{dJ}{d\mathbf{X}_{\text{surf,y,n}}}\right)^2 + \left(\frac{dJ}{d\mathbf{X}_{\text{surf,z,n}}}\right)^2}. \tag{5.1}$$

After a qualitative inspection of surface blade surface sensitivity, a histogram is made that sorts mesh point surface sensitivities into 100 discrete bins from -0.01 to 0.01 and the number of points in each bin on a logarithmic axis for both harmonic balance (HB) and mixing plane (MP) sensitivities. This representation is chosen over showing the full design vector sensitivity $\left(\frac{dJ}{d\alpha}\right)$ as an agreement between the sensitivities is not expected. Blade surface sensitivity value is independent of the parameterization type and would not change if an FFD box was used, or a different NURBS parameterization was chosen. A positive sensitivity value would deform the

blade normal to the surface (increasing thickness), while a negative value would depress the blade (decreasing thickness).

5.2.1 Stator 1

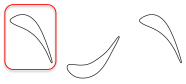

In Figure 5.11 the pressure side of the Stator 1 blade surface sensitivity is compared between the harmonic balance and mixing plane methods.

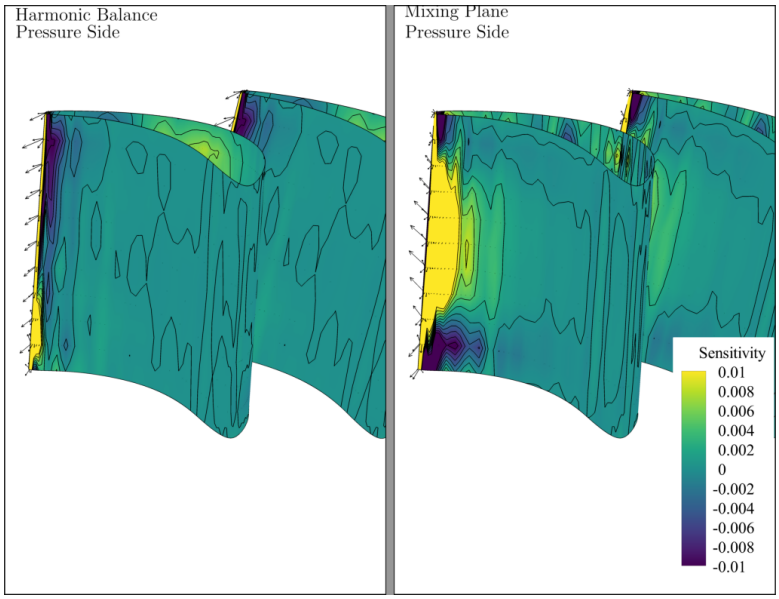

Fig. 5.11: Stator 1 Pressure side objective surface sensitivity. The left picture shows the harmonic balance result, while the right result shows the mixing plane. The top of the blade is the location of the shroud.

The mixing plane surface is quite sensitive at the trailing edge, especially around the mid-span region. This sensitivity is positive and would create a thicker edge. Due to the choice of the design parameters, this region is not eligible for deformation and thus does not impact the optimization process too much. Interestingly, until the blade's geometrical throat, the two methods have very similar sensitivity contours but are predominantly around zero, indicating relatively insensitive blade surface areas. Insensitive blade surfaces are not likely to be deformed and are verifiable in the final geometries present in subsequent sections. A cause of this insensitivity is because the pressure side of a turbine blade is not responsible for much entropy generation [14]. The boundary layer is predominantly responsible for entropy generation on a surface. On the pressure side of a blade, the boundary layer is very thin and remains attached, keeping entropy generation low.

The suction side of Stator 1 shows a large difference between harmonic balance and mixing plane results, as seen in Figure 5.12. Before the geometric throat, similar behavior of being relatively insensitive to design changes is shown but abruptly changes in the mixing plane case. This sensitivity difference is caused by the flow passing the blades' geometric throat and flow now mixing into an open area. The mixing plane method is highly sensitive at the trailing edge, which is not present in the harmonic balance method.

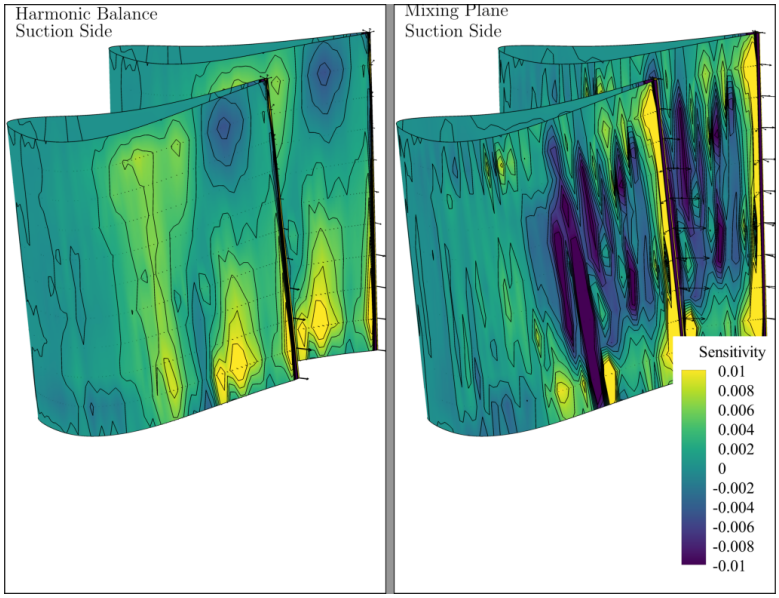

Fig. 5.12: Stator 1 Suction side objective surface sensitivity. The left picture shows harmonic balance result while the right result shows the mixing plane. The top of the blade is the location of the shroud.

A potential cause of this difference is that the flow is partially separated at the edge in the mixing plane case. When the sensitivity is calculated, a separation bubble forms, impacting the trailing edge's boundary layer. The changing boundary layer is the largest contributor to entropy generation in the Stator 1 blade seen in Figure 5.10 (**a**).

Figure 5.13 shows a histogram of the surface sensitivity points on the Stator 1 blade on a logarithmic scale with the harmonic balance in blue and mixing plane in green. Both methods have a majority and a similar amount of points with near 0 sensitivity (insensitive).

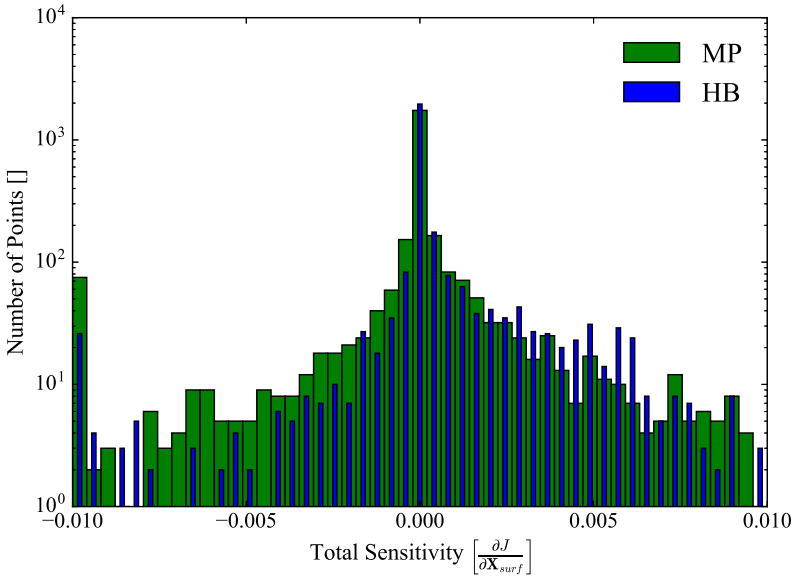

Fig. 5.13: Stator 1 Surface sensitivity histogram.

The harmonic balance distribution shows that most of the Stator 1 surface points have a positive total sensitivity creating a thicker blade. The mixing plane shows a more even distribution of points with positive and negative sensitivities. The mixing plane optimization is expected to result in a thinner blade than the harmonic balance optimized result from this distribution.

5.2.2 Rotor 1

In Figure 5.14 the pressure side surface sensitivity of the Rotor 1 blade is shown. The mixing plane case again shows a high sensitivity at the trailing edge, which is not present in harmonic balance with a predominantly 0 surface sensitivity along the rest of the blade.

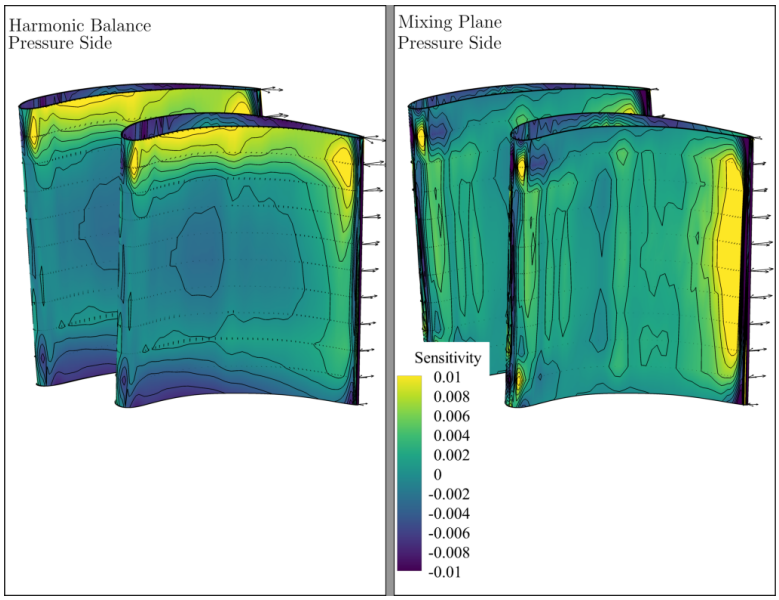

Fig. 5.14: Rotor 1 Pressure side objective surface sensitivity. The left picture shows harmonic balance result while the right result shows the mixing plane. The top of the blade is the location of the shroud.

Harmonic balance shows a span-wise difference in sensitivity along with a greater sensitivity until the geometric throat. The shroud shows a positive sensitivity in the axial direction, while the hub is the opposite. These sensitivities indicate that the harmonic balance method will deform the hub and shroud pressure surface before the geometric throat.

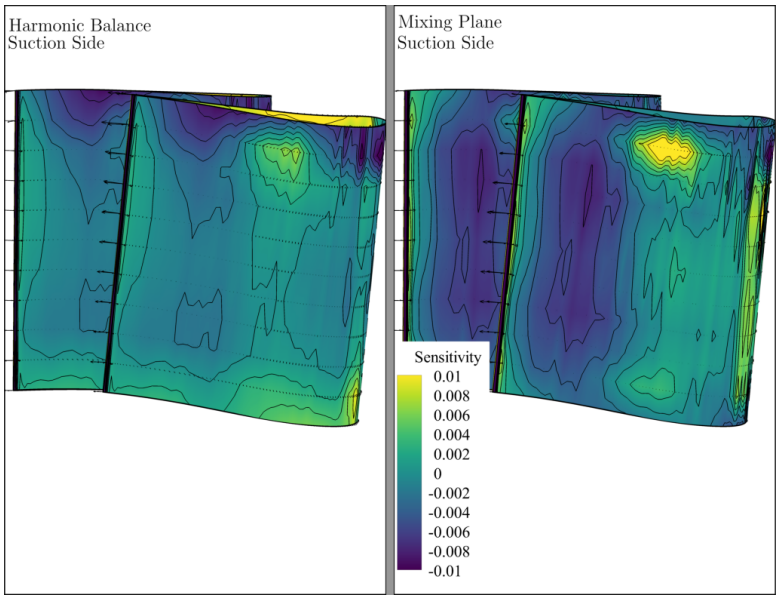

Fig. 5.15: Rotor 1 Suction side objective surface sensitivity. The left picture shows harmonic balance result while the right result shows the mixing plane. The top of the blade is the location of the shroud.

Figure 5.15 shows the suction surface of the Rotor 1 blade. The mixing plane sensitivity shows similar behavior to the Stator 1 suction side. There is an abrupt change in sensitivity past the geometric throat with a predominately negative sensitivity. The region of negative sensitivity is also much larger in the span-wise direction in the mixing plane case than the harmonic balance. The harmonic balance sensitivity area is mainly confined to the shroud section and quickly returns to a near-zero sensitivity.

Figure 5.16 shows a histogram of the surface sensitivity points on the Rotor 1 blade on a logarithmic scale with the harmonic balance in blue and mixing plane in green. Both methods have a majority and a similar amount of points with near 0 sensitivity (insensitive). A similar distribution can be seen for both mixing plane and harmonic balance results. Harmonic balance shows a slightly larger number of points with negative sensitivity and would be expected to have a thinner profile.

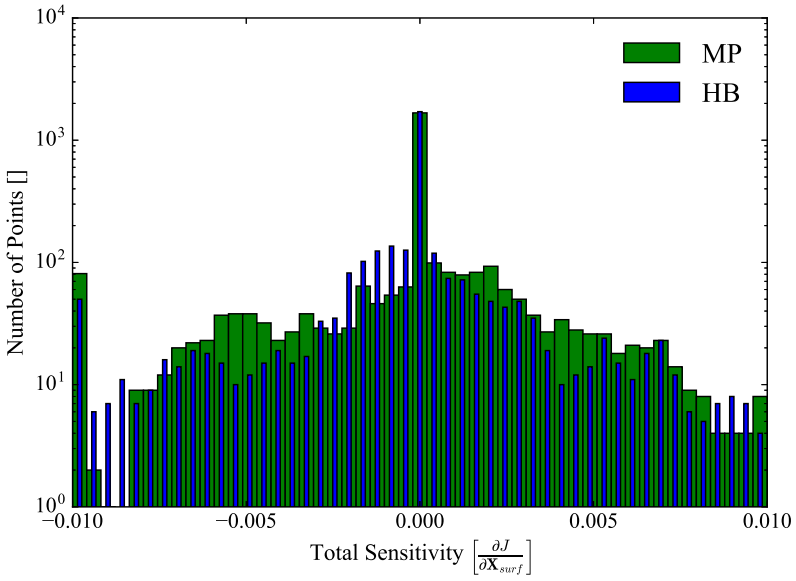

Fig. 5.16: Rotor 1 Surface sensitivity histogram.

5.2.3 Stator 2

Figure 5.17 shows agreement between harmonic balance and mixing plane method trailing edge sensitivity, but the mixing plane method resolves a larger area of positive sensitivity that is absent in harmonic balance.

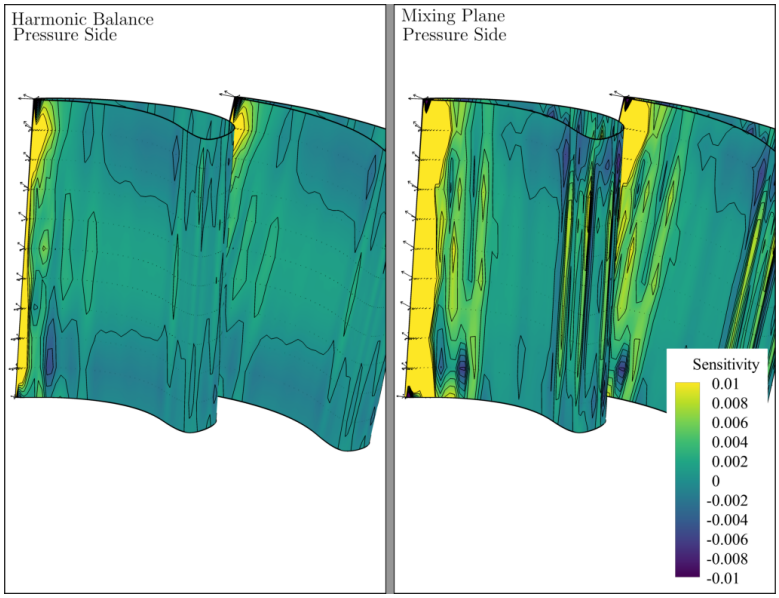

Fig. 5.17: Stator 2 Pressure side objective surface sensitivity. The left picture shows the harmonic balance result, while the right result shows the mixing plane. The top of the blade is the location of the shroud.

The geometric throat again shows up as a divergence point in sensitivity behavior, which becomes much more variable in the mixing plane case. Leading-edge sensitivity is also quite different with a greater variation in the mixing plane case.

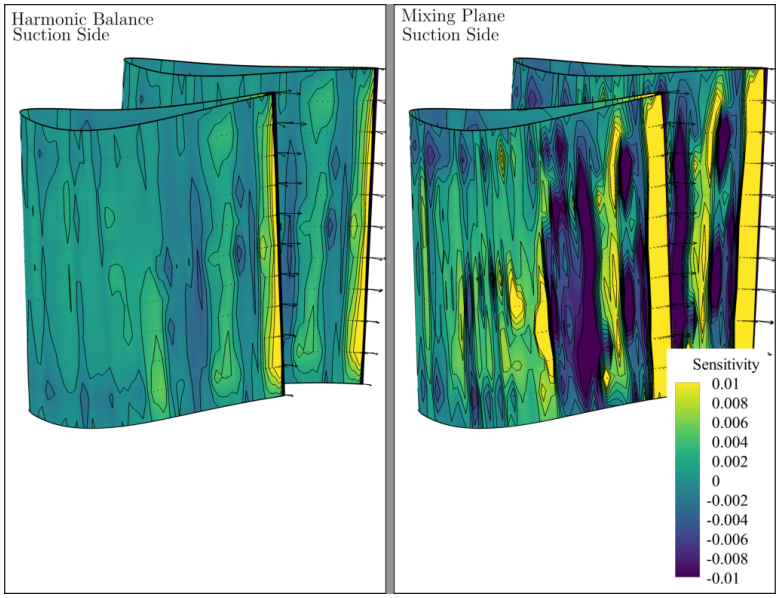

Fig. 5.18: Stator 2 Suction side objective surface sensitivity. The left picture shows harmonic balance result while the right result shows the mixing plane. The top of the blade is the location of the shroud.

The suction surface in Figure 5.18 shows the importance of the geometric throat on the sensitivity in the case of the mixing plane method again. A very distinct variability increase in sensitivity can be seen as a side effect of the throat, but the trailing edge sensitivity is similar to the harmonic balance result. The mixing plane method's high sensitivity area encompasses a larger trailing edge area and spans the blade's entirety.

Figure 5.19 shows a histogram of the surface sensitivity points on the Stator 2 blade on a logarithmic scale with the harmonic balance in blue and mixing plane in green.

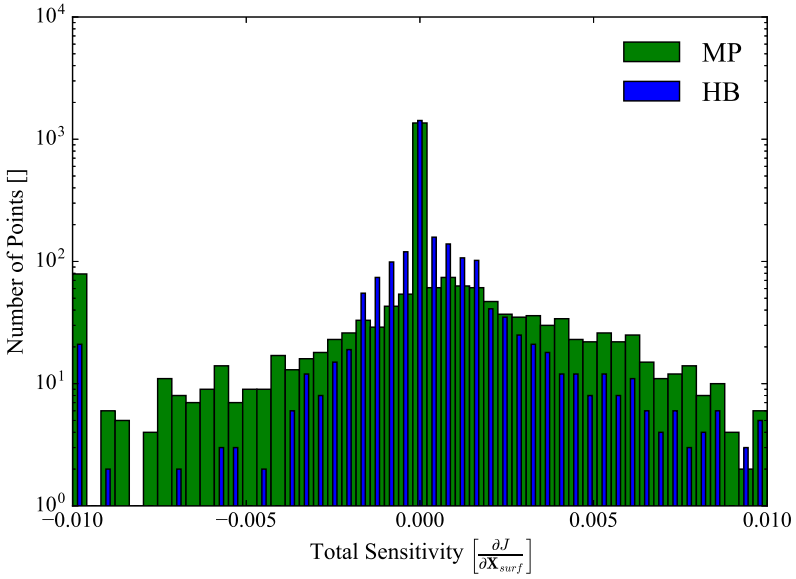

Fig. 5.19: Stator 2 Surface sensitivity histogram.

Both methods have a majority and a similar amount of points with near 0 sensitivity (insensitive). Like Stator 1, there is a greater distribution of points with positive sensitivity than negative for both harmonic balance and mixing plane. The harmonic balance distribution also shows a tighter clustering around 0 with a consistently lower amount of points for a given sensitivity than the mixing plane. The harmonic balance optimized blade is expected to show an increase in blade thickness, while the mixing plane blade thickness change can not be estimated.

5.2.4 Final Remarks

A few conclusions can be made by reviewing the sensitivity histograms for blade surface sensitivities of harmonic balance and mixing plane methods.

- The Stator 1 surface sensitivity in the mixing plane has more mesh points with a negative sensitivity than the harmonic balance method indicating the mixing plane optimized blade would show a decreased blade thickness relative to the harmonic balance case.
- The Rotor 1 surface sensitivity in the mixing plane and harmonic balance case are more uniformly spread in sensitivity than either the Stator 1 or Stator 2 blades. The harmonic balance surface sensitivity is skewed towards the negative values and indicates a greater propensity for blade thickness reduction.
- The Stator 2 surface sensitivity in the harmonic balance case is much more centered around 0, with a majority of mesh points having a positive sensitivity. The mixing plane method shows a much greater variety of surface sensitivities and is inconclusive to blade thickness changes.
- In all blades, the mixing plane method surface sensitivities show a wide spatial variation in surface sensitivity past the blade's geometric throat. This variability is hypothesized to result from potential boundary layer separation. Harmonic balance results do not show nearly as much variation past the geometric throat.

5.3 Optimization Performance

Optimization was performed using both harmonic balance and mixing plane methods starting from the baseline design. The optimization was continued until either negative mesh volumes were created or flow convergence no longer reached six orders of magnitude. No re-meshing steps were done as the grid is highly sensitive to changes.

The convergence history of the harmonic balance and mixing plane optimizations are shown in Figure 5.20. (**a**) shows the entropy generation and power for both the harmonic balance and mixing plane simulations while Figure 5.20 (**b**) shows the non-dimensional change with respect to the initial value of the baseline mesh.

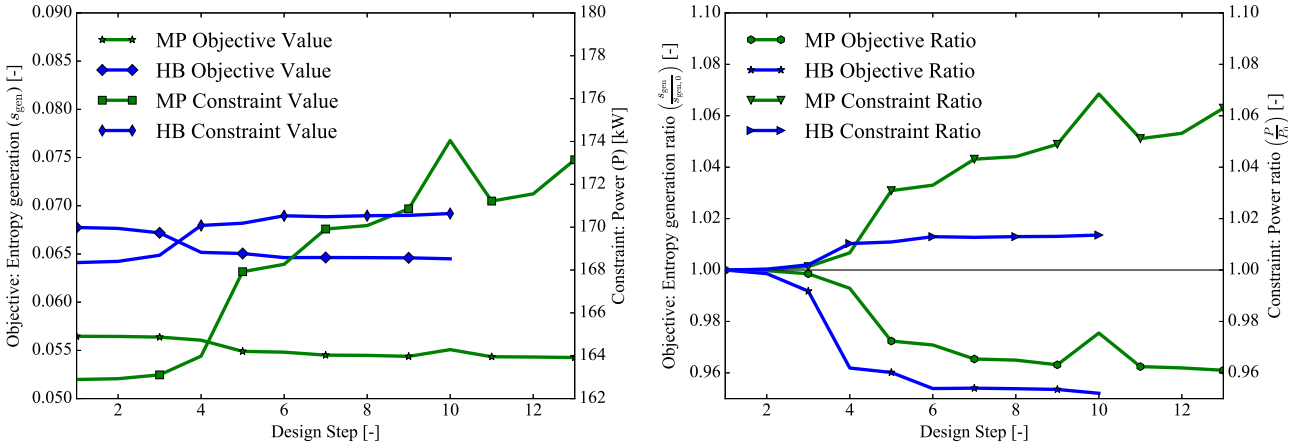

(**a**) Optimization values.

(**b**) Non-dimensional optimization values.

Fig. 5.20: Optimization convergence history of (**a**) entropy generation and power and (**b**) non-dimensional entropy generation ratio and power ratio.

The harmonic balance (HB) optimized design resulted in a 4.87% reduction in entropy generation, while the mixing plane (MP) optimized design has a 3.89% reduction. Note that in both cases, the optimization is a non-dominated constrained problem. In non-dominated constrained problems, the constraint is not active and could be omitted without impacting the optimization results.

5.4 HB-based Optimization Results

5.4.1 Blade Shapes

The harmonic balance optimized design can be seen in Figure 5.21 with the baseline blade geometry as a black line and the optimized blade geometry in blue. The hub, mid-span, and shroud sections are denoted with solid, dash-dotted, and dashed lines.

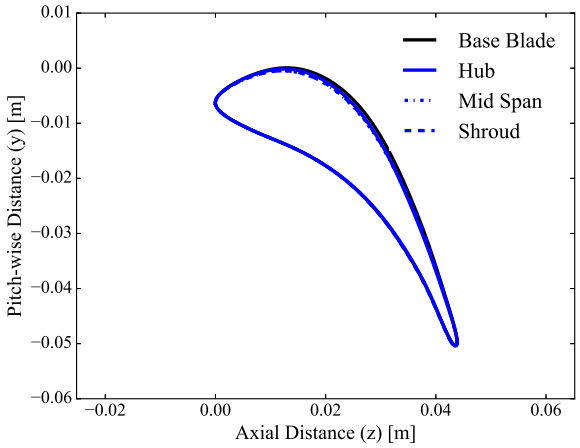

(**a**) Stator 1.

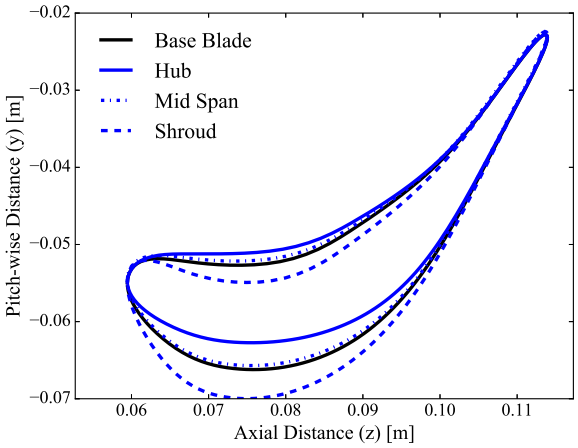

(**b**) Rotor 1.

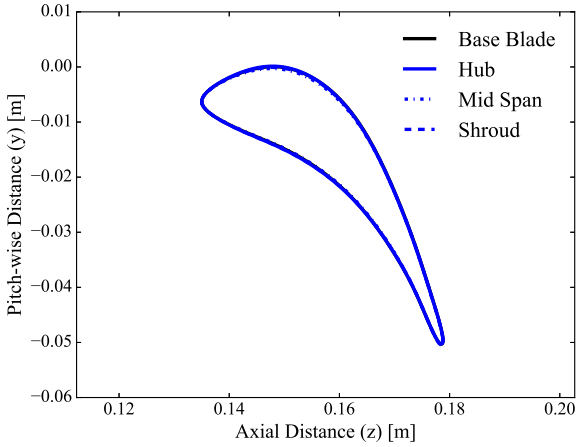

(**c**) Stator 2.

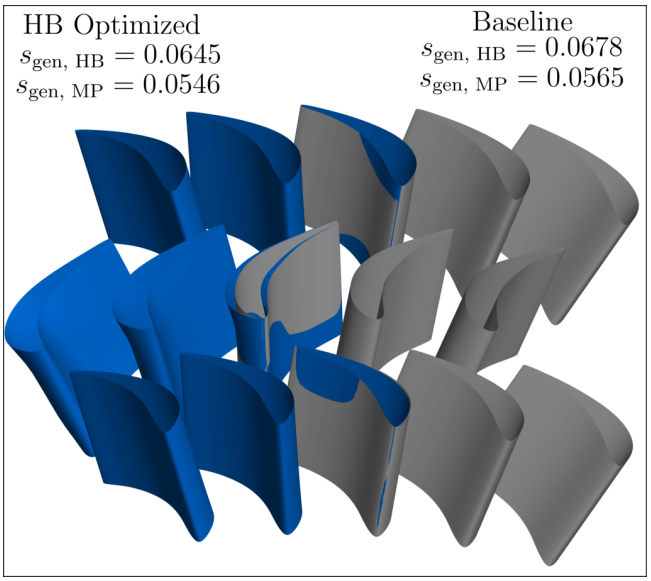

(**d**) Harmonic Balance Optimized Blade Shapes.

Fig. 5.21: Harmonic Balance Optimized Blade shapes (**a**) Stator 1, (**b**) Rotor 1, (**c**) Stator 2, (**d**) Harmonic balance optimized blade comparison to baseline geometry.

Both Stator 1 and Stator 2 have minimal deformation, while Rotor 1 has the bulk of the changes. Rotor 1 shows interesting design changes at the hub and shroud sections. The hub shows a reduction in the blade thickness for most of the blade with a flattening of the suction side curvature. These changes increase the circumferential space and decrease the hub's flow velocity due to a larger flow area. The shroud exhibits an increase in blade thickness and curvature on both the pressure and suction sides. This design change's overall effect should be to increase the rotor shroud's flow velocity due to an area decrease in the blade to blade plane. The increased curvature is also responsible for the increased power output of the turbine.

5.4.2 Flow field on secondary planes

All flow contours and values are from a harmonic balance method simulation and averaged across all resolved time instances.

5.4.2.1 Stator 1 - Rotor 1

In Figure 5.22 the relative Mach number contour for the baseline and optimized blades interface between Stator 1 and Rotor 1 are shown. The Stator 1 outlet shows a reduction in the maximum velocity on the hub section of the blade. The span-wise flow distribution is relatively unchanged, but the wake flow shows a difference in velocity. Flow velocity at the shroud wake is lower in the optimized case and remains lower at the hub as well. The Rotor 1 inlet shows the general trend of high and low-velocity flow but does not accurately reproduce the Stator 1 outlet flow contour.

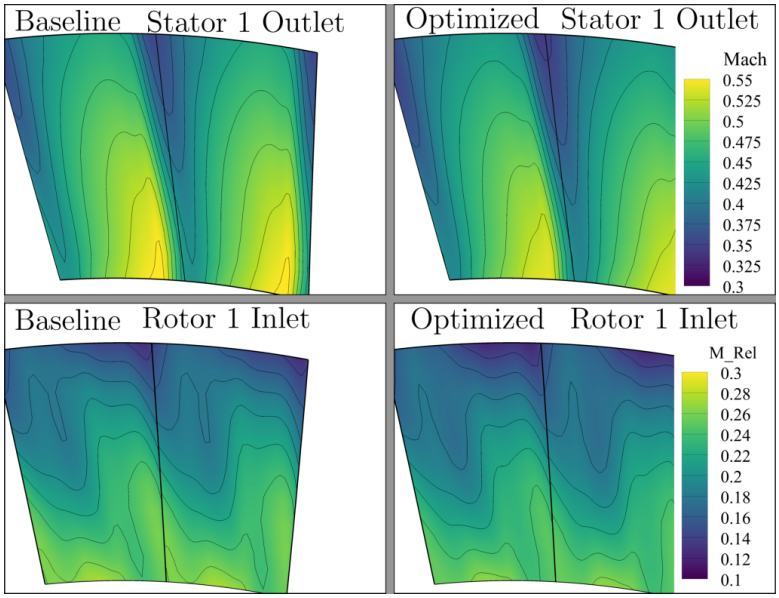

Fig. 5.22: Harmonic balance optimized Stator 1 to Rotor 1 interface Mach and Relative Mach number contour. The left column shows baseline flow field while the right column shows the optimized flow field.

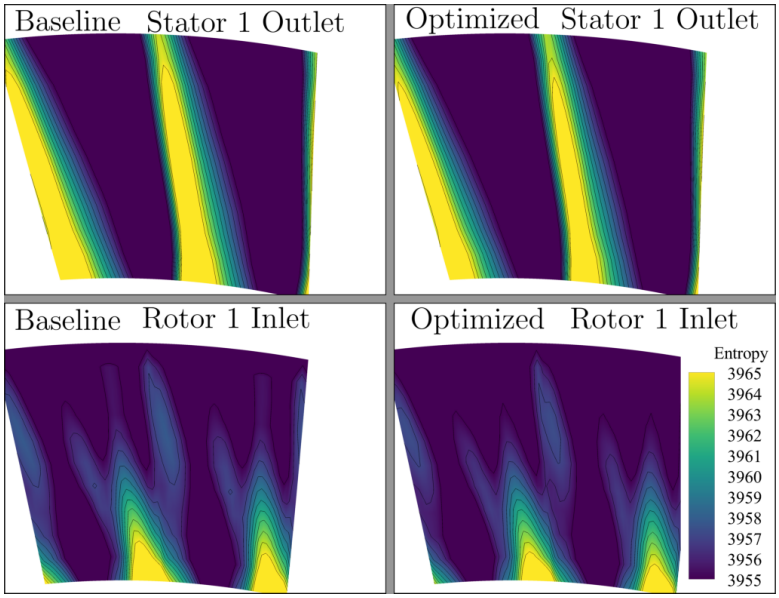

Fig. 5.23: Harmonic balance optimized Stator 1 to Rotor 1 interface entropy contour. The left column shows baseline flow field while the right column shows the optimized flow field.

Figure 5.23 shows a reduction in wake thickness in the optimized Stator 1 outlet compared to the baseline. The wake structure transported to the Rotor 1 inlet reflects the reduction of losses in the wake. This result

is interesting as the Stator 1 blade shape in Figure 5.21 (**a**) is nearly identical to the baseline shape, yet the Stator 1 wake has been distinctly modified. Further exploration is given in section 5.6.

5.4.2.2 Rotor 1 - Stator 2

Figure 5.24 Shows the Rotor 1-Stator 2 relative Mach number contours for the baseline and harmonic balance optimized blade shapes. The optimized geometry shows a slight increase of relative Mach number at the shroud. The Stator 2 inlet shows a reduction in overall flow velocity, and a majority of the flow is moving at a speed less than Mach 0.2.

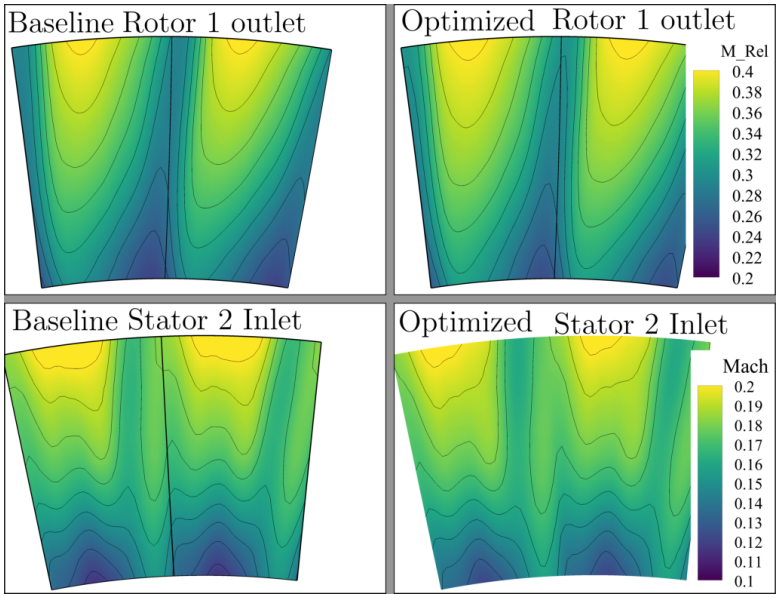

Fig. 5.24: Harmonic balance optimized Rotor 1 to Stator 2 interface Relative Mach and Mach number contour. The left column shows baseline flow field while the right column shows the optimized flow field.

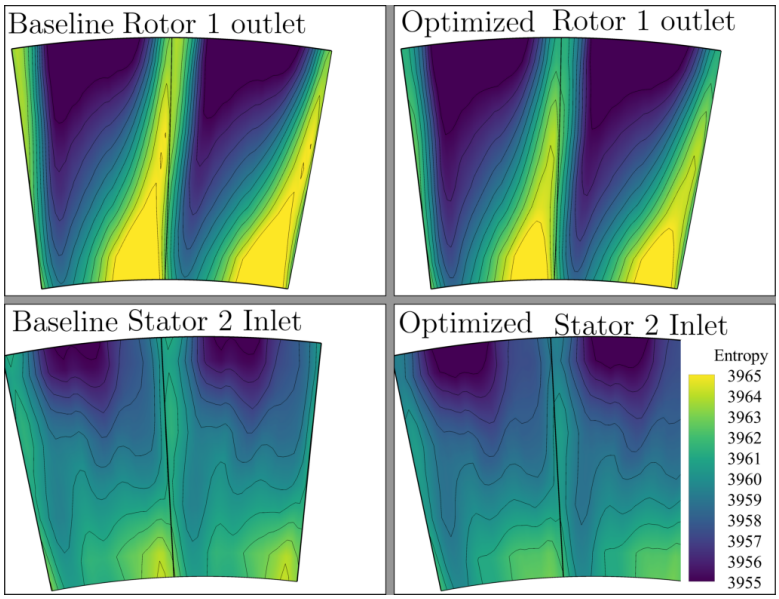

Fig. 5.25: Harmonic balance optimized Rotor 1 to Stator 2 interface entropy contour. The left column shows baseline flow field while the right column shows the optimized flow field.

5.4.2.3 Stator 2 outlet

The Rotor 1 entropy wake seen in Figure 5.25 at the Rotor 1 outlet shows an apparent reduction between the baseline and optimized geometries. The hub wake bulge is significantly reduced and shows less influence on the blade's upper span-wise portions. As seen in the baseline comparison of Figure 5.4, the wake structure is again almost completely gone at the inlet interface. The only wake structure indicated is the wake free shroud's low entropy area and the hub's high entropy area.

The Stator 2 blade outlet mach number between the baseline and optimized blade geometries in Figure 5.26 is very similar. The largest difference is at the hub with a slightly increased mach number but it quickly returns to the baseline span-wise flow distribution.

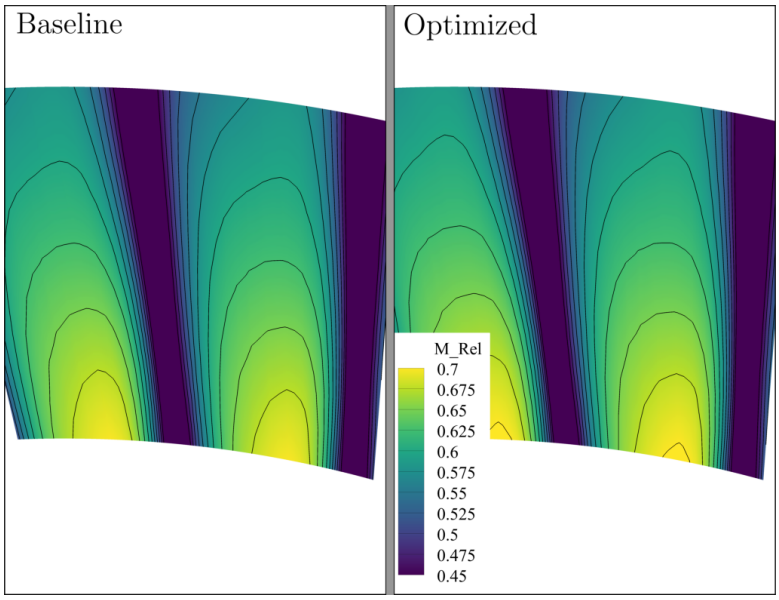

Fig. 5.26: Harmonic balance optimized Stator 2 outlet Mach number contour. The left column shows baseline flow field while the right column shows the optimized flow field.

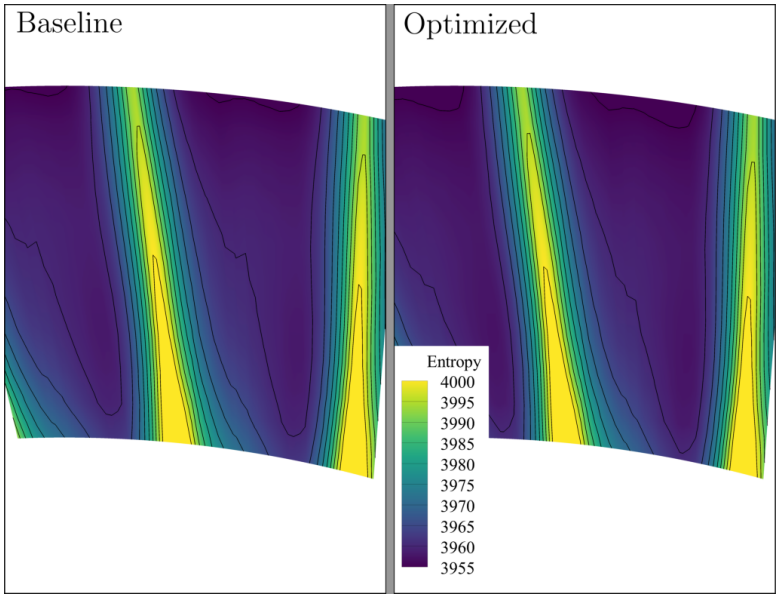

Fig. 5.27: Harmonic balance optimized Stator 2 outlet entropy contour. The left column shows baseline flow field while the right column shows the optimized flow field.

The entropy contours of Figure 5.27 are nearly identical between baseline and optimized designs. From the contours, the only difference of note is that the optimized blade geometry has lower entropy in the wake-free region. Since the boundary layer is the primary source of entropy generation, the overall entropy generation due to the Stator 2 blade should be nearly identical between the baseline and optimized geometries.

5.4.3 Flow field on blade to blade planes

5.4.3.1 Stator 1

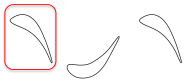

In Figure 5.28 (**a**) , the relative Mach contours are shown for the hub, mid-span, and shroud position. In contrast, in (**b**), a Mach number iso-surface for flow above 0.5 is shown for the Stator 1 blade with baseline geometry on the left and optimized geometry on the right.

In Figure 5.28 (**a**) , the span-wise slices show that flow in the blade to blade plane is similar between the baseline and optimized geometries. The most noticeable difference can be seen in the hub slice, where there is a bubble of higher velocity flow.

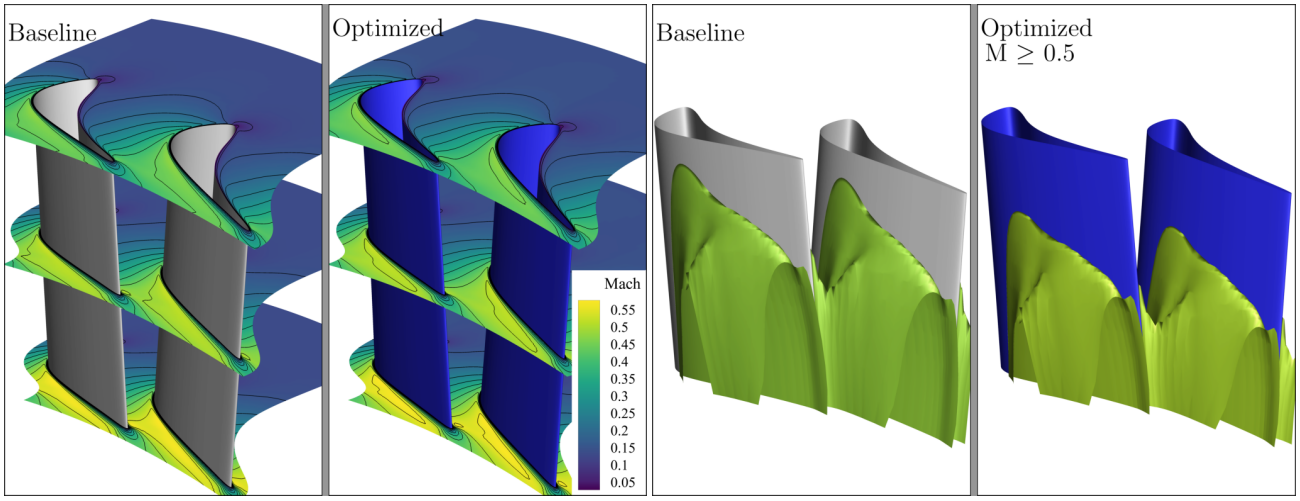

(**a**) Stator 1 hub, mid-span, and shroud contours.

(**b**) $M \geq 0.5$ iso-surface.

Fig. 5.28: Stator 1 Harmonic Balance optimized Stator 1 Mach number contours. In both (**a**) and (**b**) the left column shows baseline flow field while the right column shows the optimized flow field. The top of the blade is the location of the shroud surface.

The reduction in the wake size seen in the interface between Stator 1 and Rotor 1 comes as a side effect of reduction in flow velocity in the geometric throat of Stator 1. In Figure 5.28 (**b**), the span-wise location where the flow exceeds 0.55 has been reduced and occurs closer to the center of the blade span. As the Stator 1 blade is nearly absent of deformation, the flow velocity change stems from the Rotor 1 blade shape's upstream influence. The upstream influence of the Rotor 1 blade shape changes reduced the flow velocity in the Stator 1 position. The large reduction in high-velocity flow at the geometric throat is responsible for a large decrease in entropy in this region.

5.4.3.2 Rotor 1

In Figure 5.29 (**a**) the relative Mach contours are shown for the hub, mid-span and shroud position while in (**b**) a Mach number iso-surface for flow above 0.45 is shown for the Rotor 1 blade with the baseline design on the left and optimized design on the right.

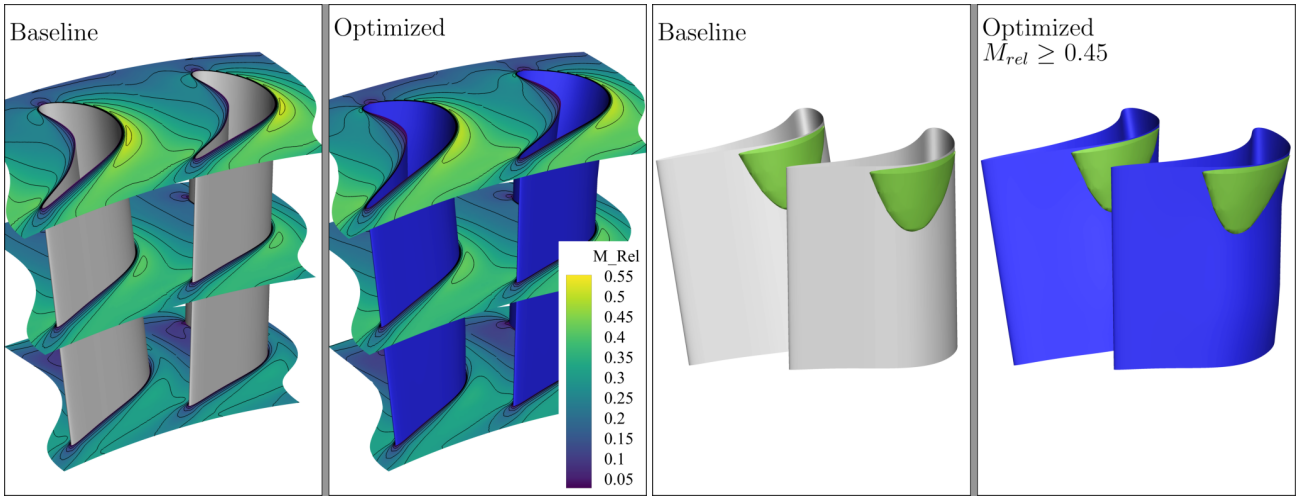

(**a**) hub, mid-span, and shroud contours. (**b**) $M_{\text{rel}} \geq 0.45$ iso-surface.

Fig. 5.29: Rotor 1 Harmonic Balance optimized Stator 1 Relative Mach number contours. In both (**a**) and (**b**) the left column shows baseline flow field while the right column shows the optimized flow field. The top of the blade is the location of the shroud surface.

The Rotor 1 relative Mach number flow field is similar to the baseline comparison between the baseline design and the optimized design. There are minimal differences in Figure 5.29 (**a**) of the Mach contours. Hence, the difference is seen at the Rotor 1 - Stator 2 interface is predominantly due to the wake interacting with the boundary layer and not due to the mixing of high-velocity flow.

5.4.3.3 Stator 2

In Figure 5.30 (**a**) the Mach contours are shown for the hub, mid-span and shroud position while in (**b**) a Mach number iso-surface for flow above 0.65 is shown for the Stator 2 blade for the baseline and optimized designs.

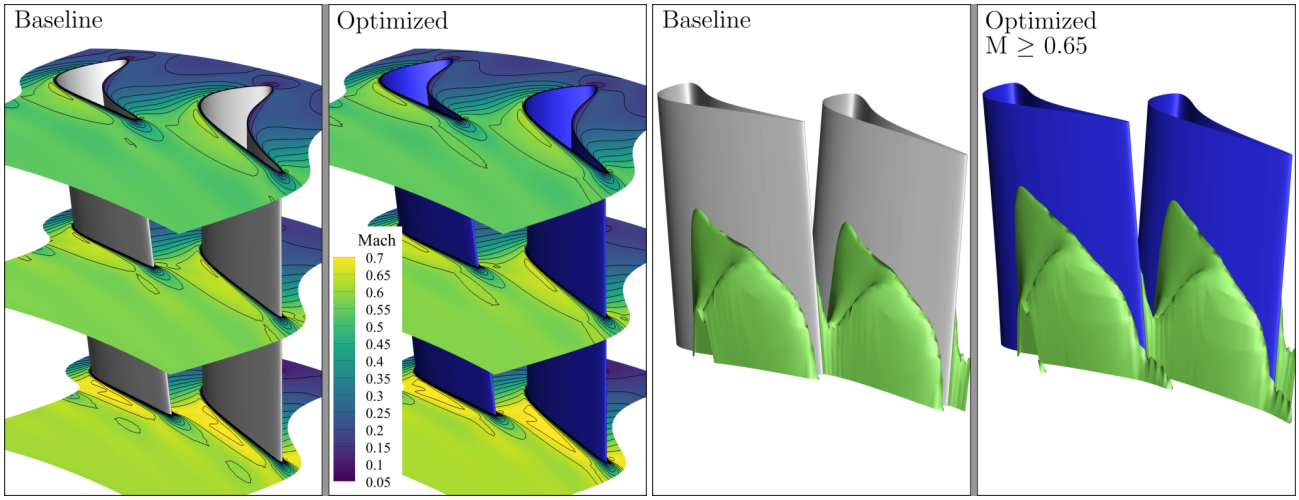

(**a**) hub, mid-span, and shroud contours. (**b**) $M \geq 0.65$ iso-surface.

Fig. 5.30: Harmonic Balance optimized Stator 2 Mach number contours. In both (**a**) and (**b**) the left column shows baseline flow field while the right column shows the optimized flow field. The top of the blade is the location of the shroud surface.

The Stator 2 Mach contours for the harmonic balance optimized blades show a difference in flow changes con-

trary to previous adjustments. The region of flow which exceeds $M_{\text{rel}} \geq 0.65$ has actually increased. While the span-wise location of the flow accelerating past this location is relatively unchanged, a great span-wise proportion of the blade has this high-velocity flow.

5.4.4 Mass-Averaged Entropy trends in Axial direction

To better understand how the previous flow features quantitatively affect the turbomachine performance, the mass-flow averaged entropy was plotted as a function of distance through the machine as seen in Figure 5.31 (**a**) with the percentage difference seen in Figure 5.31 (**a**) . As the entropy difference in (**b**) increases, the better performance the optimized blade has. The harmonic balance optimized design shapes are shown in the dark red background to demonstrate where deformation is occurring and how it corresponds with entropy changes.

From the difference plot in (**b**), most of the performance increase in the harmonic balance optimized blade occurs near the Stator 1 blade's trailing edge. Surprisingly the blade with almost no deformation is responsible for a majority of the performance increase. Stator 1 also had the smallest difference in the baseline harmonic balance to mixing plane entropy comparison.

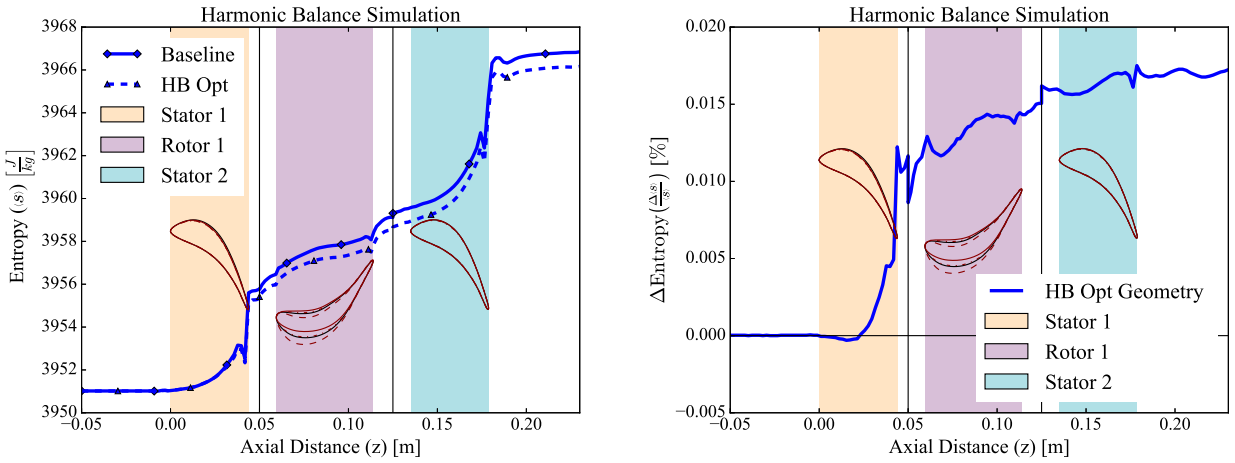

(**a**). (**b**).

Fig. 5.31: Harmonic balance baseline to optimized mass-flow averaged entropy (**a**) and mass-flow averaged entropy difference (**b**) using harmonic balance simulation.

Three possible explanations for this strange behavior are,

1. The small deformation of the Stator 1 blade is solely responsible for the performance benefit.
2. Stator 1 and Rotor 1 are aerodynamically linked, and only the combined deformations of both blades result in the performance benefit
3. The deformation of the Rotor 1 blade is solely responsible for the performance increase due to upstream influence

Explanations 2 and 3 rely on the flow remaining sub-sonic so that the pressure and velocity fields influence upstream conditions. Hypothesis 2 and 3 are tested in section 5.6 as further investigation.

Rotor 1 had the second largest improvement from interface to interface. The leading edge deformation can affect the entropy difference as there is an initial spike at around z = 0.055 m that decreases the entropy difference, which quickly reverses after around z = 0.076. The entropy dip can be explained by the reduced impact of the incoming wake from Stator 1 Figure 5.23 mixing with the Rotor 1 boundary layer. The reduced hub curvature of Rotor 1 leads to a decrease in interaction between the wake and boundary layer, which provides further reduction in entropy generation and increases the entropy difference.

Stator 2 has the smallest change in entropy generation and shows almost no deformation. The lack of blade geometry deformation is at odds with the flow feature difference seen in Figure 5.30 (**b**) that shows an increase in the Mach contour greater than 0.65. The entropy trend along with the blade outlet entropy contour seen in Figure 5.27 (**b**) suggest that even though there is a relatively large increase in flow velocity (up to $M = 0.65$) that mixing losses are not a significant source of entropy.

5.5 MP-based Optimization Results

5.5.1 Blade Shapes

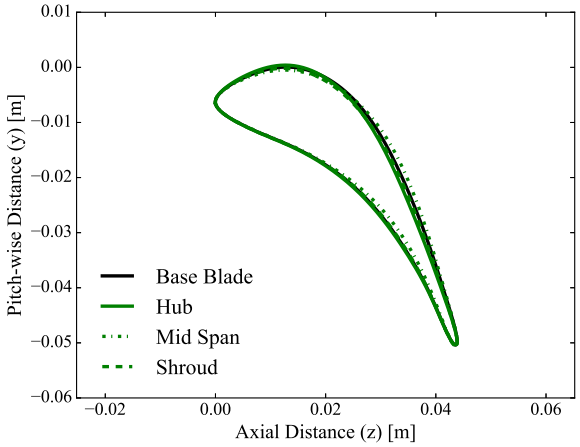

(**a**) Stator 1.

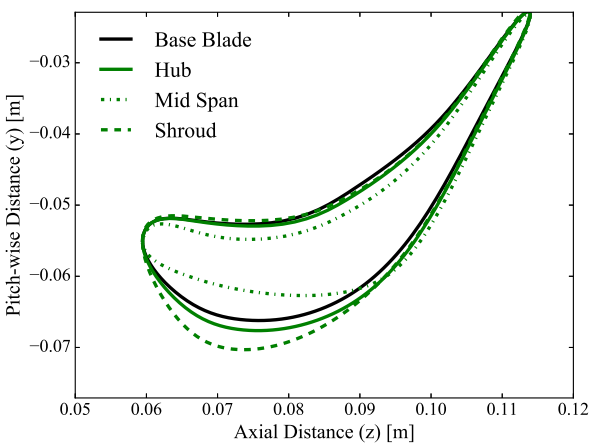

(**b**) Rotor 1.

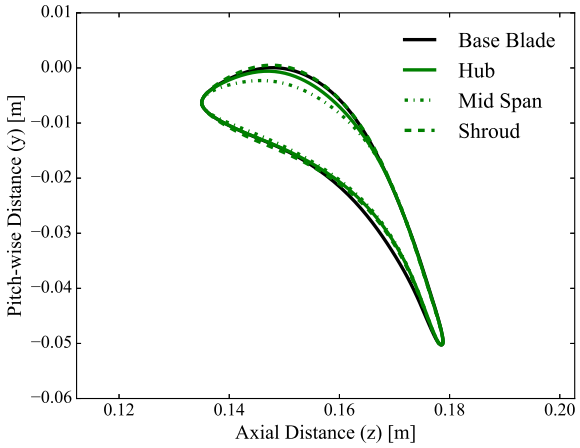

(**c**) Stator 2.

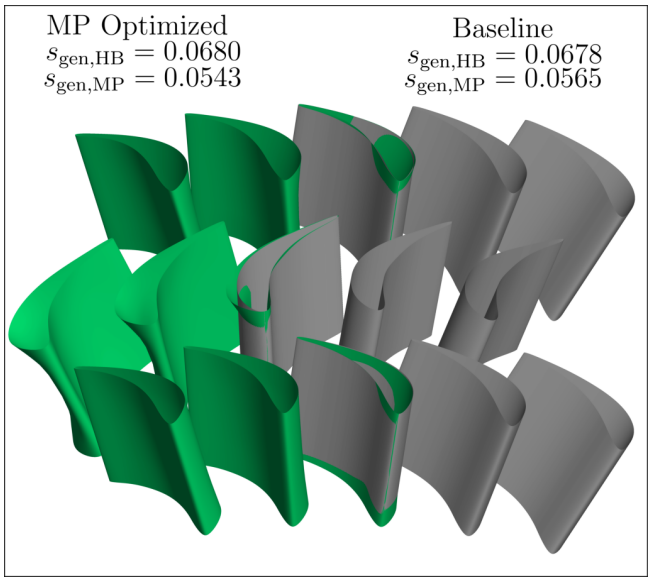

(**d**) Mixing Plane Optimized Blade Shapes.

Fig. 5.32: Mixing Plane Optimized Blade shapes (**a**) Stator 1, (**b**) Rotor 1, (**c**) Stator 2, (**d**) Mixing plane optimized blade comparison to baseline geometry.

The mixing plane optimized blade shapes can be seen in Figure 5.32 with the baseline blade geometry as a black line and the optimized blade geometries in green. The hub, mid-span, and shroud sections are denoted

with solid, dash-dotted, and dashed lines.

The blade with the most considerable deformation is Rotor 1, followed by Stator 2 and Stator 1.

Rotor 1 shows a severe compound lean in the blade with almost the entire suction side curve flattened at the mid-span position while the hub and shroud retained or exaggerated the original blade shape. Interestingly, this blade shape similar to what was found in Ref. [8] except the blade shape in that research was found using a Free-Form deformation box. The shroud shows an increase in blade thickness along the initial curve and an increase in flow turning along the lower surface. The flow turning increase is responsible for the rise in power extraction seen in Figure 5.10 (**b**). The mid-span to shroud span-wise flow should show a change in the flow field from these changes.

In the Stator 2 blade, there is also a compound lean, but it is very slight. The hub has been slightly reduced in thickness while the shroud has maintained its original shape. From these changes, a decrease in flow velocity would be expected at the mid-span position while the hub and shroud see minimal changes to the flow field.

Stator 1 shows the least change in blade shape, with most deformation occurring near the geometric throat. The deformation area is also the location where some of the most extensive surface sensitivity variations appeared in Figure 5.12. Minor deformation has occurred on the blade with a slight thickness reduction on the mid-span section's suction side surface. Minimal changes to the flow field would be expected as a result.

5.5.2 Flow field on secondary planes

The inlet sections are omitted due to mixing plane mass-flow averaging each interface's outlet sections resulting in near-uniform contours. All flow contours and values are from a mixing plane method simulation. For reference of a mixing plane inlet entropy or relative Mach contour refer to Figure 5.1 or Figure 5.4.

5.5.2.1 Stator 1 - Rotor 1

In Figure 5.33 the Mach number contour is shown for the mixing plane baseline and optimized Stator 1 outlet. The flow velocity near the blade's hub increased, and the contour for the largest Mach number has extended further in the span-wise direction in the optimized design than in the baseline.

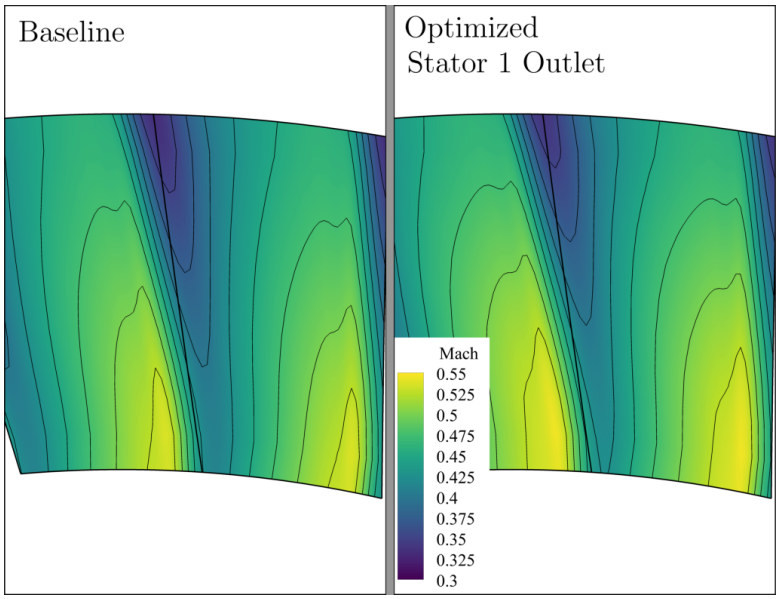

Fig. 5.33: Mixing plane optimized Stator 1 blade outlet Mach number contour. The left contour is the baseline, while the right is the optimized contour.

The increased flow velocity of the hub seen in Figure 5.33 does not come with an increase in mixing-related entropy. Entropy creation is primarily concentrated in the wake as seen in Figure 5.34. The hub section shows a minimal increase of entropy in either the wake or wake-free region. There is a slight increase in wake thickness moving from the hub to the mid-span section. This increase in wake size is accompanied by an increase in average entropy at this axial position.

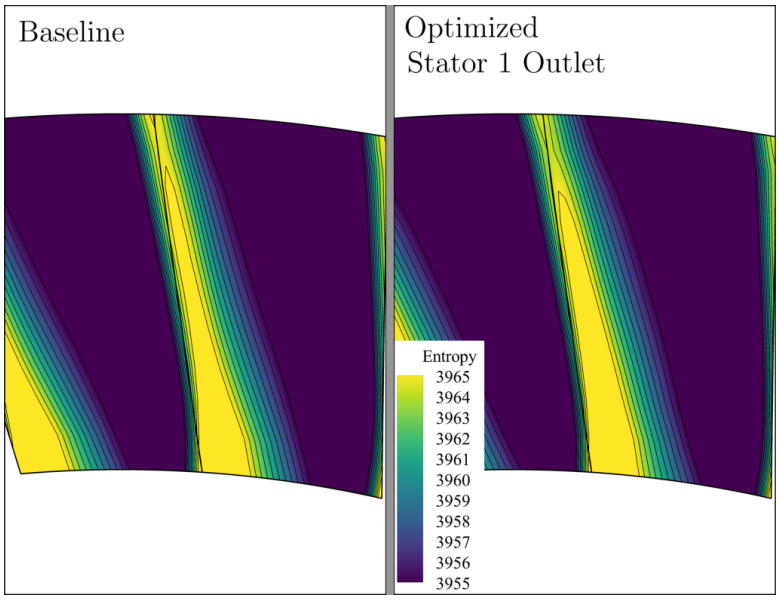

Fig. 5.34: Mixing plane optimized Stator 1 blade outlet entropy contour. The left contour is the baseline while the right is the optimized contour.

5.5.2.2 Rotor 1 - Stator 2

The Rotor 1 interface shows an increase in flow velocity at the shroud position for the optimized blade in Figure 5.35. Span-wise flow is distributed relatively similar between the baseline and optimized blades.

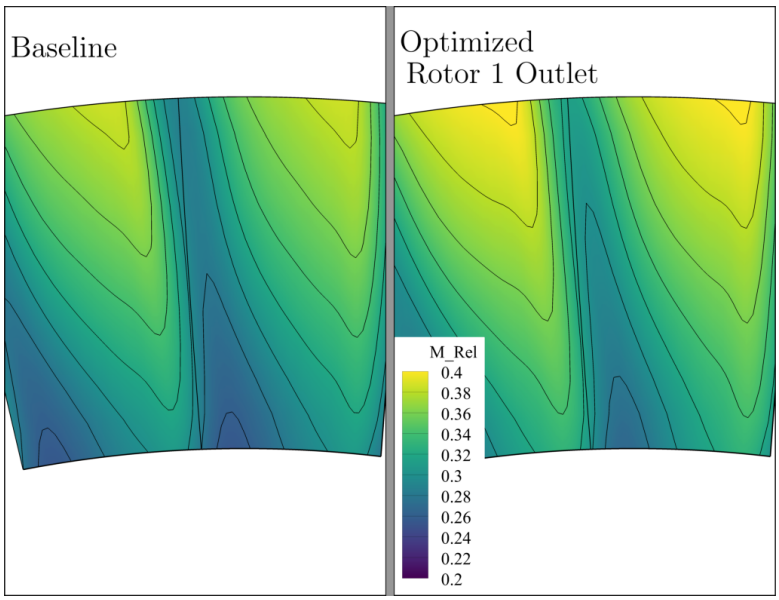

Fig. 5.35: Mixing plane optimized Rotor 1 blade outlet Relative Mach number contour. The left contour is the baseline while the right is the optimized contour.

The optimized Rotor 1 outlet shows a much larger relative flow velocity at the shroud than in the baseline case. Increased flow velocity at the shroud is a consequence of the Rotor 1 blade deformation. The Rotor 1 blade shape has an increased blade thickness at the shroud, as shown in Figure 5.32 (**b**). The increased blade thickness reduces the available area for the fluid to pass through, and due to mass flow conservation, the flow velocity is increased.

Figure 5.36 shows a massive increase in entropy contained in the blade wake of the rotor in the optimized design over the baseline. The rise in the boundary layer's entropy must come from the Rotor 1 blade shape's compound lean. Rotor 1 blade's compound lean results in a larger area of high entropy flow along the blade span. The wake free region shows a similar span-wise entropy distribution between the baseline and optimized blades and can not be a large source of entropy increase.

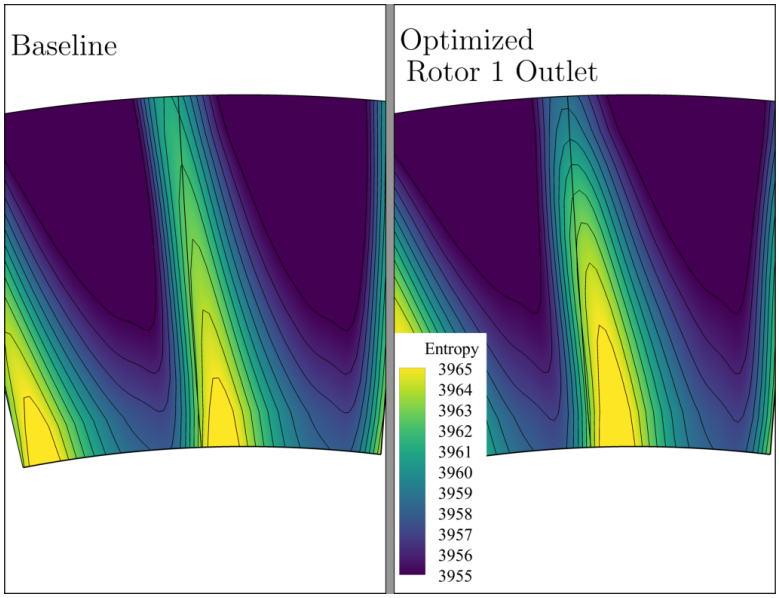

Fig. 5.36: Mixing plane optimized Rotor 1 blade outlet entropy contour. The left contour is the baseline while the right is the optimized contour.

5.5.2.3 Stator 2 outlet

Stator 2 shows a typical flow distribution change usually associated with performance increases. Figure 5.37 shows a decrease in flow velocity at the hub. The blade to blade flow velocity distribution becomes more uniform between the hub and mid-span sections. Flow distribution at the shroud is predominantly similar between the baseline and optimized distribution, as is the blade wake.

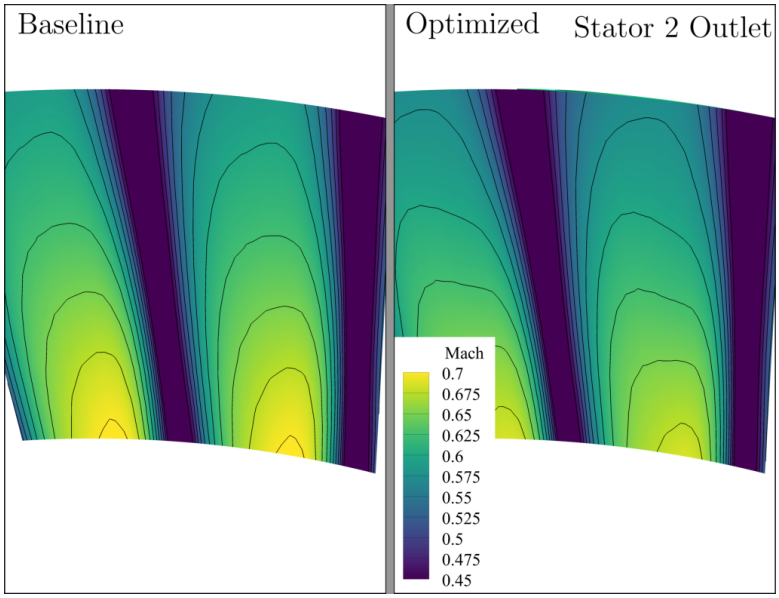

Fig. 5.37: Mixing plane optimized Stator 2 blade outlet Mach number contour. The left contour is the baseline while the right is the optimized contour.

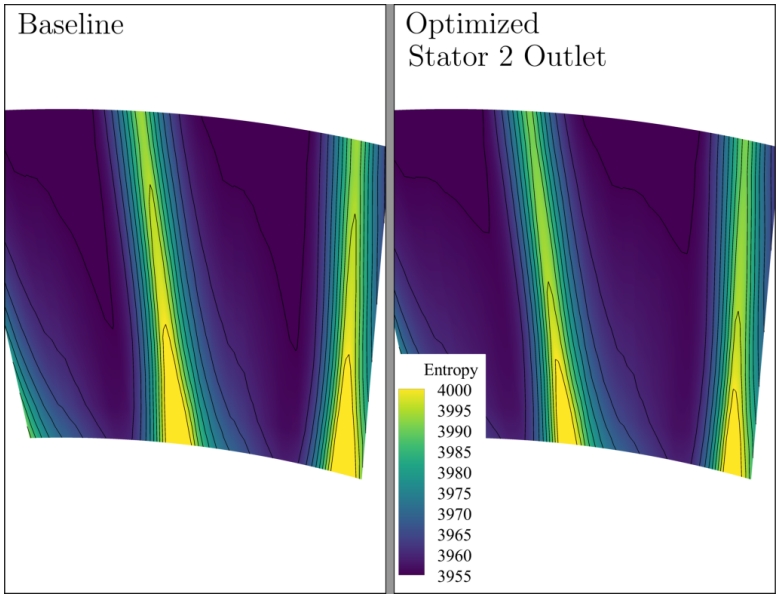

Fig. 5.38: Mixing plane optimized Stator 2 blade outlet entropy contour. The left contour is the baseline while the right is the optimized contour.

In Figure 5.38 the blade outlet entropy contour is shown for the baseline and optimized Stator 2 geometry. A majority of the entropy is contained within the blade wake. The optimized geometry shows a large reduction in entropy contained in the hub region of the wake and maintains a similar blade to blade entropy distribution. The wake-free region shows a higher average entropy in the optimized case than baseline.

The cause of the higher entropy in the wake free region is due to the velocity gradients found in Figure 5.37. As noted previously, mixing is increased in areas with large velocity gradients, and the velocity contour lines of the optimized blades have much sharper edges than the baseline. Sharper contour line edges indicate the velocity difference between the adjacent fluid states is more extensive and, therefore, responsible for the mixing loss increase and higher than baseline entropy.

5.5.3 Flow field on blade to blade planes

5.5.3.1 Stator 1

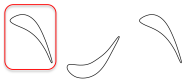

In Figure 5.39 (**a**) the Mach contours are shown for the hub, mid-span, and shroud position while in (**b**) , a Mach number iso-surface for flow above 0.5 is shown for the Stator 1 blade. The baseline design is on the left and optimized design on the right.

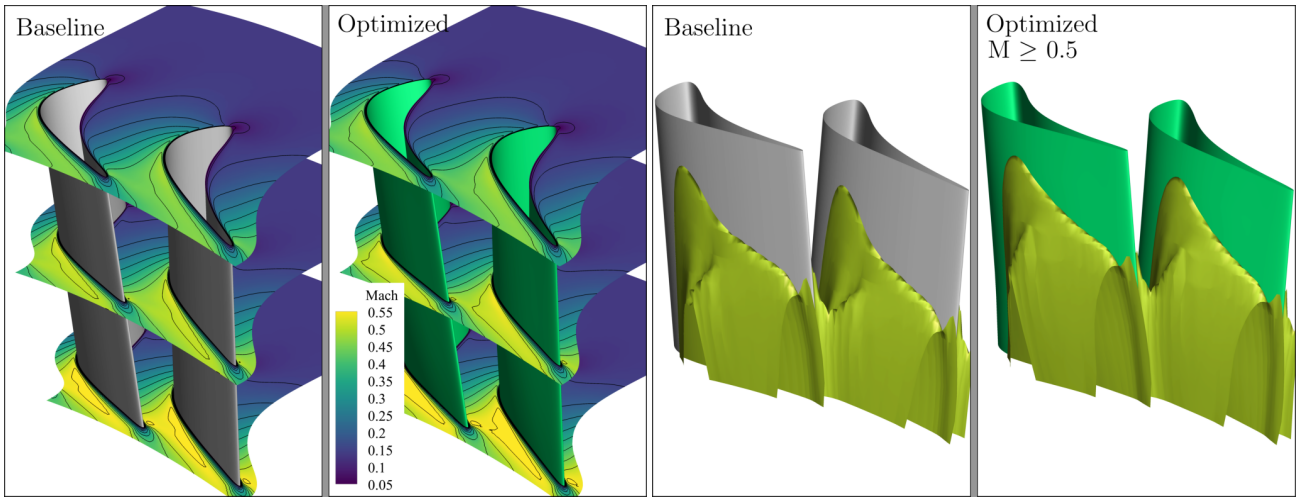

(**a**) hub, mid-span, and shroud contours. (**b**) $M \geq 0.5$ iso-surface.

Fig. 5.39: Mixing plane optimized Stator 1 Mach number contours. In both (**a**) and (**b**) the left contour is the baseline flow field while the right is the optimized flow field. The top of the blade is the location of the shroud surface.

As seen from the Stator 1 outlet interface, the entropy increases in the wake of the optimized blade compared to the baseline shape are due to mixing. In Figure 5.39 (**a**), most of the flow field difference occurs at the hub and mid-span blade sections. The mixing plane optimized blade geometry shows a tremendous increase in flow velocity at the hub's geometric throat. The location in which the flow remains above $M \geq 0.5$ at the geometric throat moves further in the span-wise direction and results in an overall larger portion of the blade with higher velocity flow in (**b**).

5.5.3.2 Rotor 1

In Figure 5.40 (**a**) the relative Mach contours are shown for the hub, mid-span and shroud position while in (**b**) a Mach number iso-surface for flow above 0.45 is shown for the Rotor 1 blade. The mixing plane baseline design is on the left, and the optimized design on the right.

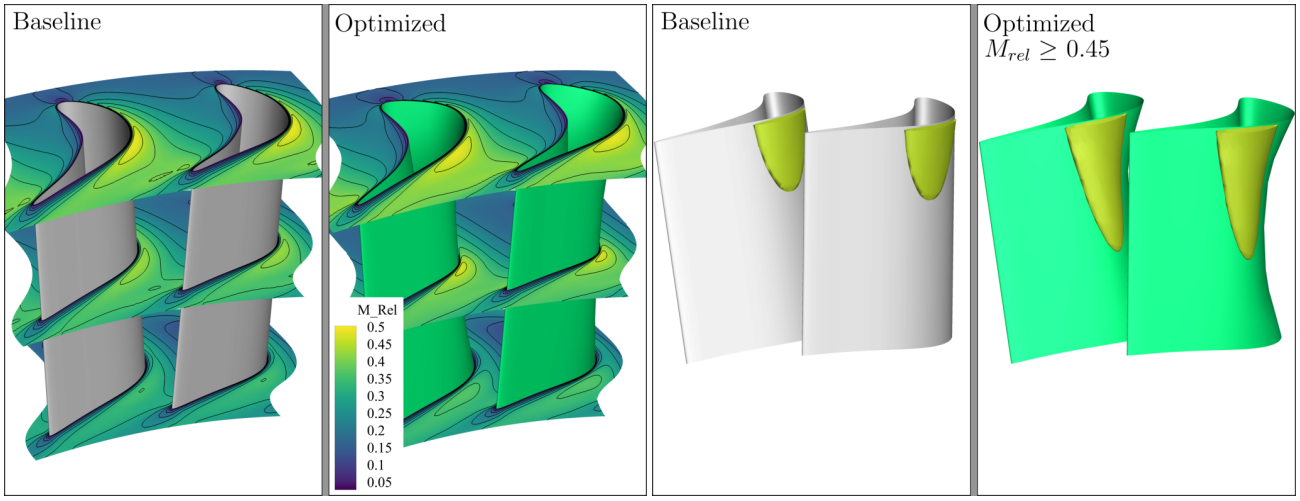

(**a**) hub, mid-span, and shroud contours. (**b**) $M_{\text{rel}} \geq 0.45$ iso-surface.

Fig. 5.40: Mixing plane optimized Rotor 1 Relative Mach number contours. In both (**a**)and (**b**)the left contour is the baseline flow field while the right is the optimized flow field. The top of the blade is the location of the shroud surface.

As expected from the compound lean of the blade, Figure 5.40 (**b**) shows an increase in the span-wise flow, which extends from the shroud to the mid-span section. In both (**a**) and (**b**), the high-velocity flow regions are increased and moved further towards the optimized geometry's geometric throat. The result of this increase in flow velocity was seen directly at the outlet interface in Figure 5.36 with the large increase of entropy in the wake. The entropy contour at the wake has a much larger area of higher entropy. The diffuse entropy region between the wake and wake-free regions is larger as well. As seen in Figure 5.40 (**a**) the flow velocity at the hub and mid-span position rose.

5.5.3.3 Stator 2

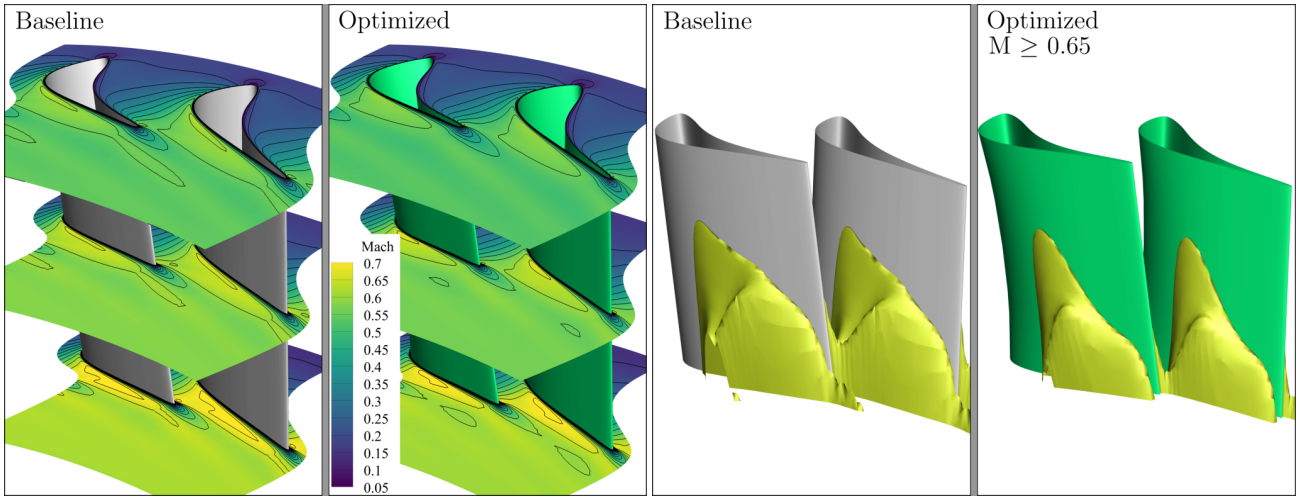

(**a**) hub, mid-span, and shroud contours. (**b**) $M \geq 0.65$ iso-surface.

Fig. 5.41: Mixing plane optimized Stator 2 Mach number contours. In both (**a**) and (**b**) the left contour is the baseline flow field while the right is the optimized flow field. The top of the blade is the location of the shroud surface.

In Figure 5.41 (**a**), the Mach contours are shown for the hub, mid-span, and shroud position. In contrast, (**b**)

shows a Mach number iso-surface for flow above 0.65 for the Stator 2 blade.

Whereas Rotor 1 had an increase and delay in flow velocity due to the compound lean, the Stator 2 blade shows a considerable reduction in high-velocity flow, especially between the mid-span and hub region of the optimized flow seen in Figure 5.41. The span-wise position of the flow above $M \geq 0.65$ has been lowered until it nearly coincides with the hub. The reduction in span-wise flow and an overall decrease in high-velocity flow past the geometric throat is responsible for the entropy contour decrease seen at the Stator 2 blade outlet in Figure 5.38.

5.5.4 Mass-Averaged Entropy trends in Axial direction

For a quantitative investigation of the optimization's performance, the mass-flow average entropy is plotted against axial position in Figure 5.42 (**a**) with the difference from the baseline mixing plane entropy in (**b**). The mixing plane optimized blade shapes are shown in the dark red background to demonstrate where deformation is occurring and how it corresponds with entropy changes.

In Figure 5.42 (**b**) the optimized design demonstrates worse performance compared to the baseline design until the Stator 2 blade as indicated by the Stator 1 and Rotor 1 outlet entropy trends. Individual sections within the Stator 1 and Rotor 1 blade deformation regions show an improvement from preceding axial locations. The performance gains are usually negated by mixing at the trailing edge. While the optimizer has correctly calculated design changes that increase a blade's local performance, regions outside the blade shape's direct influence completely negate the performance increases. The modified leading edge of the Rotor 1 blade causes a massive drop in performance. The subsequent deformations creating a compound lean of the blade make up for the performance drop.

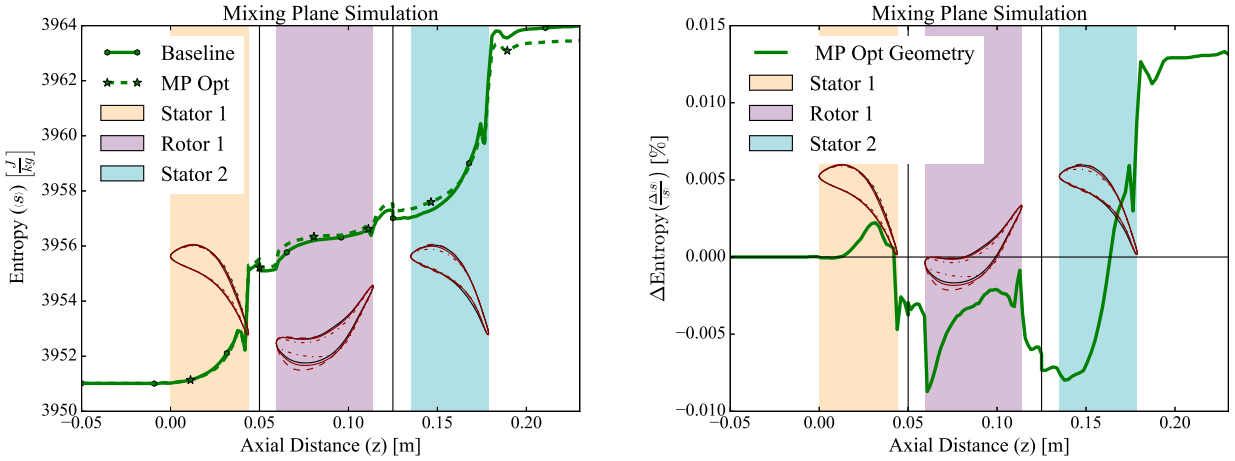

(**a**). (**b**).

Fig. 5.42: Mixing plane baseline to optimized (**a**) mass-flow averaged entropy trend and (**b**) mass-flow averaged entropy trend difference using a mixing plane solver.

Interestingly the Stator 2 blade shows the best performance of any blade previously seen in either mixing plane or harmonic balance optimizations. The Stator 2 blade performance benefit is near twice as good as the previous blades were bad. This result is precisely opposite the harmonic balance optimization results in which the Stator 2 blade was the worst-performing.

5.6 Hybrid Design Hypothesis

In Figure 5.43 both the harmonic balance (HB) and mixing plane (MP) based optimized designs are simulated with both (**a**) harmonic balance and (**b**) mixing plane methods and differenced with the baseline entropy distribution for the respective flow solver. The HB optimized design is seen in blue while the MP optimized design is in green in both (**a**) and (**b**).

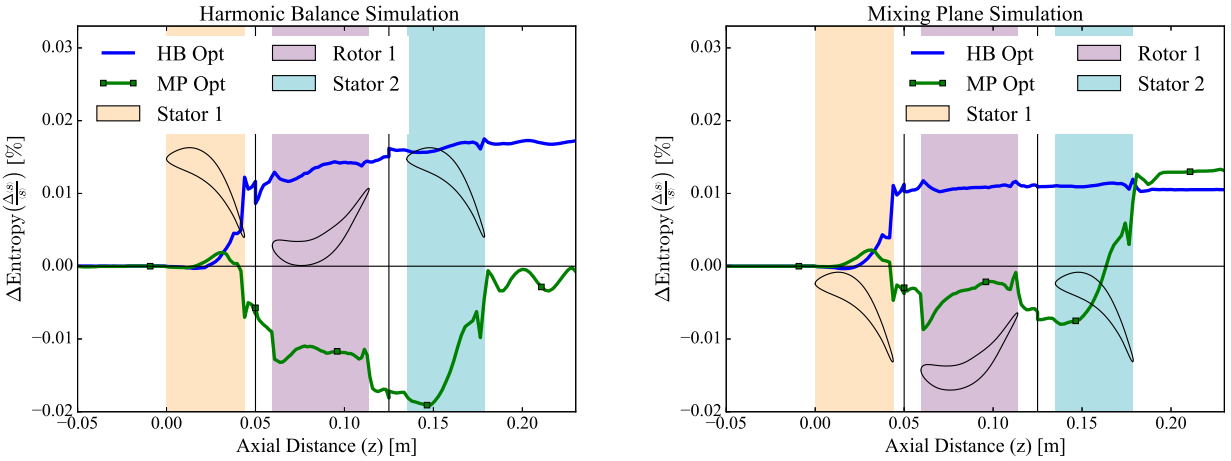

(**a**) Harmonic balance solver.

(**b**) Mixing plane solver.

Fig. 5.43: Harmonic balance and mixing plane optimized blades mass-flow averaged entropy difference using the (**a**) harmonic balance and (**b**) mixing plane solvers.

In Figure 5.43 (**a**) the performance differences are seen for the harmonic balance method simulation. The HB optimized design improvement is almost entirely found at the trailing edge of the Stator 1 blade. There is a slight improvement of the Rotor 1 blade and a near-zero change of the Stator 2 blade. The MP optimized design performance is only slightly worse than the original design and has near-identical overall entropy generation, but an interesting result is seen in the Stator 2 performance. While the Stator 1 and Rotor 1 blades perform much worse than the original design, the Stator 2 blade performs so well it corrects for the underperforming blades of the design.

Figure 5.43 (**b**) shows both designs' performance when using the mixing plane method for simulation. Like the harmonic balance simulation results, nearly all of the HB optimized design's performance increase stems from the Stator 1 blade. Likewise, the MP optimized design in that all of the performance benefit results from the Stator 2 blade. The MP optimized design outperforms the HB optimized design by a slight margin using the mixing plane method.

The two major improvement zones are interesting as both designs have a majority of the performance benefit resulting from only a single blade. There is near zero deformation to the Stator 1 blade geometry in the HB optimized design, as can be seen in Figure 5.21 (**a**). As the flow conditions are sub-sonic, a possibility for the change in flow conditions in the absence of local geometry deformation is the aerodynamic coupling or upstream influence [6] of the Rotor 1 blade. There is a local deformation to the blade in the MP optimized case, which appears to be responsible for boosting performance.

As the improvements in both optimized designs appear to result from two different situations, there are two hypotheses made for further performance increases.

Design: Hypothesis

C1: Performance gain can be made by selecting the best performing blade. Aerodynamic coupling plays a minimal role in performance increases.

C2: Performance gain from harmonic balance method optimization stems from aerodynamically linked Stator 1 and Rotor 1 blades and are thus required together. Stator 2 performance is insensitive to changes, and it is possible to replace the blade shape with a better performing geometry to increase overall performance.

Each design was simulated with both harmonic balance and mixing plane methods. The hybrid design geometries are reported in Table 5.1.

	Design	
	C1	**C2**
Zone	Geometry Used	
Stator 1	MP Optimized Stator 2	HB Optimized Stator 1
Rotor 1	HB Optimized Rotor 1	HB Optimized Rotor 1
Stator 2	MP Optimized Stator 2	MP Optimized Stator 2

Table 5.1: Design exploration for hybrid designs.

5.7 C1 Design

5.7.1 Blade Shapes

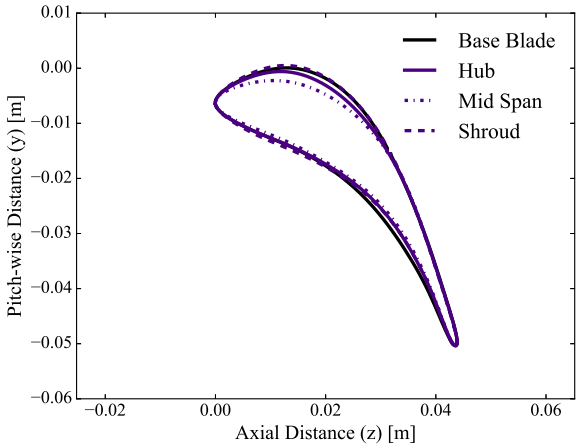

(**a**) Stator 1.

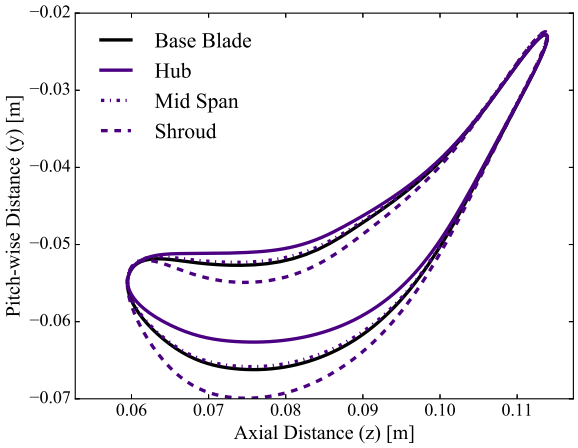

(**b**) Rotor 1.

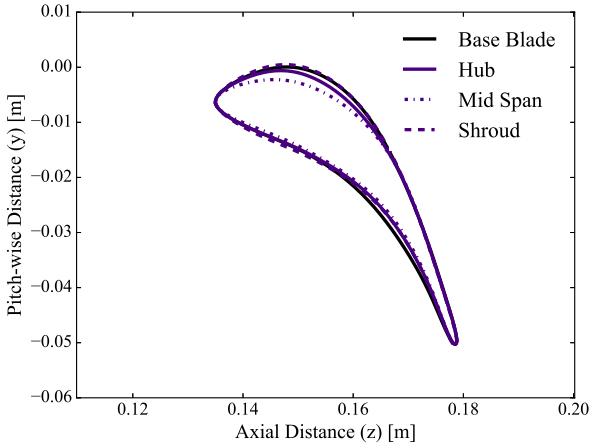

(**c**) Stator 2.

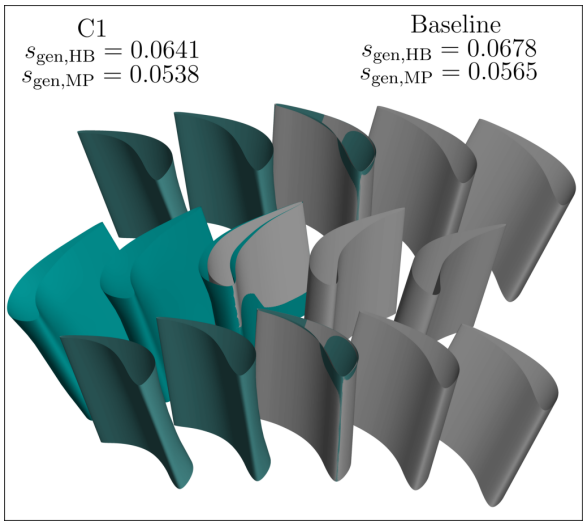

(**d**) C1 Blade Shapes.

Fig. 5.44: C1 design blade shapes (**a**) Stator 1, (**b**) Rotor 1, (**c**) Stator 2, (**d**) C1 design blade comparison to baseline geometry.

The C1 design tested the influence of the best-performing individual blades. The design geometries can be seen in Figure 5.44. The mesh for the new design used the parameterization changes of the blade to deform the baseline mesh in the same way the optimizer changes the mesh when taking a design step.

5.7.2 Mass-Averaged Entropy trends in Axial direction

The C1 design shows a performance increase in both harmonic balance and mixing plane simulations over the single method based optimization design.

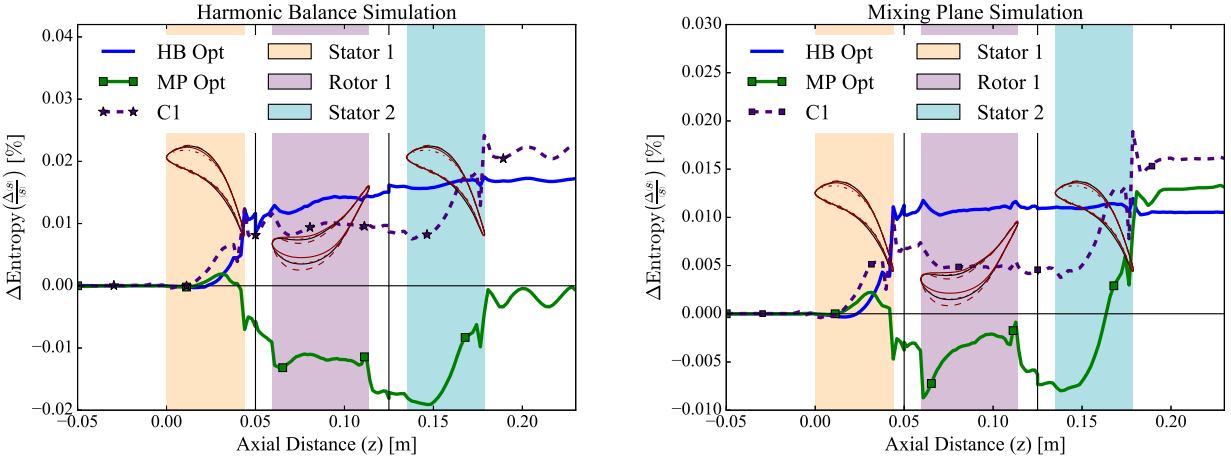

(**a**) Harmonic balance solver.

(**b**) Mixing plane solver.

Fig. 5.45: Hybrid design C1 mass-flow averaged entropy difference using (**a**) harmonic balance and (**b**) mixing plane solvers.

Figure 5.45 shows the harmonic balance, mixing plane, and C1 blade shapes mass-averaged entropy trends in the axial direction using both the harmonic balance (**a**) and mixing plane (**b**) methods. The HB optimized design entropy trend is shown as a solid blue line, while the MP optimized design entropy trend is shown as a solid green line. The C1 entropy trend is shown as a dashed purple line.

The MP optimized Stator 2 blade was chosen for use in both stator positions of design C1 as it showed the best individual performance of all blades. Neither the Stator 1 or Stator 2 blades in the C1 design demonstrate as large a performance increase as the Stator 2 blade in the MP optimized design, even though they have identical geometries. This trend of reduced performance benefit is seen in both harmonic balance (**a**) and mixing plane simulations (**b**).

The Rotor 1 blade shows a change in entropy trend from the original HB optimized design entropy trend in both (**a**) and (**b**). Rotor 1 performance decreases between the leading and trailing edges in the C1 design compared to the HB optimized design. This difference in behavior shows that there is still a robust aerodynamic coupling between the blades. Although the HB optimized Stator 2 shows almost no performance benefit or cost, when the blade is changed to the mixing plane optimized Stator 2, a performance cost is imposed on the Rotor. The Rotor's performance decrease is subsequently made up by the MP optimized Stator 2 blade's performance increase. The Stator 2 blade's performance increase is less in the C1 configuration than the original MP optimized design even though it is the same blade shape and in the same location.

The mixing plane simulation in Figure 5.45 (**b**) shows a similar performance boost of the MP optimized Stator 2 blade in the C1 configuration. However, the performance increase has been reduced in the Stator 1 position. As seen in Figure 5.45 (**b**), the performance benefit from the Stator 2 geometry is decreased when used in the C1 configuration instead of the purely MP optimized design.

5.8 C2 Design

5.8.1 Blade Shapes

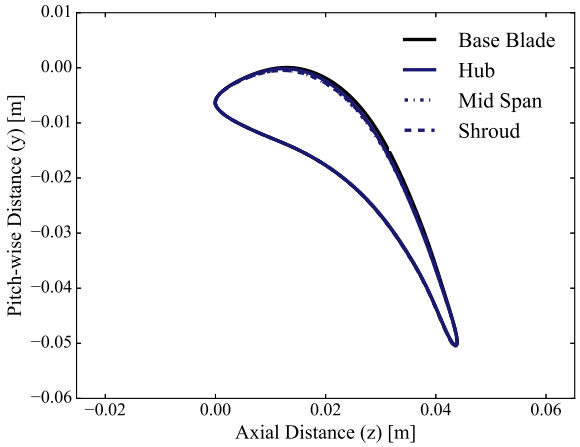

(**a**)Stator 1.

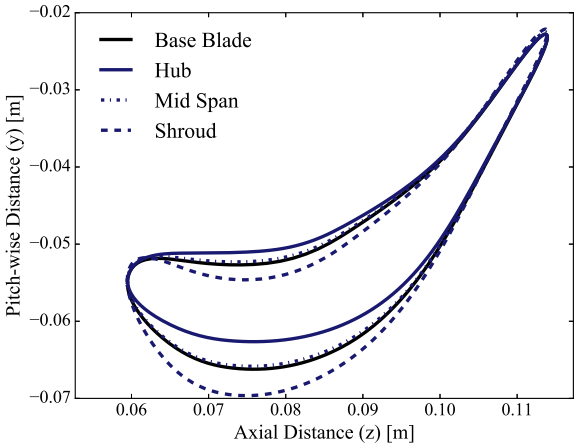

(**b**) Rotor 1.

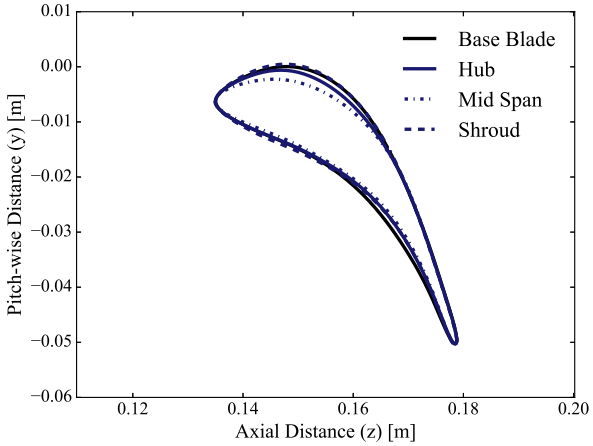

(**c**) Stator 2.

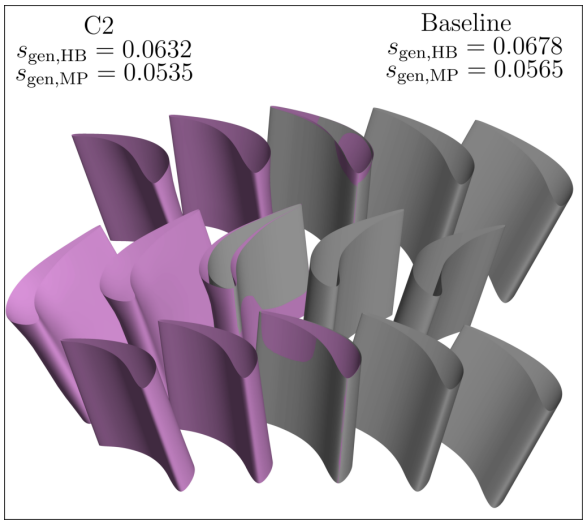

(**d**) C2 Blade Shapes.

Fig. 5.46: C2 Design blade shapes (**a**) Stator 1, (**b**) Rotor 1, (**c**) Stator 2, (**d**) C2 design blade comparison to baseline geometry.

The C2 design configuration tests the importance of aerodynamic coupling of the blades on performance increase. Blade geometries can be seen in Figure 5.46. The mesh for the new design used the parameterization changes of the blade to deform the baseline mesh in the same way the optimizer changes the mesh when taking a design step.

5.8.2 Mass-Averaged Entropy trends in Axial direction

The C2 configuration tested the hypothesis that the aerodynamic coupling between the Stator 1 and Rotor 1 blades was the primary reason for increased performance. In contrast, the Stator 2 blade could be modified for further improvement. The MP optimized Stator 2 blade was used for the C2 Stator 2 blade as it performed

better than the initial HB optimized Stator 2 blade. Overall the C2 configuration outperforms both the HB and MP optimized blades. The hybrid design performs well and provides a positive result for the hybrid design hypothesis. In Figure 5.47 the entropy differences in both harmonic balance and mixing plane simulations were compared to the baseline. The HB optimized design entropy trend is shown as a solid blue line, while the MP optimized design entropy trend is shown as a solid green line. The C2 design entropy trend is shown as a solid dark blue line..

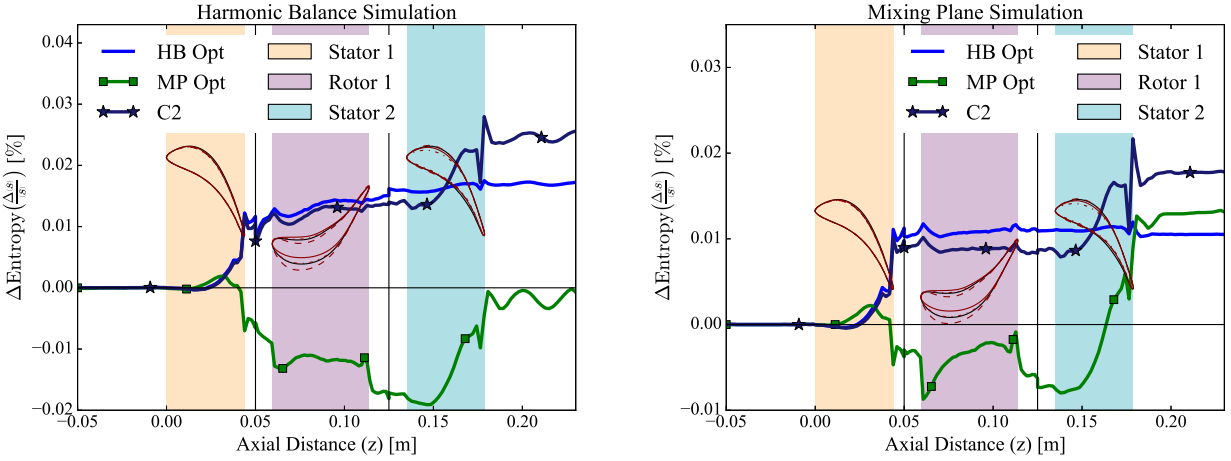

(**a**) Harmonic balance solver.

(**b**) Mixing plane solver..

Fig. 5.47: Hybrid design C2 mass-flow averaged entropy difference for (**a**) Harmonic Balance and (**b**) Mixing Plane solvers.

In Figure 5.47 (**a**), the trend for the C2 configuration follows the original HB optimized difference trend quite closely until the Stator 2 blade. The slight difference between the HB optimized and C2 entropy trends demonstrates the Stator 2 blade geometry change's upstream effect, but it is relatively small. Like the C1 configuration, the Stator 2 performance increase is somewhat lessened between its use in the MP optimized design and its use in the C2 configuration. Overall the C2 configuration outperforms the solely harmonic balance or mixing plane optimized designs.

The mixing plane simulation in (**b**) shows a similar trend as the harmonic balance simulation. For the C2 design, the initial gains stemming from the HB optimized Stator 1 and Rotor 1 blades are still present, but the overall increase is slightly less. The difference is due to the Stator 2 blade. There is some upstream influence due to the MP optimized blade, but the blade's performance increases outweigh the upstream influence cost on the Rotor 1 blade performance.

5.9 Summary of Performance

	$s_{\text{gen}}[-]$		$\frac{\Delta s_{\text{gen}}}{s_{\text{gen,basline}}}[\%]$	
	Harmonic Balance	Mixing Plane	Harmonic Balance	Mixing Plane
Baseline	0.0678	0.0565	-	-
HB Optimized	0.0645	0.0546	-4.87	-3.36
MP Optimized	0.0680	0.0543	+0.29	-3.89
C1	0.0641	0.0538	-5.46	-4.78
C2	0.0632	0.0535	-6.78	-5.31

Table 5.2: Overall Performance s_{gen} and percentage difference from baseline parameters for M0 mesh in both harmonic balance and mixing plane simulation type for Baseline, Harmonic Balance Optimized, Mixing Plane Optimized, C1, and C2 Designs.

All design performance characteristics are shown in Table 5.2. The HB optimized design offers a 4.87% reduction of entropy generation in a harmonic balance simulation and a 3.36% reduction when using a mixing plane simulation. The MP optimized design shows a 0.29% increase in entropy generation in a harmonic balance simulation and a 3.89% reduction in entropy generation with the mixing plane simulation. A conclusion drawn from these results is that a performance benefit from a harmonic balance based optimization is applicable when simulated with unsteady and steady methods. The performance benefit obtained from a mixing plane optimized design may not be applicable when simulated with an unsteady solver. While this conclusion is only shown in this one test case, further investigation is needed to verify how robust the finding is.

Regarding the hybrid hypothesis and configurations C1 and C2, the overall hypothesis that an increased performance benefit can be realized with hybrid designs is true. Both hypotheses lead to better performing designs. The best performing configuration is C2 with a 6.78% and 5.31% reduction in entropy generation in harmonic balance and mixing plane simulations. Configuration C1 also has better performance than the designs stemming from an optimization using a single method. With an entropy generation reduction of 5.46% and 4.78% respectively in harmonic balance and mixing plane simulations.

The design improvement follows conventional wisdom that aerodynamic coupling can have a strong influence on turbine performance in sub-sonic flow regimes. While both hybrid designs have improved performance compared to a design resulting from an optimization using a single method, the better approach favors aerodynamically coupled geometry changes. Interestingly both hybrid configurations outperform the single method optimization designs when coupled with the MP optimized Stator 2 blade, as can be seen in Figure 5.48. further exploration is needed to answer whether the MP optimized Stator 2 blade performs well in the C1 and C2 configurations because MP optimized blades are suited for Stator performance or the last blade in the design is not influenced by another blade downstream.

Figure 5.48 shows all optimized and hybrid configuration differences in both harmonic balance and mixing plane simulations. The harmonic balance and mixing plane optimized entropy trends are shown as a solid blue and green line. The hybrid configurations C1 and C2 are shown in a dashed purple and solid dark blue color.

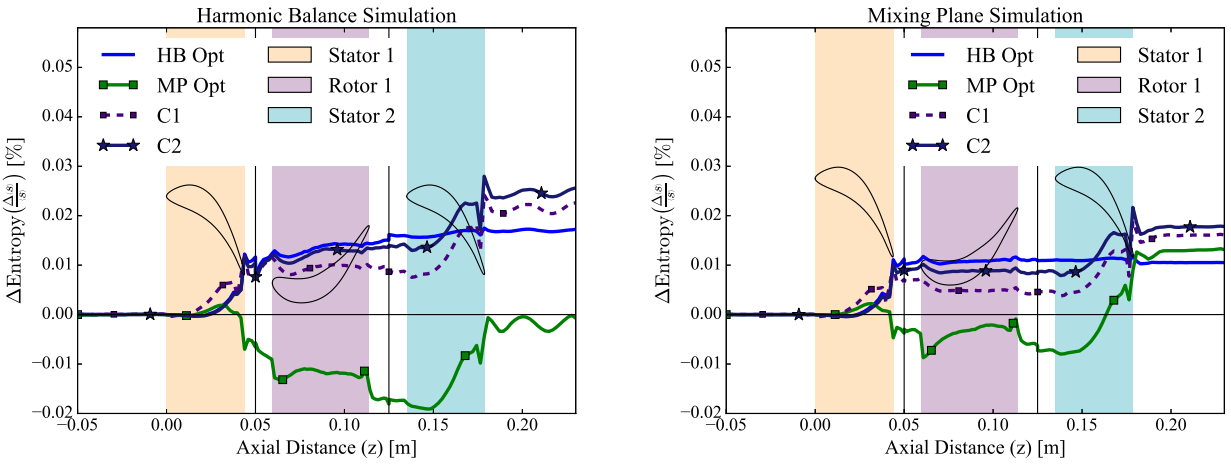

(**a**). (**b**).

Fig. 5.48: All designs mass-flow averaged entropy difference in (**a**) harmonic balance and (**b**) mixing plane simulations of M0 mesh count.

Although this study's primary focus is on optimization results due to computational constraints, a grid-dependent mesh was used. The designs were simulated with finer meshes, and the entropy trend was analyzed to verify if the locations of performance changes in the grid-dependent mesh transferred to the grid-independent solution. Figure 5.49 shows the grid converged entropy differences for all designs in both harmonic balance and mixing plane simulations. All designs in both harmonic balance and mixing plane simulations, except for the MP Optimized design simulated using the harmonic balance method, perform better than the baseline design until the geometric throat of Stator 2. After the geometric throat, all performance increase is lost. A useful note is that the Stator 2 geometric throat is the only area in which the flow approaches a Mach number ≥ 0.65, which is beginning to encroach on the low trans-sonic regime of internal flows. The performance benefits obtained in

the subsonic flow regime of Stator 1 and Rotor 1 carryover from the grid-dependent optimized designs to the grid converged results.

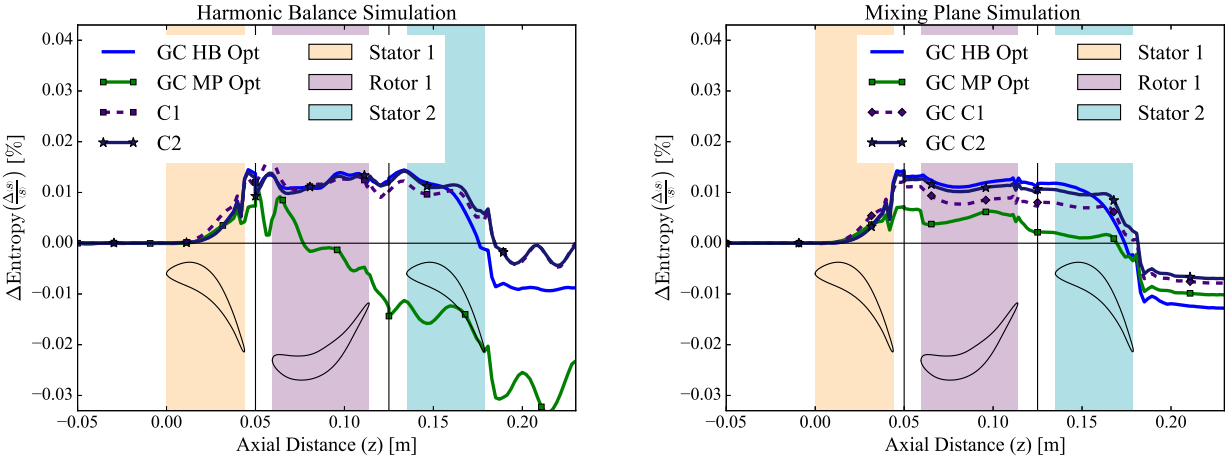

(**a**) (**b**)

Fig. 5.49: All designs mass-flow averaged entropy difference in (**a**) harmonic balance and (**b**) mixing plane simulations with a grid converged mesh.

The most significant divergence between the grid-dependent and grid converged mesh's expected behavior occurs only in the trans-sonic flow region. The entropy trend similarities point to future optimization design chain simplification in that grid-dependent meshes can still be used to optimize designs operating below the trans-sonic regime. The results that unsteady optimization can perform better than a mixing plane optimized design leads to a preference for using harmonic balance based optimization. Even though sizeable computational scaling consequences imposed in harmonic balance optimization, the decreased mesh resolution requirements could still lead to better performing designs.

The entropy difference trends for the harmonic balance method seen in Figure 5.49 (**a**) shows that configurations C1 and C2 are nearly identical. Nevertheless, in Table B.1 configuration C2 shows one percentage point difference in entropy generation. This seemingly contradictory result comes as a consequence of the comparison method. Because the entropy difference trend only compares the mass-flow average entropy at a specific axial location, the interface can affect the final entropy value. Figure B.9 and Figure B.12 show that the interface's entropy difference is not the same. Although the end entropy value is the same between the C1 and C2 configurations, a differing amount of entropy is passed between the interfaces, which results in different objective values. This difference highlights an essential aspect of further multizone optimization. The global difference between inlet and outlet quantity values may be small; the interim interfaces can lead to much different results. Further investigation of enforcing specific residual and flow quantities on the inlet and outlet of interfaces in a multi-point objective optimization is recommended. Additional comparison between the grid-dependent and grid-independent losses can be seen in Appendix B.

Chapter 6

Conclusions and Recommendations

6.1 Conclusions

This study compared the results of harmonic balance and mixing plane optimization on a 3D 1.5 stage turbine. The results indicate that a harmonic balance optimized design leads to better or comparable performance to mixing plane optimized design. Steady mixing plane optimization only performs better when using a mixing plane simulation and performs worse than the initial design when simulated with the harmonic balance method. Further testing showed that hybrid designs that mix blade geometries from different optimization methods outperform designs resulting from optimization using a single method. The different designs' entropy trends show that the most consistent performance increases stem from optimizing aerodynamically linked blades. Entropy trends also show that while an optimization process may be globally successful in multizone machines, an individual blade may not produce any performance benefits. Verification shows that performance benefits obtained from optimization on a grid-dependent mesh are maintained until the flow velocity approaches the trans-sonic flow regime of $M \geq 0.7$ and quickly drops off afterward.

The conclusions of this work can be summarized in the bullets below.

- Harmonic balance blade surface sensitivity has less variation than steady mixing plane sensitivity, especially in regions past a blade's geometric throat.
- Harmonic balance optimized designs had better performance than mixing plane optimized designs in unsteady simulations and comparable results in steady simulations.
- Mixing plane method optimization did not guarantee individual blade performance increases.
- Hybrid designs using blade geometries from both harmonic balance and mixing plane method optimization perform better than designs optimized using a single method.
- Optimized aerodynamically coupled blades have a more significant impact on machine performance than using the individual 'Best' performing blades.

6.2 Recommendations

- Perform multizone optimization enforcing performance increases between blades instead of the end of the stage.
- Perform a similar harmonic balance and mixing plane method optimization comparison with a supersonic test case.
- Examine design performance of stator blades optimized using mixing plane methods and rotor blades optimized using harmonic balance.
- Extend $SU2$ capabilities for larger RAM usage and processor count.
- Study previous works to determine if performance increases in 2D multistage optimized cases are due to a singular well-performing blade or if increases are spread equally among all blades.

Bibliography

[1] John F 1936 Wendt, John D Jr. (John David) Anderson 1937-, and Von Karman Institute for Fluid Dynamics. T A T T . Computational fluid dynamics : an introduction, 2009. URL https://doi.org/10.1007/978-3-540-85056-4https://link.springer.com/openurl?genre=book&isbn=978-3-540-85055-7http://bvbr.bib-bvb.de:8991/F?func=service&doc_library=BVB01&doc_number=016964713&line_number=0001&func_code=DB_RECORDS&service_type=MEDIAhttp://ezproxy.st-andrews.ac.uk/login?url=http://dx.doi.org/10.1007/978-3-540-85056-4https://link.springer.com/book/10.1007/978-3-540-85055-7https://link.springer.com/10.1007/978-3-540-85056-4http://public.eblib.com/choice/PublicFullRecord.aspx?p=6312633.

[2] Thomas Léonard, Laurent Y.M. Gicquel, Nicolas Gourdain, and Florent Duchaine. Steady/unsteady reynolds- averaged Navier-Stokes and large eddy simulations of a turbine blade at high subsonic outlet mach number. *Journal of Turbomachinery*, 137(4), 2015. ISSN 15288900. doi: 10.1115/1.4028493.

[3] P G Tucker. Computation of unsteady turbomachinery flows: Part 1—Progress and challenges. *Progress in Aerospace Sciences TA - TT -*, 47(7):522–545, 2011. ISSN 0376-0421. doi: 10.1016/j.paerosci.2011.06.004LK-https://tudelft.on.worldcat.org/oclc/5903232844.

[4] Antonio Rubino. *Reduced Order Models For Unsteady Fluid Dynamic Optimization of Turbomachinery*. 2019. ISBN 9789462339583. doi: 10.4233/uuid:11bb7f0d-c39b-4a32-8936-6ff8905543e1.

[5] Kenneth C Hall, Kivanc Ekici, Jeffrey P Thomas, and Earl H Dowell. Harmonic balance methods applied to computational fluid dynamics problems. *International Journal of Computational Fluid Dynamics*, 27 (2):52–67, feb 2013. ISSN 1061-8562. doi: 10.1080/10618562.2012.742512. URL https://doi.org/10.1080/10618562.2012.742512.

[6] E. M. Greitzer, C. S. Tan, and M. B. Graf. *Internal Flow*. 2004. doi: 10.1017/cbo9780511616709.

[7] John D. Denton. Multall—An Open Source, Computational Fluid Dynamics Based, Turbomachinery Design System. *Journal of Turbomachinery*, 139(12), 09 2017. ISSN 0889-504X. doi: 10.1115/1.4037819. URL https://doi.org/10.1115/1.4037819. 121001.

[8] S. Vitale, M. Pini, and P. Colonna. Multistage turbomachinery design using the discrete adjoint method within the open-source software su2. *Journal of Propulsion and Power*, 2020. ISSN 15333876. doi: 10.2514/1.B37685.

[9] Yin Yu, Zhoujie Lyu, Zelu Xu, and Joaquim R.R.A. Martins. On the influence of optimization algorithm and initial design on wing aerodynamic shape optimization. *Aerospace Science and Technology*, 75:183–199, 2018. ISSN 12709638. doi: 10.1016/j.ast.2018.01.016. URL https://doi.org/10.1016/j.ast.2018.01.016.

[10] Gabor Janiga Dominique Thevenin. *Optimization and Computational Fluid Dynamics*. 2008. ISBN 978-3-540-72153-6. doi: 10.1007/978-3-540-72153-6.

[11] Hendrik (author) Gaens. Best Practices for Adjoint-based Shape Optimization of Turbomachinery Stages LK - https://tudelft.on.worldcat.org/oclc/1158180586, 2020. URL http://resolver.tudelft.nl/uuid:76a73cd4-5595-4486-bc26-bfe54098deb7.

[12] N. Anand, S. Vitale, M. Pini, and P. Colonna. Assessment of FFD and CAD-based shape parametrization methods for adjoint-based turbomachinery shape optimization. 2018.

[13] Pablo (author) Garrido de la Serna. Adjoint-based 3D Shape Optimization for Turbomachinery Applications LK - https://tudelft.on.worldcat.org/oclc/1130743752, 2019. URL http://resolver.tudelft.nl/uuid:d8d5dfcf-a5ac-4b54-bac5-9f78fb15f786.

[14] J. D. Denton. Loss mechanisms in turbomachines. *Journal of Turbomachinery*, 115(4):621–656, 1993. ISSN 15288900. doi: 10.1115/1.2929299.

[15] Penghao Duan, Choon S. Tan, Andrew Scribner, and Anthony Malandra. Loss generation in transonic turbine blading. *Journal of Turbomachinery*, 140(4):1–12, 2018. ISSN 15288900. doi: 10.1115/1.4038689.

[16] Sungho Yoon, Thomas Vandeputte, Hiteshkumar Mistry, Jonathan Ong, and Alexander Stein. Loss audit of a turbine stage. *Journal of Turbomachinery*, 138(5):1–9, 2016. ISSN 15288900. doi: 10.1115/1.4032138.

[17] L. Piegl and W. Tiller. The NURBS Book. *Computer-Aided Design*, 1996. ISSN 00104485. doi: 10.1016/0010-4485(96)86819-9.

[18] R. Agromayor and N. Anand. Parablade documentation, 2019. Accessed: 2020-11-06.

[19] JA Samareh. A survey of shape parameterization techniques. *NASA Conference Publication*, 1999. ISSN 0001-1452.

[20] P. Dwight. *Robust mesh deformation using the linear elasticity equations.* 2006.

[21] Giancarlo Alfonsi. Reynolds-averaged navier-stokes equations for turbulence modeling. *Applied Mechanics Reviews - APPL MECH REV*, 62, 07 2009. doi: 10.1115/1.3124648.

[22] A. Rubino, M. Pini, P. Colonna, T. Albring, S. Nimmagadda, T. Economon, and J. Alonso. Adjoint-based fluid dynamic design optimization in quasi-periodic unsteady flow problems using a harmonic balance method. *Journal of Computational Physics*, 372:220–235, 2018. ISSN 10902716. doi: 10.1016/j.jcp.2018.06.023. URL https://doi.org/10.1016/j.jcp.2018.06.023.

[23] Frédéric Sicot, Guillaume Dufour, and Nicolas Gourdain. A time-domain harmonic balance method for rotor/stator interactions. *Journal of Turbomachinery*, 134(1), 2012. ISSN 0889504X. doi: 10.1115/1.4003210.

[24] Benoit Obert and Paola Cinnella. Comparison of steady and unsteady RANS CFD simulation of a supersonic ORC turbine. *Energy Procedia*, 129:1063–1070, 2017. ISSN 18766102. doi: 10.1016/j.egypro.2017.09.122. URL http://dx.doi.org/10.1016/j.egypro.2017.09.122.

[25] L. He. Three-dimensional unsteady Navier-Stokes analysis of stator-rotor interaction in axial-flow turbines. *Proceedings of the Institution of Mechanical Engineers, Part A: Journal of Power and Energy*, 2000. ISSN 09576509. doi: 10.1243/0957650001537813.

[26] Michael V. Casey. Accounting for losses and definitions of efficiency in turbomachinery stages. *Proceedings of the Institution of Mechanical Engineers, Part A: Journal of Power and Energy*, 221(6):735–743, 2007. ISSN 09576509. doi: 10.1243/09576509JPE459.

[27] D. Kraft. A Software Package for Sequential Quadratic Programming, 1988.

[28] Tecplot. Tecplot 360 Getting Started Manual. *Structure*, 2011. ISSN 17582229.

[29] B. Stephan, H. E. Gallus, and R. Niehuis. Experimental investigations of tip clearance flow and its influence on secondary flows in a 1-1/2 stage axial turbine. In *Proceedings of the ASME Turbo Expo*, 2000. ISBN 9780791878545. doi: 10.1115/2000-GT-0613.

[30] F. R. Menter. Two-equation eddy-viscosity turbulence models for engineering applications. *AIAA Journal*, 1994. ISSN 00011452. doi: 10.2514/3.12149.

[31] Linear solvers and preconditioners. URL https://su2code.github.io/docs_v7/Linear-Solvers-and-Preconditioners/.

[32] Antony Jameson. Origins and further development of the Jameson-Schmidt-Turkel scheme. *AIAA Journal*, 2017. ISSN 00011452. doi: 10.2514/1.J055493.

[33] Keiichi Morikuni, Lothar Reichel, and Ken Hayami. FGMRES for linear discrete ill-posed problems. *Applied Numerical Mathematics*, 2014. ISSN 01689274. doi: 10.1016/j.apnum.2013.08.004.

Appendix A

Baseline Grid Convergence Study

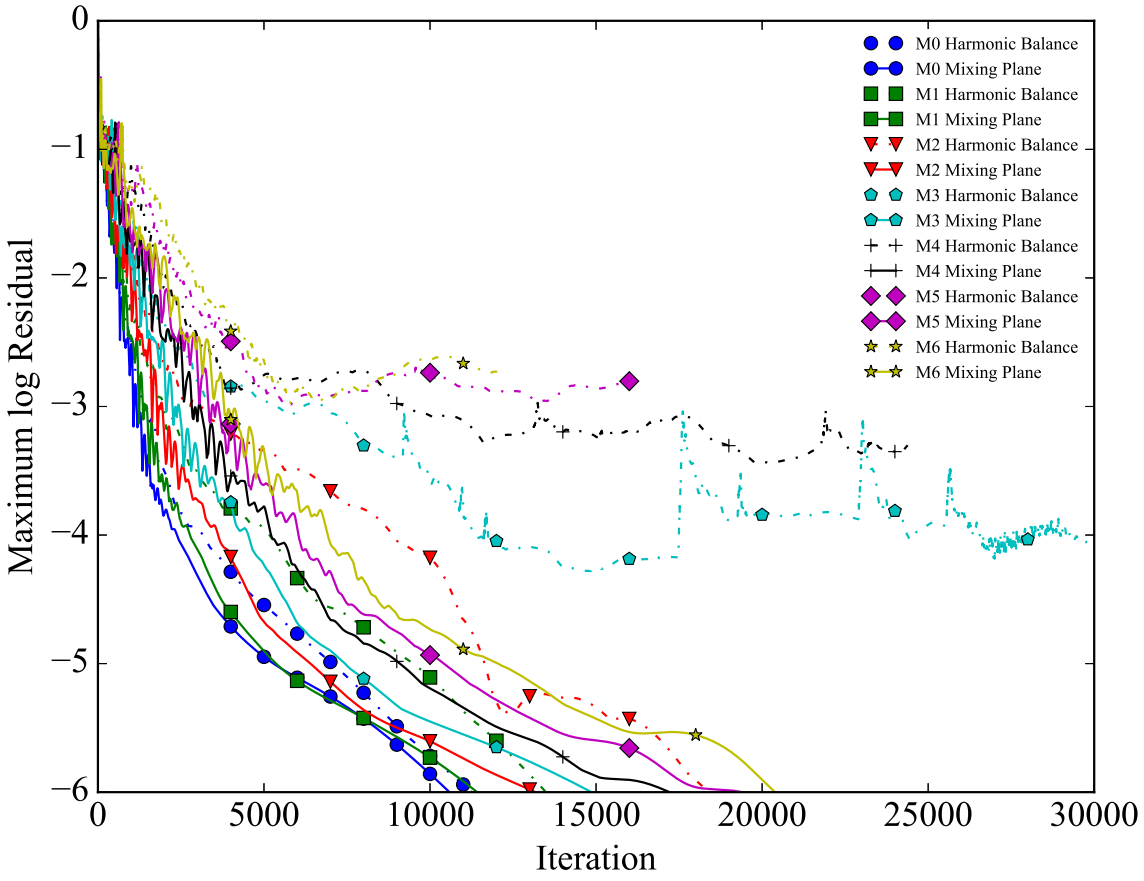

Fig. A.1: Grid Convergence Maximum Residual Value vs. Iteration count for increasing mesh element number.

Appendix B

Result Comparison to Grid Converged Meshes

	$s_{\text{gen}}[-]$		$\frac{\Delta s_{\text{gen}}}{s_{\text{gen,basline}}}[\%]$	
	Harmonic Balance	Mixing Plane	Harmonic Balance	Mixing Plane
Baseline M2	0.0352	0.0305	-	-
HB Optimized	0.0388	0.0329	+10.22	+7.86
MP Optimized	0.0431	0.0326	+22.44	+6.88
C1	0.0384	0.0321	+9.09	+5.24
C2	0.0378	0.0320	+7.39	+4.92

Table B.1: Overall Performance s_{gen} and percentage difference from baseline parameters for grid convereged mesh in both harmonic balance and mixing plane simulation type for Baseline, Harmonic Balance Optimized, Mixing Plane Optimized, C1, and C2 Designs.

B.0.1 Machine design region partitioning

To provide further understanding in to how the design is optimized the mass-flow averaged entropy ($\langle s_{gen} \rangle$) is extracted. The machine is partitioned into eight discrete zones, as can be seen in Figure B.1. The zone partition gives a breakdown and proportion of the loss factors.

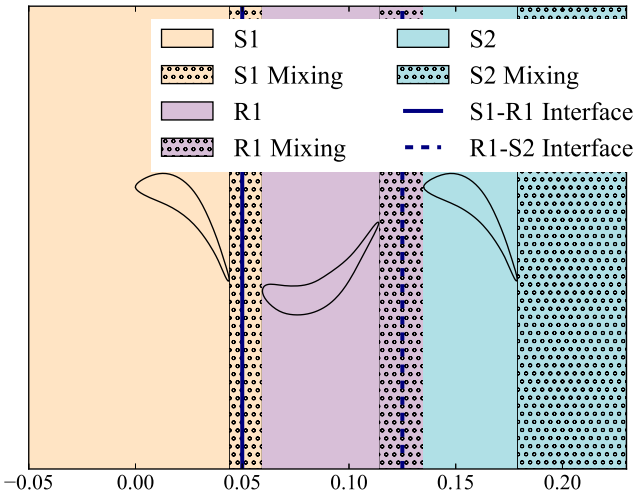

Fig. B.1: Multizone stage partition break down.

Stator 1 (S1) encompasses the entire area from the inlet to its trailing edge. (S1 Mixing) contains the zone where the Stator 1 wake is being mixed in the absence of any other physical object and extends from the Stator 1 trailing edge to the leading edge of Rotor 1. The first black line (S1-R1 Interface) encompasses any discontinuities due to either the interpolation interface for harmonic balance or the mass-flow averaging in the mixing plane method. While a discontinuity can be present in the flow quantities at an interface, the entropy generation rate is not affected too drastically as the value is only calculated on a zone by zone basis, i.e., $S1_{exit} - S1_{inlet}, R1_{exit} - R1_{inlet}, etc.$, and does not include differences at an interface.

Rotor 1 leading edge to Rotor 1 trailing edge is the (R1) zone with (R1 Mixing) extending from the trailing edge to the Stator 2 leading edge. A dashed line is present at the interface between Rotor 1 and Stator 2 and behaves similarly to the (S1-R1 Interface). The Stator 2 leading edge to the trailing edge is denoted by (S2), and (S2 Mixing) is from the Stator 2 trailing edge to the exit.

While there is mixing occurring at all times, further separation of losses was not done once the flow moves past a physical object. The Aachen test case does not have much flow in or above the trans-sonic region, M $\geq$ 0.7, and thus losses associated with shocks are negligible. Heat transfer as a source of entropy generation is also expected to be zero and not relevant to the current analysis. Other sources of loss are profile losses and the original mixing loss. The (S1 Mixing, R1 Mixing, and S2 Mixing) zones contain only losses associated with mixing. Simultaneously, the (S1, R1, and S2) zone are a combination of profile losses developing on the blade surface and mixing in the blade passage. Due to the interface in both harmonic balance and mixing plane distorting the wake contours, individual blades' wakes could not be isolated past the blade domain in which it was created.

B.1 HB-based Optimization Results

The effects of the mesh on entropy through the machine can be seen in Figure B.2 with a comparison between the grid-dependent (M0), and grid converged (GC) mesh.

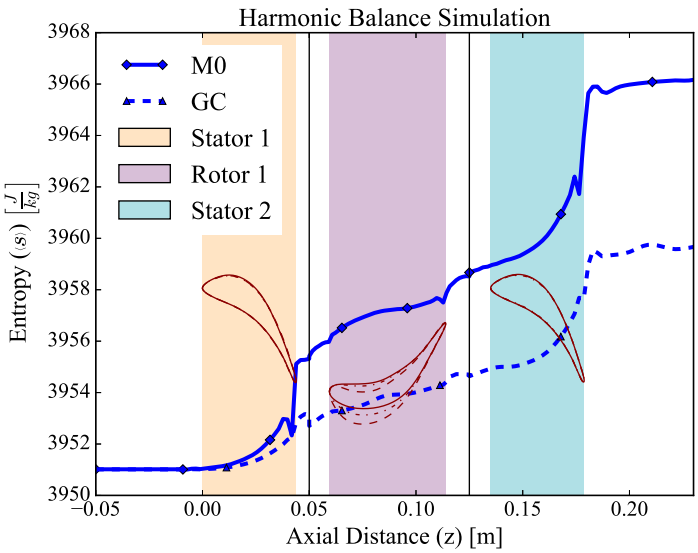

Fig. B.2: M0 mesh to Grid Converged Mesh Harmonic Balance Simulation mass-flow averaged entropy trend.

As can be seen in Figure B.2, the entropy result of the M0 mesh is consistently higher by a large margin. The entropy increase could be due to $SU2$ not implementing wall-functions and requiring a low y^+ value along the blade boundary.

Even though the total entropy generated is quite different, proportionality in specific zones was considered. In Figure B.3 a breakdown is shown as a comparison of the change in entropy in a specific zone for the baseline blades harmonic balance simulation in (**a**)and the harmonic balance optimized blades in (**b**). For both (**a**) and (**b**), the ratio for entropy creation in specific zones changes between the M0 and grid converged meshes. Surprisingly the baseline proportion in (**a**) for the S2 is nearly identical for the M0 and grid converged mesh.

Nevertheless, the optimized blades of (**b**) show a sizable difference in the total loss of the Stator 2 zone. The M0 mesh underestimates the influence of mixing after the Stator 2 blade.

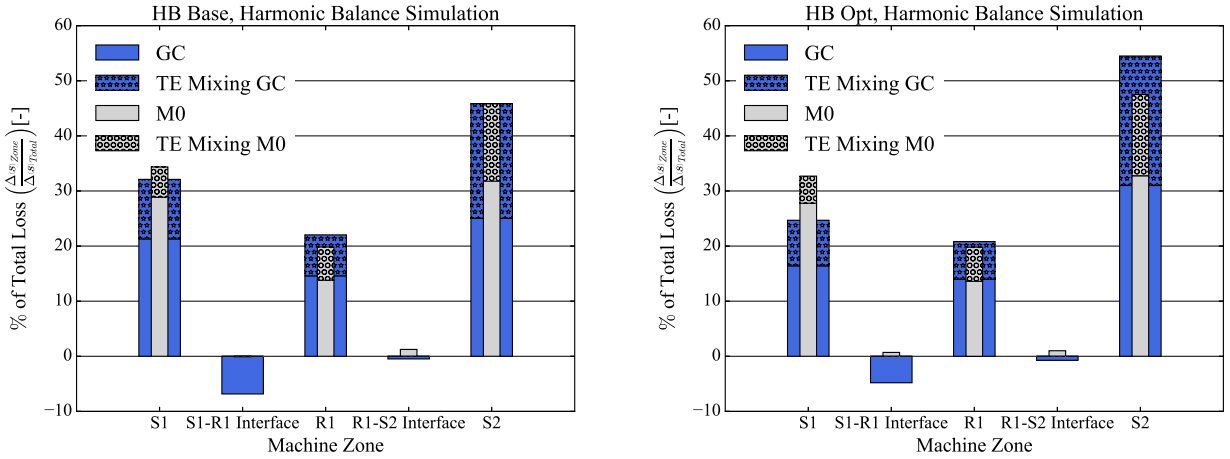

(**a**) Loss break down by zone for baseline blades in M0 and M2 (GC) meshes.

(**b**) Loss break down by zone for harmonic balance optimized blades in M0 and M2 (GC) meshes.

Fig. B.3: Baseline and harmonic balance optimized design loss break down by zone for (**a**) baseline M0 and M2 meshes and (**b**) harmonic balance optimized M0 and Grid converged meshes using a harmonic balance simulation.

For a more accurate comparison, the grid converged mesh for the harmonic balance optimized design was compared to the baseline using grid converged meshes. In Figure B.4 the entropy through the machine is again shown for the grid converged case in (**a**) with the difference shown in (**b**). It is interesting to see that a similar improvement trend is seen in the grid converged case as the M0 mesh for Stator 1 and Rotor 1. The M0 optimization is successful until the flow reaches Stator 2, where all previous improvement is negated, and the machine as a whole performs worse than the baseline.

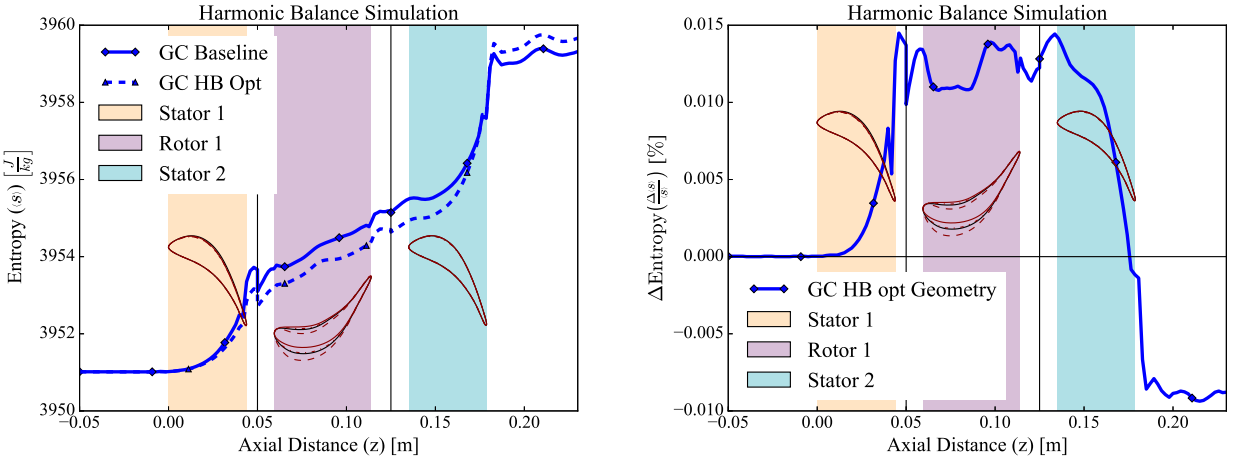

(a) Baseline M2 and harmonic balance optimized grid converged meshes mass-flow entropy trends.

(a) Baseline M2 and harmonic balance optimized grid converged meshes mass-flow entropy difference.

Fig. B.4: Baseline and harmonic balance optimized design grid converged (**a**) mass-flow averaged entropy and (**b**) mass-flow averaged entropy difference using a harmonic balance simulation.

From Figure 5.31 and Figure B.4 the harmonic balance optimization can be considered a success for both Stator 1 and Rotor 1 performance. Stator 2 shows divergent behavior for the two grids and serves as an example that grid-independent meshes are not a necessary pre-condition for optimization. While this may not be a general trend for other machines, this is a worthwhile trait for further investigation.

B.2 MP-based Optimization Results

The effects of the mesh on entropy through the machine can be seen in Figure B.5 for the mixing plane optimized design with a comparison between the M0 and grid converged (GC) mesh shown. As can be seen in Figure B.5, the entropy result of the M0 mesh is consistently higher by a large margin. The entropy increase could be due to $SU2$ not implementing wall-functions and requiring a low y^+ value along the blade boundary.

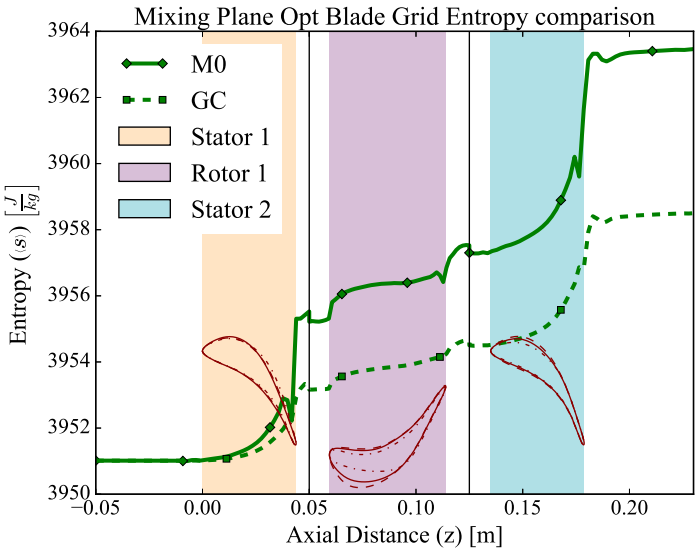

Fig. B.5: Mixing plane optimized design entropy in M0 and Grid converged meshes using a mixing plane simulation.

Even though the total entropy generated was quite different, proportionality in specific zones was considered. In Figure B.6 a breakdown is shown to compare the change in entropy in a specific zone for the baseline blades mixing plane simulation in (**a**) and for the mixing plane optimized blades in (**b**). The Stator 1 and 2 loss proportions switch from either over or under-estimating loss compared to their respective grid converged meshes when comparing the baseline to mixing plane optimized design. The loss proportion associated with discontinuities at the interface remains relatively stable between baseline and optimized geometries and mesh size.

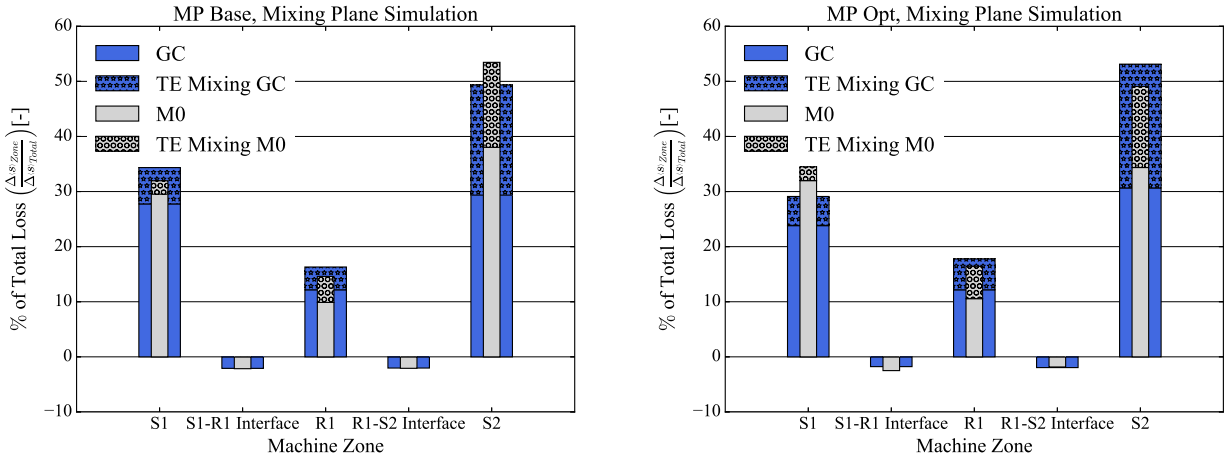

(a) Baseline blades

(**b**) Mixing plane optimized blades

Fig. B.6: Loss breakdown by zone for mixing plane baseline and mixing plane optimized blades using a mixing plane simulation.

In Figure B.7 the mixing plane optimized design is simulated with a grid converged mesh and entropy compared

to the baseline grid converged mesh in (**a**) with the difference shown in (**b**). Similar to the harmonic balance optimization grid converged results, both Stator 1 and Stator 2 show better performance than the baseline grid converged mesh. A majority of the losses occur in the Stator 2 blade, where the grid-dependent mesh makes all of its improvement. Part of the answer to this discrepancy lies in the results that the mixing plane grid-dependent optimized blade underestimates the Stator 2 region losses seen in Figure B.6 (**b**) and even further underestimates losses associated with Stator 2 trailing edge mixing. Trailing edge mixing accounts for nearly two-thirds of the entropy difference change in Figure B.6 (**b**) and is a majority of the reason why mixing plane suffers from such a severe decrease in performance when moving from the grid-dependent (M0) to grid converged mesh.

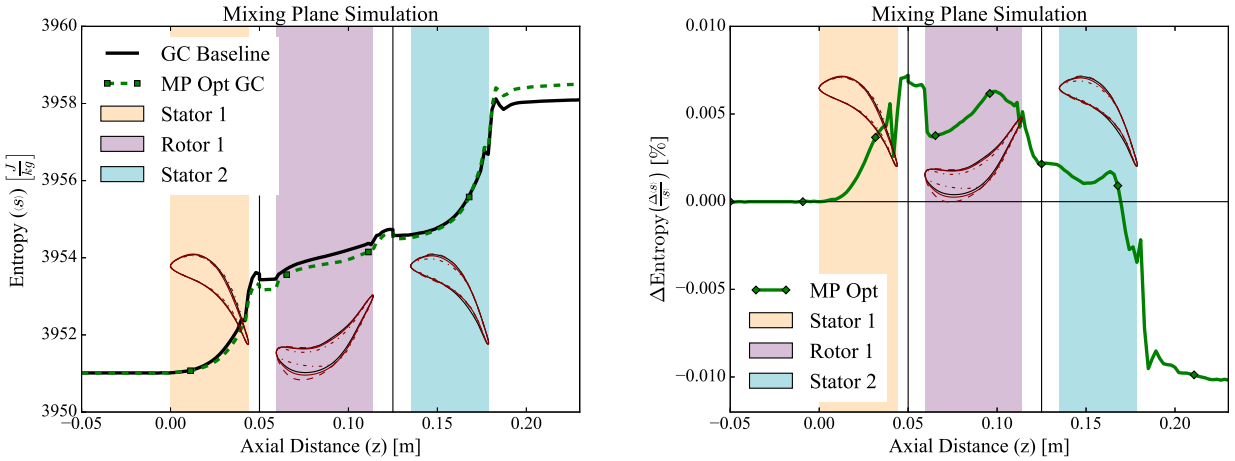

(**a**) Baseline M2 and mixing plane optimized design grid converged mass-flow averaged entropy.

(**b**) Baseline M2 and mixing plane optimized design grid converged mass-flow averaged entropy difference.

Fig. B.7: Baseline and mixing plane optimized design grid converged (**a**) mass-flow averaged entropy and (**b**) mass-flow averaged entropy difference using a mixing plane simulation.

B.3 C1

Figure B.8 shows the grid converged entropy trends through the machine in both harmonic balance and mixing plane simulations with both the harmonic balance and mixing plane optimized geometries. In (**a**), the C1 and harmonic balance optimized design entropy trend is nearly identical to the Stator 2 blade's geometric throat. By the outlet, the harmonic balance entropy is above the baseline shape as demonstrated earlier, but the C1 geometry outlet entropy is much closer to the baseline entropy at the outlet. A similar trend can be seen in (**b**) in the mixing plane simulation. The C1 geometry has a lower entropy value than the mixing plane optimized blades from the inlet to around the Stator 2 blade's geometric throat. At this point, both C1 and the mixing plane optimized design show an increase in entropy creation and end up producing more entropy than the baseline design.

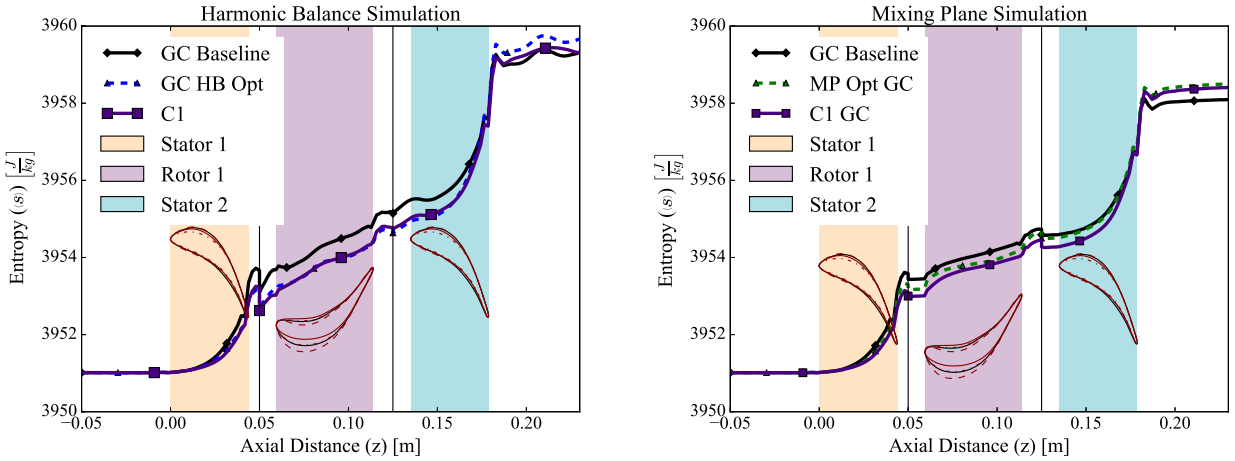

(**a**) baseline to optimized mass-flow averaged entropy using a harmonic balance simulation.

(**b**) baseline to optimized mass-flow averaged entropy difference using a mixing plane simulation.

Fig. B.8: Hybrid configuration C1 mass-flow averaged entropy using (**a**) harmonic balance simulation and (**b**) mixing plane simulation.

In Figure B.9 the C1 geometry entropy change in each zone is compared for the M0 and grid converged meshes in the harmonic balance and mixing plane simulation methods.

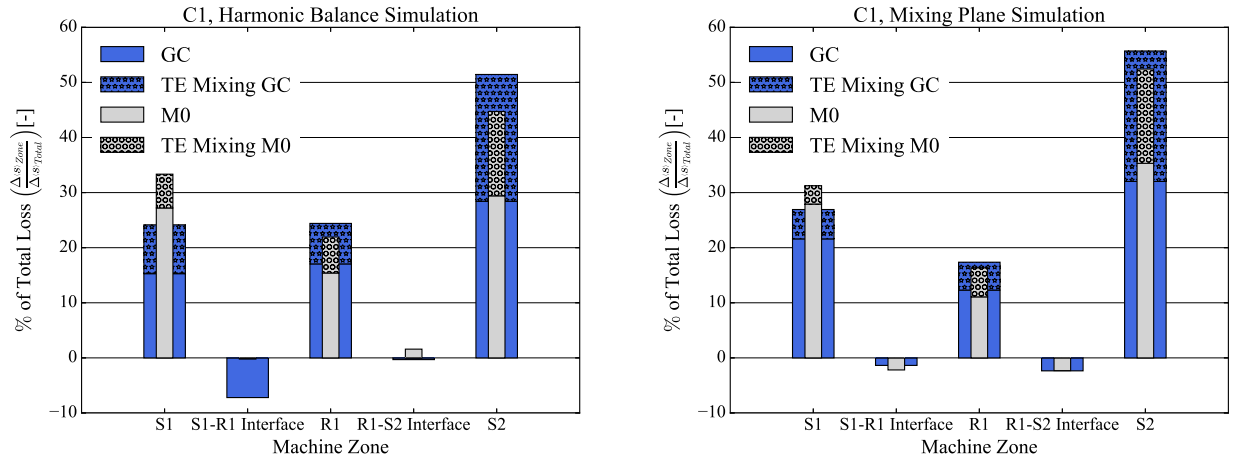

(**a**) Harmonic balance

(**b**) Mixing plane

Fig. B.9: Hybrid configuration C1 mass-flow averaged entropy zone partition breakdown for M0 and Grid converged meshes in (**a**) Harmonic Balance and (**b**) Mixing Plane

A trend stands out for why the C1 geometry seems to show such promise in the M0 grid and not for the grid converged mesh. The main point of improvement for the C1 configuration occurs as a result of the Stator 1 zone. The improvement is overestimated, while the Stator 2 zone is underestimated in the M0 mesh compared to the grid converged mesh. The harmonic balance results also show a larger difference between the over or under-estimation amounts than the mixing plane results.

When comparing the grid converged results to the grid converged mesh in Figure B.10, a similar situation of previous performance gains being negated in the geometric throat of the Stator 2 blade is shown. The theory that hybrid blades can perform better shows promise that even though the C1 configuration performs worse than the baseline, the difference is the lowest among either the mixing plane optimized or harmonic balance optimized designs.

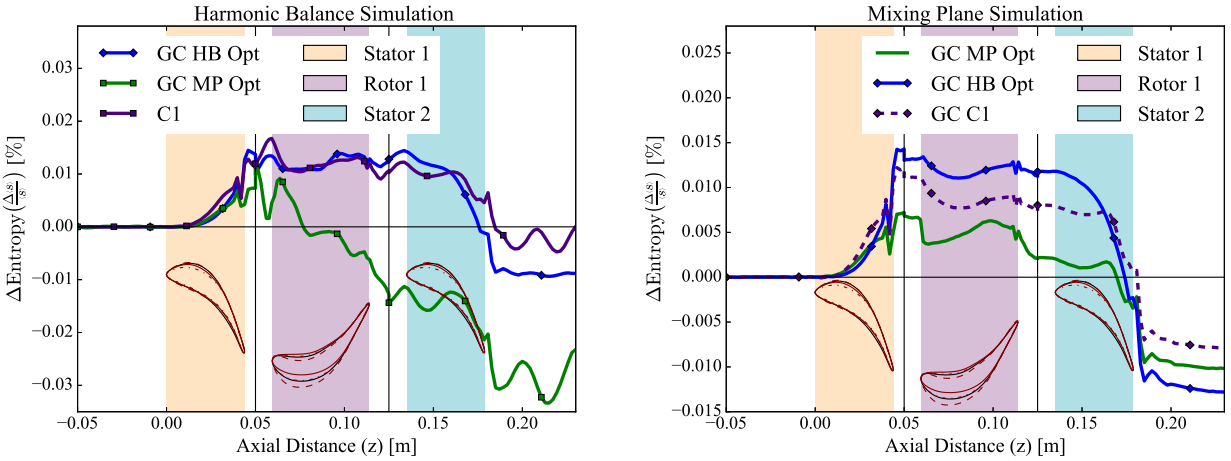

(**a**)Harmonic balance, Mixing plane, and configuration C1 grid converged mass-flow entropy difference in harmonic balance.

(**b**) Harmonic balance, Mixing plane, and configuration C1 grid converged mass-flow entropy difference in mixing plane.

Fig. B.10: Hybrid configuration C1 grid converged mass-flow averaged entropy difference using an (**a**) harmonic balance and (**b**) mixing plane simulation.

B.4 C2

Figure B.11 shows the machine's entropy trends in both harmonic balance and mixing plane simulations. In (**a**), the entropy trends for the harmonic balance optimized blades and C2 configuration are nearly identical from the machine inlet to the Stator 2 blade's geometric throat. The increase in entropy, which occurs in the final half of the Stator 2 blade, produces the same final entropy value at the outlet as the baseline design. The C2 configuration outperforms the mixing plane optimized blades for the machine's entirety in the mixing plane simulation.

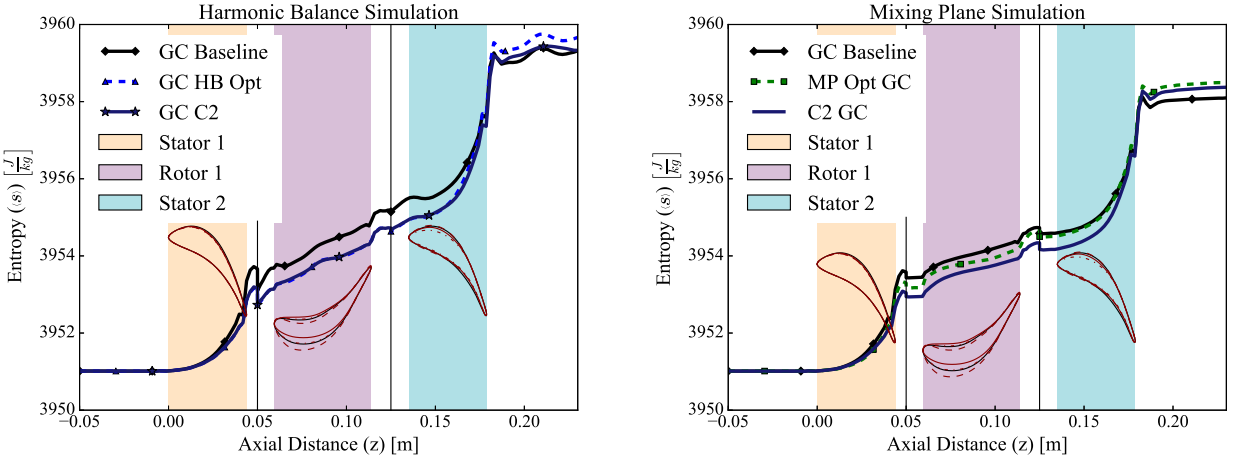

(**a**) Mass-flow averaged entropy in a harmonic balance simulation.

(**b**) Mass-flow averaged entropy difference in a mixing plane simulation.

Fig. B.11: Hybrid optimized C2 mass-flow averaged entropy using an (**a**) harmonic balance and (**b**) mixing plane simulaton.

In Figure B.12, each zone's entropy difference is compared for the M0 and grid converged meshes of the C2 configuration. The harmonic balance simulation shows a larger difference in entropy distribution between M0 and grid converged meshes. The Stator 1 zone's performance benefit in the C2 configuration is similarly overestimated, with the Stator 2 zone being underestimated as seen in the previous geometries.

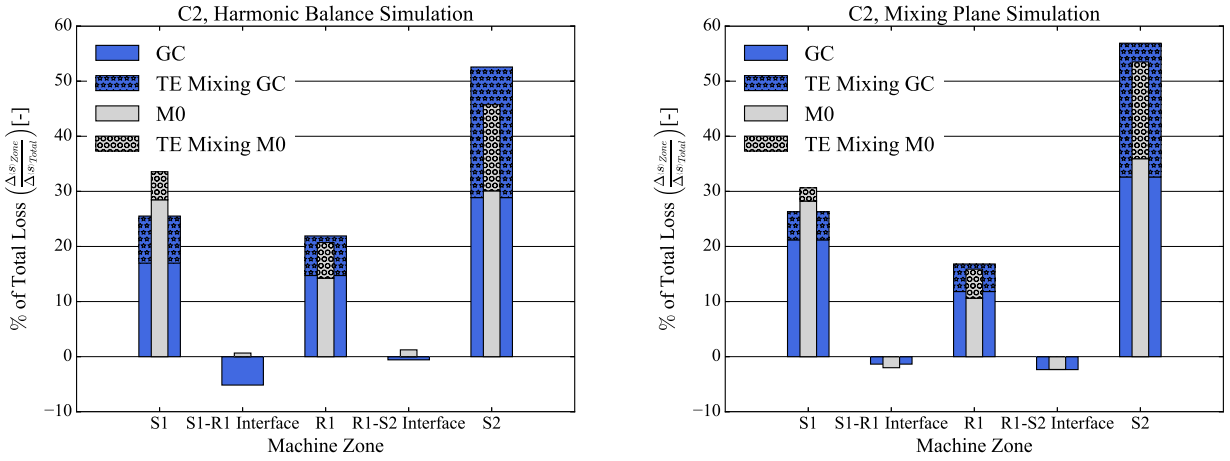

(**a**) Loss breakdown of M0 and grid converged mesh of configuration C2 using the harmonic balance method.

(**b**) Loss breakdown of M0 and grid converged mesh of configuration C2 in mixing plane

Fig. B.12: Hybrid configuration C2 mass-flow averaged entropy zone partition breakdown for M0 and Grid converged meshes using the (**a**) harmonic balance and (**b**) mixing plane methods.

The entropy differences for the grid converged C2 configuration are compared to the baseline M2 mesh for harmonic balance, and mixing plane simulations are shown in Figure B.13. As seen in every previous geometry, the new configuration performs well until the second half of the Stator 2 blade, where all previous performance benefits are negated. In the mixing plane simulation shown in Figure B.13 (**b**), the Stator 2 blade of configuration C2 shows a greater resilience to the worsening performance of the last half of the Stator 2 blade. While the mixing plane optimized Stator 2 blade causes an upstream influence and subsequent performance reduction compared to the harmonic balance optimized, the drop in performance is not as severe as the harmonic balance optimized Stator 2 blade shape. However, it is worse than the solely mixing plane optimized blade. This trend shows that blade shapes can be traded between optimizations and that the entropy behavior defect upstream is not one-to-one proportional to the downstream entropy defect.

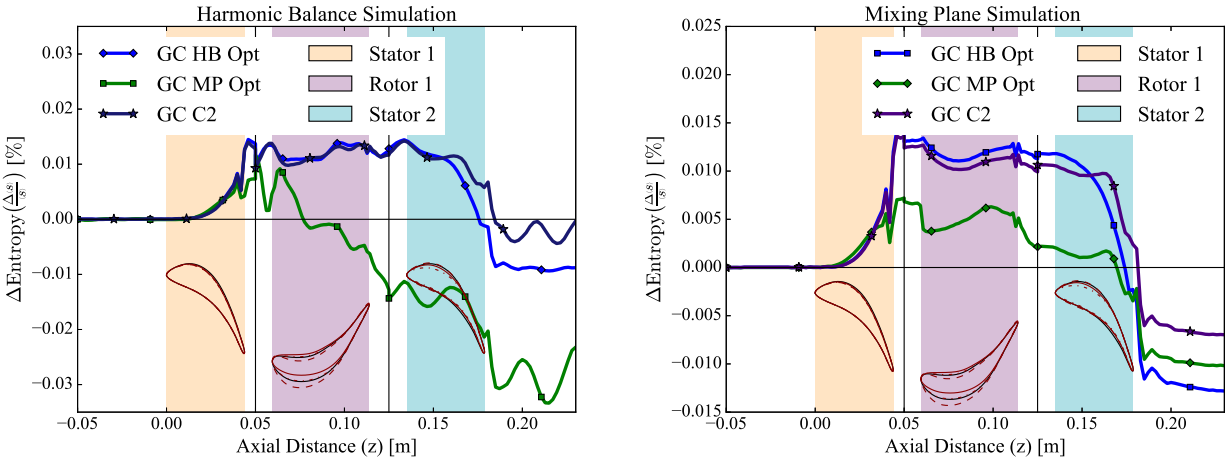

(**a**)Harmonic balance, Mixing plane, and configuration C2 grid converged mass-flow entropy difference in a harmonic balance simulation.

(**b**) Harmonic balance, Mixing plane, and configuration C2 grid converged mass-flow entropy difference in a mixing plane simulation.

Fig. B.13: Hybrid configuration C2 grid converged mass-flow averaged entropy difference using an (**a**) harmonic balance and (**b**) mixing plane simulation.